Dynamics of Dust and Planets in turbulent Accretion Disks

Dissertation

der Mathematisch-Naturwissenschaftlichen Fakultät
der Eberhard Karls Universität Tübingen
zur Erlangung des Grades eines
Doktors der Naturwissenschaften
(Dr. rer. nat.)

vorgelegt von
Moritz Stoll
aus Tübingen

Tübingen
2017

Tag der mündlichen Qualifikation: 16.05.2017

Dekan:	Prof. Dr. Wolfgang Rosenstiel
1. Berichterstatter:	Prof. Dr. Wilhelm Kley
2. Berichterstatter:	Prof. Dr. Klaus Werner

Abstract

This thesis studies the dynamics of dust and planets in turbulent accretion disks. As source for the turbulence in the disk the vertical shear instability (VSI) was investigated, a hydrodynamic instability with a unique flow pattern, that can generate weak turbulence. We first performed numerical simulations to validate the applicability of the VSI in the context of protoplanetary disks. The results of the simulations including radiation transport indicate that indeed parts of the so-called dead zone are unstable to the VSI and produce weak angular momentum transport.

Encouraged by this result we studied the impact of the VSI on the dust in the disk. We added dust particles into the disk and analyzed their evolution. We found that the VSI has a strong bunching effect on the dust particles, leading to ringlike structures with enhanced dust density. These clusters are regions with faster dust growth and possibly supply the necessary conditions for the streaming instability.

Furthermore we explore the interaction between the VSI and embedded planets. Here it becomes important that the turbulent viscosity of the VSI does not act the same way as the kinematic viscosity employed by the traditional α-model. While the gap depth and width created by the presence of massive planets is similar in models with a kinematic viscosity, the lifetime of vortices formed by the Rossby wave instability at the gap edge is not. The outer vortex is stable and the inner vortex can even migrate inwards without signs of decay. In the simulations with a smaller planet we observed up to five time faster migration rates. This is caused by a small vortex behind the planet, which is not dispersed by the turbulence, in contrast to viscous α-models, where they can not even be generated.

Zusammenfassung

Diese Dissertation untersucht die Dynamik von Staub und Planeten in turbulenten Akkretionsscheiben. Als Quelle für die Turbulenz in der Scheibe wurde die vertikale Scherinstabilität (VSI) untersucht, eine hydrodynamische Instabilität mit einem ungewöhnlichem Strömungsbild, welches schwache Turbulenz generiert. Zuerst überprüften wir mit Hilfe numerische Simulation ob diese Instabilität auf protoplanetaren Scheiben anwendbar ist. Diese Simulation ergaben, dass selbst unter Einbeziehung von Strahlungstransport die sogenannte tote Zone anfällig für die VSI ist und einen schwachen Transport von Drehimpuls erzeugt.

Ermutigt von diesen Ergebnissen haben wir den Einfluss der VSI auf den Staub in der Akkretionsscheibe untersucht. Dazu fügten wir Staubteilchen in die Akkretionsscheibe ein und untersuchten deren Entwicklung. Dadurch entdeckten wir, dass die VSI einen starke Klumpung von Staubteilchen hervorruft, was zu ringförmigen Strukturen mit erhöhter Staubdichte führt. In diesen Staubansammlungen kann der Staub schneller anwachsen und außerdem ist dieser Bereich möglicherweise anfällig für die Strömungsinstabilität.

Außerdem untersuchten wir die Wechselwirkung zwischen der VSI und eingebetteten Planeten. Hier ist es nun wichtig, dass die turbulente Viskosität der VSI nicht wie eine kinematische Viskosität wirkt, die üblicherweise in α-Modellen verwendet wird. Zwar ist die Tiefe und Breite der Lücke, die durch massive Planeten erzeugt wird, sehr ähnlich in Modellen mit kinematischer Viskosität, allerdings sind die Vortizes die von der Rossby Welleninstabilität am Rand der Lücken erzeugt werden deutlich stabiler. Der Vortex am inneren Rand kann sogar einwärts migrieren, ohne Anzeichen eines Zerfalls zu zeigen. In den Simulationen mit kleineren Planeten beobachteten wir bis zu fünf mal höhere Migrationsraten. Dies wird durch einen kleinen Vortex hinter dem Planeten verursacht, der nicht durch die Turbulenz aufgelöst wird. Im Gegensatz dazu können diese Vortizes in viskosen α-Modellen nicht einmal erzeugt werden.

Contents

1 Introduction

Recently, it was discovered that even the closest star to our Sun, Proxima Centauri, is a host for a rocky planet, close in mass to the Earth. But while observations can inform us about orbital parameters, for example we know that the planet orbits Proxima Centauri in a distance of 0.05 au with a period of 11.2 days, not much is known about its formation. Nowadays more and more Earth-like planets are found but it is still impossible to observe the formation of planets directly. This leaves only theoretical consideration and simulations to study planet formation.

With simulations it is possible to explore the earlier phases of planet formation, when the disk was still accreting onto the star and interacted with the planet. We can study how the planet migrated through this disk due to gravitational interaction with the disk, until we reach the birthplace of the planet. We can analyze how the dust interacted with the gas of the disk, how it was pushed around by the turbulent motion of the gas and in turn shaped the gas. We can go back even further and research how the turbulence shaped the disk.

To provide context for the publications the next sections will give an overview of planet formation. I will first give an introduction on the accretion disks and the turbulence within. Then I will review the dust evolution and finally I will discuss the planets and their migration. I will present the aim of this thesis in Chapter 2. Chapter 3 will provide the publications and finally I will discuss the results and give an outlook to future research on this field in Chapter 4.

1.1 Accretion disk dynamics

Historically, not much was known about accretion disks from observations. Instead one had to reason about the internal dynamics of accretion disks, beginning with its

creation. A star forms from an extended molecular cloud which collapses under its own gravity. Due to the small initial rotation in the molecular cloud not all of the initial gas of the cloud will collapse onto the star. Instead angular momentum conservation will prevent the inflow of the gas and lead to an almost stable configuration of gas orbiting the star on circular orbits with Keplerian velocity. These flat disks usually extend up to several hundred au. As the name accretion disk already implies, those disks will slowly accrete their matter onto the star. The lifetime of these accretion disks depends on the timescale on which the angular momentum of the gas can be transported outwards, as this allows the gas to accrete inwards.

Alpha disk model

A simple first guess for the source of angular momentum transport would be the kinematic viscosity. The exchange of angular momentum would be directly due to collision between particles with slightly different velocities. This does lead to inflow of matter, but it can be calculated that this process would lead to timescales several orders of magnitude larger than the lifetime of the universe. Even without further observational evidence it is clear that this is far too slow. Fortunately this model can be salvaged if the kinetic viscosity is substituted with a turbulent viscosity.

Indeed one of the first models of accretion disks, which is still used today, is the model of Shakura and Sunyaev (1973). They reasoned that the largest turbulent eddy can be of the size of vertical height of the disk H. Additionally, a typical velocity in a disk is the isothermal sound speed c_s. Together this leads to a simple model for the turbulent viscosity:

$$\nu = \alpha c_s H \,, \tag{1.1}$$

where α is a dimensionless constant, that quantifies the strength of the turbulence. We can then estimate an α from observations of the lifetime of protoplanetary disks.

Lifetime of disks

The lifetime of accretion disks can be estimated from the observation of star clusters (Williams and Cieza, 2011). For each cluster one estimates the age of the cluster and the fraction of stars in the cluster with accretion disks. In very young cluster with an age of less than one million years nearly every star will have a disk. This fraction then

drops of to half of the stars at around 2.5 million years and finally after 10 million years almost none of the stars will have retained their disk. Hence, a typical disk lifetime is around 2.5 million years, with a large error in the order of one million years due to the difficulty in accurately estimating the age of very young stars. The lifetime of a specific disk will also depend on a few parameters, for example the mass of the star and metallicity of the disk. From this lifetime we can now estimate the α-parameter to lie between 10^{-3} and 10^{-2} for protoplanetary disks.

Magneto rotational instability

An instability that can reach this level of turbulence is the magneto rotational instability (MRI) first studied by Balbus and Hawley (1991). The MRI generates magnetic fields which can transport angular momentum outwards, provided there is a small initial magnetic field. Another condition for the disk to be unstable to the instability is an outwardly decreasing angular orbital frequency profile, which is easily satisfied in Keplerian disks. The biggest obstacle for the MRI is the low ionization fraction in protoplanetary disks. The magnetic field can only properly connect to the gas if there are enough free electrons and ions to couple the magnetic forces with the gas. But the ionization fraction in protoplanetary disks is usually too low for the ideal MHD equations to be applicable, instead the diffusive MHD equations need to be considered in major parts of the disk. Nevertheless at the inner region of the disk ($r < 0.5\,\mathrm{au}$) the temperatures are typically hot enough for sufficient ionization of the gas. At this temperature the collisions between the hydrogen atoms themselves are already ionizing. The force of the magnetic field threading the disk will then act on the gas parcels on different orbits similar to a spring between them and the magnetic field thus acts against the gas being sheared apart due to the differential rotation. Since the inner gas parcel has the higher angular momentum in a protoplanetary disk, this exchange of angular momentum leads to the outward transport.

Farther out in the disk the ionization will be too small and the resistivity of the gas will suppress the MRI. This region with suppressed MRI is often called “dead zone”, because it was thought that this region is not turbulent, but this needs not to be true as other instabilities may be active. It was also predicted by Gammie (1996) that the surface layers of this region may still be active and excite the dead zone. Also new

simulations including the Hall effect and ambipolar diffusion show a small activity in this region.

In the outer regions the disk is thin enough that the ionizing x-rays from the star can reach the midplane of the disk and provide a sufficient ionization. Nevertheless, the different diffusive terms may dominate in this region, preventing turbulence.

Fortunately, magnetic fields are not the only way to generate turbulence in accretion disks. While it was initially thought that purely hydrodynamic instabilities can not play a significant role because the level of turbulence they generate is relatively small and not sufficient to explain the expected lifetime of disks, the dead zone and layered accretion provide the possibility that they are nevertheless important for the disk dynamics outside of being the main source of angular momentum transport. For example even a low level of turbulence is extremely important for the dust settling and transport and thus also plays a major role in planet formation.

Gravitational instability

A well studied purely hydrodynamic instability is the gravitational instability. In a massive disk the self-gravity of an over-dense perturbation in the disk can act against the stabilizing shear and pressure and lead to a collapse of this region. The criterion for stability was found by Toomre (1964) to be:

$$Q = \frac{c_s \kappa}{\pi G \Sigma} \lesssim 1 \tag{1.2}$$

where κ is the epicyclic frequency, quantifying the shear and Σ is the surface density of the disk. The disk is unstable if $Q \lesssim 1$ is satisfied. This condition is usually only fulfilled in the outer region of massive protoplanetary disks. Another important factor for the level of activity is the radiative cooling (Gammie, 2001). Depending on the local physics this leads to sustained turbulence or even fragmentation of the disk. The fragmentation of the disk due to the gravitational instability is one possible explanation for the formation of gas giant planets.

Convective overstability and subcritical baroclinic instability

Another source for hydrodynamic activity is convection. The convective overstability (Lyra, 2014) makes use of the epicyclic oscillations naturally occurring in an accretion

disk. If the cooling times are in the order of the dynamical times, the oscillating gas parcel will not be in thermal equilibrium with the surrounding gas, leading to a radial buoyant force that slowly increases the amplitude of the oscillation. While it is unclear if the very specific conditions needed, for example on the radial entropy gradient, are met in a protoplanetary disk, it would be a convenient way to trigger the subcritical baroclinic instability (SBI).

The SBI can create long lived vortices with a weak angular momentum transport ($\alpha \sim 10^{-3}$) out of small initial perturbations (Lesur and Papaloizou, 2010). Vortices play a major role in planet formation, since dust can be collected inside, leading to enhanced growth of dust particles.

Rossby wave instability

The Rossby wave instability (RWI, Lovelace et al., 1999, Li et al., 2000, 2001) is another instability which is important in the context of planet formation due to the generation of vortices. The region is unstable if there is a maximum in the inverse potential vorticity:

$$\frac{\Sigma S^{2/\gamma}}{2(\nabla \times u)_z}, \tag{1.3}$$

where Σ is the surface density, S is the specific entropy, γ is the specific heat ratio, and u is the gas velocity.

While the condition for the RWI can not be reached in an undisturbed disk, they are readily met at the edge of gaps created by massive planets (de Val-Borro et al., 2007). There the bump in the radial pressure profile leads to a local extremum in the rotation speed. This axisymmetric peak in the vorticity is then unstable to the RWI and decays to multiple small vortices. These can then merge to a single large vortex. Another region where they are expected to form is the inner edge of the dead zone, there a pressure bump is expected due to the sudden increase in turbulent viscosity (Lyra and Mac Low, 2012).

Vertical shear instability

The vertical shear instability (VSI) was first discovered by Goldreich and Schubert (1967), Fricke (1968), in the context of differentially rotating stars. As the name im-

plies, the instability feeds on the vertical shear in the angular momentum profile of the disk, which is generated by a radial gradient in temperature. The condition for instability can be shown by extending the Rayleigh criterion $\frac{dj^2}{dR} < 0$ for inviscid disks without vertical shear to disks with vertical shear. If the cooling is fast enough to overcome the stabilizing buoyancy the stability criterion is then extended to (Urpin, 2003, Arlt and Urpin, 2004):

$$\frac{\partial j^2}{\partial R} - \frac{k_R}{k_Z}\frac{\partial j^2}{\partial Z} < 0\,. \tag{1.4}$$

Here $j = R^2\Omega$ is the angular momentum and k_R, k_Z are the wavenumbers of the perturbation in radial and vertical direction. From this criterion we can see that any disk with vertical shear is unstable, if the wavevector is sufficiently elongated in the vertical direction. For numerical simulations this makes high radial resolution necessary.

The growth rate of the instability is (Nelson et al., 2013):

$$\sigma \sim q\frac{H}{R}\Omega\,, \tag{1.5}$$

where H is the scale height of the disk, which depends on the temperature, R is the distance to the star and q is the exponent for the power law of temperature $T \sim R^q$. Thus the VSI can quickly grow on the timescale of the inverse angular frequency, but strongly depends on the details of the temperature profile. For protoplanetary disks one expects q to be between -0.5 and -1 and H/R is usually assumed to be close to 0.05 (Armitage, 2011).

More interesting than the linear growth is the level of turbulence for the saturated state. There the wavelength is limited due to the viscous and radiative diffusion lengths (Barker and Latter, 2015). The viscous diffusion length sets a lower limit on the lengthscale of the VSI, as the fluid element needs to retain its angular momentum during the exchange. As the disk becomes more turbulent due to the VSI the viscous diffusion length also increases and together with the scale height of the disk, this sets a natural limit to the VSI activity.

The thermal diffusion length can also be an upper limit to the lengthscale of the VSI, since the VSI has to overcome the vertical buoyancy. This dictates an upper limit on the cooling time, which can be a limiting factor in outer parts of the disk (Lin and Youdin, 2015).

1.2 Dust evolution

The growth of planetesimals from microscopic dust particles is the first step for planet formation. Initially around 1% of the disk mass is in dust particles. They are initially well mixed with the gas and consist mainly of silicates with a size in the micrometer range. Due to Brownian motion they will move around in the gas and collide with other dust particles. If the relative velocities are small enough they will stick together and begin to form larger dust conglomerates. Experiments have shown that they are typically fragile and can easily fragment if they collide with other dust conglomerates that are faster than 1 m/s (Blum, 2010). The fragmentation does not only inhibit dust growth but is an important process as it prevents the depletion of small dust grains in the disk for the later stages of the accretion disk. Small grains are important for the opacity of the disk and have been confirmed by observations to still be present in the disk even in the late phases of planet formation.

Another possible outcome of the collision between two dust particles is a collision where they bounce off each other. It has been shown in experiments that this result is most likely for particles in the mm-range. This is the first barrier to further growth of the dust grains (Windmark et al., 2012). This barrier may be overcome by a few lucky particles, for which the collision velocity was unlikely slow for a few consecutive collisions. If these particles become large enough, they can sweep up the smaller particles and grow further. Fragmentation of these seed particles may then increase the number of particles that can overcome the barrier.

With the increasing size of the dust aggregates they are no longer strongly coupled to the gas. In this regime the particles are still smaller than the mean free path of the gas molecules. The drag force is then in the Epstein regime, where the coupling is directly due to the collision between gas and dust particles. An often used parameter to characterize the strength of the drag force is the stopping time, which is defined as the time scale on which the dust particle is accelerated to a velocity close to the surrounding gas. This is also the timescale on which the dust settles to the midplane due to the vertical gravity in the disk. The settling is counteracted by turbulence. Another effect of the decoupling is that the collision speed between dust particles is then set by the turbulent gas motion, which is another reason why the strength of the turbulence is important for the dust evolution.

The drag force causes the next barrier on the way to planet formation. Dust moves with Keplerian velocity, which is the velocity where gravity and the centrifugal force balance each other. But gas feels also the pressure gradient, leading to slightly sub-Keplerian velocities for the gas. Hence the azimuthal velocities between dust and gas differ. This leads to a constant drag force between the dust and gas. Because the gas dominates the mass of the disk and rotates slower due to the pressure support, the gas slows down the particles, leading to an inward drift of the particles. The speed of the inward drift depends on the stopping time and is strongest for particles with a stopping time close to the time for one orbit. For smaller stopping times the particles are closely coupled to the gas and leading to a smaller difference in the azimuthal velocities, reducing the inward drift speed. Larger stopping times on the other hand lead directly to a longer time scale for the deceleration, resulting in a slower inward drift speed.

The fastest drifting bodies have a typical size in the order of meters and reach the star in a few thousand years. This is the "drift problem" in planet formation. Thus we expect a mechanism to exist that stops or slows down the meter sized dust particles.

One possible way to stop the inward drift is a pressure maximum in the gas. In a pressure maximum the gradient in pressure is zero, removing the pressure support from the gas. Hence the gas and the dust move with the same velocity on stable orbits. Even more important, on the side to star of the pressure maximum the pressure gradient is positive, leading to gas which is faster than the dust. Thus the dust in this region will drift outwards into the pressure maximum.

Massive planets are known to create a pressure maximum by pushing matter out of their orbit. This creates an inner and outer edge, where dust can be caught and collected. But this can not solve the problem how planets are created in the first place. Another way to create pressure maxima are vortices. If the vortex is strong enough it also creates a maximum in the pressure that collects dust. This opens the question how the vortex is formed, which brings us back to the details of the accretion disk dynamics. The earlier mentioned Rossby wave instability and the subcritical baroclinic instability are candidates for this, but also the vertical shear instability may create vortices (Richard et al., 2016).

A different way to save the dust from the rapid inward drift may come from the dust

itself. If the dust is well mixed with the gas, it has only a small impact on the gas due to its small mass fraction of only 1%. But this changes if the dust is able to collect in a small region until there is more dust than gas. Then, instead of just being slowed done by the gas, the dust can also accelerate the gas to Keplerian velocity. A small overdensity in the dust may be created by larger dust grains settling to the midplane or, as we will show in this work, due to the vertical shear instability. But these processes alone can not create overdensities strong enough to stop inward drift.

This leads us to the streaming instability discovered by Youdin and Johansen (2007). The necessary conditions for this instability are a dust to gas ratio of one to ten, which is an increase in the initial dust density of a factor of ten. Additionally, the dust should have a stopping time in the order of the time for one orbit. If a small cluster of dust moves together through the gas, its combined drag force will accelerate the gas around it up to the velocity of the cluster. This creates a small patch of gas that moves faster than the surrounding gas. This allows the dust cluster to travel through the gas faster than smaller dust clusters, allowing the cluster to catch up to other clusters. These will then be added to the larger cluster, strengthening the effect. This way massive clusters can form, which are no longer slowed done by the drag from the gas.

Independent of the process that leads to the large dust clump, a gravitational collapse may occur, if enough dust is collected into a small region. In contrast to gas clumps, the gravitational force on the dust only has to overcome the shear of the disk and not a pressure gradient, which can only support gas against collapse. This skips the tedious growth of the grains by numerous collisions and can directly create planetesimals, which are km sized bodies. These planetesimals then can sweep up smaller dust particles and other planetesimals due to their no longer negligible gravitational attraction. This leads to an oligarchic growth phase (Kokubo and Ida, 1998), where a few planetesimals quickly grow to the size of planets, ending this phase of planet formation.

Observations

A major source for information on dust in protoplanetary disks are meteorites found on Earth, which can tell us about the history of our own Solar System. This reveals for example that the first CAIs were formed in the inner region of the disk 4567 Myr

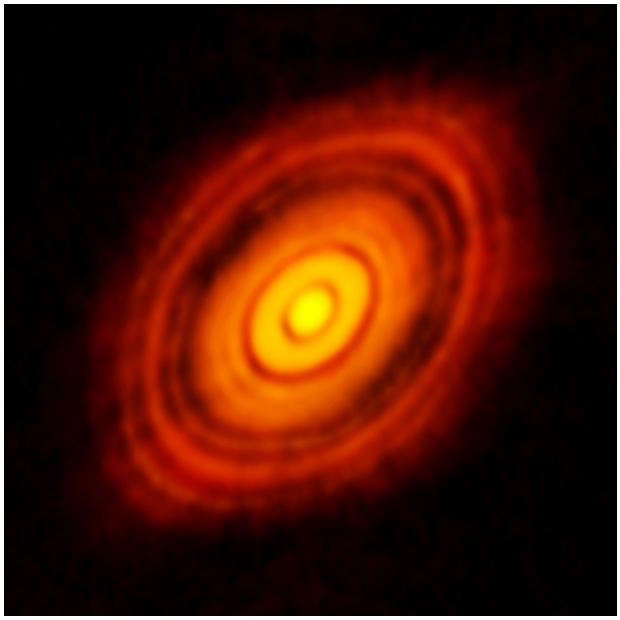

Figure 1.1: Image of HL Tau in the submillimeter wavelength taken by ALMA. Source: ALMA Partnership et al. (2015).

ago (see e.g. Weidenschilling and Cuzzi, 2006, Krot et al., 2009), which is very close to the formation of the Solar System. Surprisingly, they did not quickly migrate through the disk into the Sun, but spread, most likely due to turbulent diffusion, throughout the disk. A second class of inclusions that is often found in meteorites, the chondrules, formed 1-3 Myrs later in sudden heating events. This gives an interesting insight into the dynamics of a protoplanetary disk. Not only happened dust growth for the first time very early, it also not completely depleted the dust from the disk. Furthermore there is at least another dust growth phase 1-3 Myrs later, which is important for asteroid and probably also planetesimal formation.

Another source are observations of extrasolar planetary systems. Observations of dust are easier than in the visible light, since the wavelength is in the millimeter range, making it possible to connect telescopes with interferometry to one large telescope with higher resolution. Nowadays the resolution of these telescopes is finally high enough to resolve at least the coarse structure of an accretion disk. A famous image of HL Tau is shown in Fig. 1.2. It was taken by the Atacama Large Millimeter/submillimeter Array (ALMA) and shows the disk of HL Tau with an unexpectedly

large number of ring structures. Since the system is most likely less than 1 Myr old, it is not clear if these rings can be explained with already forming planets, or should be explained by other effects like a gravitational instability or snow lines.

1.3 Planet formation and migration

The clearest evidence of planet formation are the planets themselves. While a few planets are visible with the naked eye, other planets in our Solar System can only be seen with the help of a telescope and it is even today unclear if a ninth planet exists. Despite our ignorance of our own system it is nowadays possible to detect planets outside our own Solar System. These planets are called exoplanets.

There are several methods for the detection of exoplanets. Since planets are much smaller than stars, most methods focus on analyzing the star and then deduce the existence of planets indirectly. The first effective method makes use of the motion of a star which is induced by the gravitational interaction of the planet with the star. Just as planets orbit the combined center of mass, the star also orbits around this center albeit with a much smaller orbit, because the mass of the star usually dominates the mass in the star system by several orders of magnitude. For example our own Sun moves with approximately 13 m/s due to the motion of Jupiter, the heaviest planet in our system. This seemingly small velocity can be detected by analyzing the spectrum of the star. The relative velocity of the star with respect to the observer will add a Doppler shift to the spectrum, which can be measured to a very high accuracy by the position of known absorption lines. From the periodic changes in the Doppler shift even the presence of multiple exoplanets can be deduced.

Another successful method depends more on chance, since a specific alignment of the star system to the observer is needed. For this method the planet needs to cross in front of the star, occulting a fraction of the star from the observer. This leads to a decrease in brightness of the star. This methods has the advantage that the radius of the planet can be calculated, which allows to estimate the density and gives thus an insight into the planet formation scenario.

In rare cases even direct imaging is possible. Those systems need to be close to the observer, in order to be resolvable by the telescope and the planet should be massive

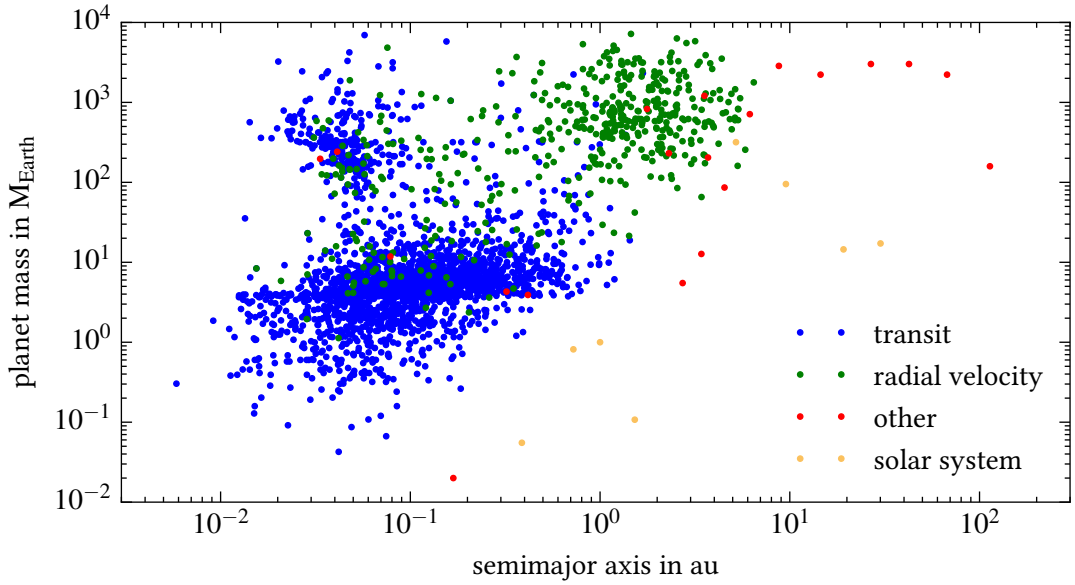

Figure 1.2: Discovered exoplanets and the planets in the Solar System. Data is from `http://exoplanets.org` (state Feb. 2017, see Han et al. (2014)). Most exoplanets were found in the last few years due to the Kepler mission.

with a wide separation, since the light reflected by the planet and its internal luminosity will only be faint in comparison to the glare due to the intense emission of star.

Another method uses gravitational microlensing. Here the observed system moves over an additional star in the background. The gravity of the observed system then acts as an optical lens, focusing the light of the background star onto the observer. While the alignment happens only rarely and only for a short time, preventing repeated observation and confirmation, this method has the advantage of working even for Earth mass planets.

The first confirmed detection of an exoplanet occurred in 1992. The detection method made advantage of the fact that the host star is a millisecond pulsar. The very precise timing of the pulsar is disturbed by the planet orbiting around the star, similar to the radial velocity method.

Since then, a high number of planets have been detected. In Fig. 1.2 the mass of the discovered planets depending on their semimajor axis is shown and compared the planets in our own Solar System. It is immediately clear that there are three clusters in the figure. This clustering does not necessarily correspond to a clustering in the

occurrence rates of this type of planets. Instead they may be created by strong observation biases due to the detection technique. For example the detection by radial velocity does not replicate the clustering in the detection with the transit method. It is also clear that currently no method can detect planets in the lower right area, into which the planets in the Solar System fall.

Nevertheless the clusters correspond roughly to different types of planets. The planets in the lower left region with a mass smaller than ten Earth masses are the Earth-like planets and the super-Earths. In this region we can find habitable planets. To be considered as habitable, they also need a distance to the star that allows water to be liquid on the planet's surface. It has been estimated from their numerous detection that at least half of the sun-like stars will have a planet in this cluster.

In the upper right corner we find the gas giant planets, which are similar to Jupiter. These are expected to be formed by either gravitational collapse or by runaway gas accretion. There a small rocky core starts to accrete gas until the gas atmosphere is heavier than the core. At this point the planet can accrete from the surrounding gas disk very quickly, until it creates a gap.

The exoplanets in the cluster in the upper left corner are so-called Hot Jupiters. They are similar to Jupiter, but are much closer to their host star. Hence, the star will heat them to high temperatures. While it is possible that they formed this close to the star, it is more likely that they migrated through the gas disk to this position. Migration will typically occur for all planet, hence no planet will end up where they have initially formed.

The process for migration of planets has nothing to do with the migration of dust. The latter is slowed down due to the drag force. Planets are far too massive in relation to their radius, to be influenced by the gas drag. Even the much smaller planetesimals can move through the disk without being slowed down by the drag. Instead the migration is only due to the gravitational interaction between the planet and the disk.

Even small planets will perturb the disk with their gravitational potential. Due to the Keplerian rotation these perturbations are sheared into spiral arms. The inner spiral will be in front of the planet and the outer spiral will be behind the planet. Since the density inside the spiral arms is increased relative to the unperturbed disk, these arms will pull the planet in their direction, exerting a torque onto the planet. These torques

are called the Lindblad torques. Since they pull in opposite directions, they will mostly cancel out each other. The details of the torque balance will depend on properties like the density and temperature gradient (D'Angelo and Lubow, 2010), but in general the outer arm behind the planet will be stronger, leading to inward migration. This kind of migration is called type I migration.

If the planet is massive enough it can carve a gap in the disk. This occurs when the angular momentum the gas gained, or lost, due to the interaction with planet is not carried away quick enough. The gas then seems to be pushed out of the corrotation region by the planet. In principle this process works also for low mass planets, but the timescale will be too long for the effect to be noticeable, especially when the viscosity is not extremely low. Since the gap reduces the density in the spiral arms, a planet that migrates to the inner edge of the gap reduces the torques of the outer arm, thus halting the inward migration. The same would happen for outward migration. Thus a planet siting in a gap can now no longer escape it and migration depends on how fast it can move the gap through the disk. This is called type II migration.

Finally, for planets between type I and II migration in disks that are close to being gravitational unstable (Masset and Papaloizou, 2003), the migration of the planet can lead to an asymmetric surface density in the co-orbital region. This asymmetry can increase the inward migration rate. Since the asymmetry also increases with the migration rate, this can lead to runaway migration, where the planet migrates inwards on a timescale of 300 orbits.

2 Aims and Objectives

The aim of this dissertation is to examine the effects of turbulence on the evolution of dust and planets. While there are different sources for turbulence in an accretion disk, we focus in this work on turbulence generated by the vertical shear instability (VSI). We chose the VSI because the VSI is a strong candidate for angular momentum transport in the dead zone and it might have unique effects on the dust and planets due to the global modes in the velocity field.

In general we use the *PLUTO*-Code developed by Mignone et al. (2007) to integrate the Navier-Stokes equations. We begin with two-dimensional axisymmetric simulations, to explore the strength and time scale of the VSI. To enable a more realistic disk model we extended the Code with a radiation transport module witch uses the flux limited diffusion approximation and was developed by Kolb et al. (2013).

To explore the impact of the VSI on the dust particles, we develop a module for Lagrangian particles. For each particle we solve the differential equation of motion, which includes the gravity of the star and the feedback from the gas via the drag force. We add those particles to our VSI model and extend the simulation to three dimensions to include effects that can be created by vortices. For this model we analyze dust settling, migration, clustering and the relative velocities.

Finally, we investigate the effect of the turbulent viscosity of the VSI on planets and their migration. We add planets of different sizes into a disk with VSI activity and compare to a laminar model, which is the same model, but with kinematic viscosity instead of VSI activity. This allows us to measure the effect of turbulent viscosity on vortices and the torques acting on the planet. We also study the perturbations of the surface density due to the planets.

3 Publications

Publications published in A&A:

Stoll and Kley (2014):
Vertical shear instability in accretion disc models with radiation transport

Stoll and Kley (2016):
Particle dynamics in discs with turbulence generated by the vertical shear instability

Stoll, Kley and Picogna (2017):
Anisotropic hydrodynamic turbulence in accretion disks

Publication submitted to A&A:

Stoll, Picogna and Kley:
Planet-disc interaction in laminar and turbulent discs

Statement of own contribution

For all publications I worked together with my supervisor Prof. Dr. Wilhelm Kley. For the last two papers, we also collaborated with Dr. Giovanni Picogna. All the data was collected by me and the analysis was done by myself, except for the last publication, where Dr. Picogna contributed the data for the models with viscosity. Concerning the writing of the publications, in the first two publications most writing was done by myself, except for the introductions, which are mostly written by Prof. Kley and conclusions, which are in equal parts written by Prof. Kley and myself. In the third publication I wrote the sections concerning the simulations and the results, while Prof.

Kley provided the section on the theoretical model of the viscosity and most of the introduction and conclusions. Finally, in the last publication, I wrote again most of the sections concerning the simulations and the results, while Dr. Picogna provided most of the introduction and large parts of the discussion and conclusion.

A&A 572, A77 (2014)
DOI: 10.1051/0004-6361/201424114

Astronomy & Astrophysics

Vertical shear instability in accretion disc models with radiation transport

Moritz H. R. Stoll and Wilhelm Kley

Institut für Astronomie und Astrophysik, Universität Tübingen, Auf der Morgenstelle 10, 72076 Tübingen, Germany
e-mail: moritz.stoll@student.uni-tuebingen.de;wilhelm.kley@uni-tuebingen.de

Received 2 May 2014 / Accepted 24 September 2014

ABSTRACT

Context. The origin of turbulence in accretion discs is still not fully understood. While the magneto-rotational instability is thought to operate in sufficiently ionised discs, its role in the poorly ionised protoplanetary disc is questionable. Recently, the vertical shear instability (VSI) has been suggested as a possible alternative.
Aims. Our goal is to study the characteristics of this instability and the efficiency of angular momentum transport, in extended discs, under the influence of radiative transport and irradiation from the central star.
Methods. We use multi-dimensional hydrodynamic simulations to model a larger section of an accretion disc. First we study inviscid and weakly viscous discs using a fixed radial temperature profile in two and three spatial dimensions. The simulations are then extended to include radiative transport and irradiation from the central star.
Results. In agreement with previous studies, for the isothermal disc we find a sustained unstable state with a weak positive angular momentum transport of the order of $\alpha \approx 10^{-4}$. Under the inclusion of radiative transport the disc cools off and the turbulence terminates. For discs irradiated from the central star we again find a persistent instability with a similar α value as for the isothermal case.
Conclusions. We find that the VSI can indeed generate sustained turbulence in discs, albeit at a relatively low level with α about few times 10^{-4}.

Key words. hydrodynamics – instabilities – accretion, accretion disks – radiative transfer

1. Introduction

The origin of the angular momentum transport in accretion discs is still not fully understood. Observationally it has been confirmed that the molecular viscosity is by many orders of magnitude too small to explain the effective mass and angular momentum transport in discs (Pringle 1981). This can be inferred for example from time variations in the disc luminosity in close binary systems, or by correlating the infrared-excess caused by discs around young stars with the age of the system. As a consequence it is assumed that discs are driven by some kind of turbulent transport whose cause is still not known. Despite its unknown origin, the efficiency of the turbulence is usually parameterised in terms of the dimensionless parameter, α, as introduced by Shakura & Sunyaev (1973). Observationally, values of a few times 10^{-3} as in protostellar discs to 10^{-1} for discs in close binary stars are suggested. For sufficiently well ionised discs the magnetorotational instability (MRI) is certainly the most promising candidate to provide the transport (Balbus 2003). While this may be true for the hot discs in close binary systems or in active galactic nuclei, there is the important class of protostellar discs where at least the thermal ionisation levels are too low to provide a sufficient number of charged particles that can support the MRI (Armitage 2011). In such discs turbulence plays an important role in several aspects. Not only does it determine the lifetime of an accretion disc, but it also influences where and how planets can form and evolve in the disc. A variety of sources such as stellar X-rays, cosmic rays or collisions with beta particles from radioactive nuclei have been invoked to provide the required ionization levels, but recent studies indicate the presence of an extended dead zone where, because of the lack of ionization, no magnetically driven instability may operate. Additionally, recent studies on the origins of turbulence in protostellar discs that include non-ideal magnetohydrodynamical (MHD) effects such as ambipolar diffusion or the Hall effect, indicate that the MRI may even be suppressed strongly in these discs, see the review by Turner et al. (2014) and references therein.

As a consequence, alternative mechanisms that provide turbulence are actively discussed. Typical examples for non-magnetised discs are convective instability (Ruden et al. 1988), gravitational instability (Lin & Pringle 1987), or baroclinic instability (Klahr & Bodenheimer 2003), for further references see Nelson et al. (2013). While any of these may operate under special conditions in the disc, e.g. suitable radial entropy gradients or a sufficiently high disc mass, none seems to have general applicability. Searching for alternatives two linear instabilities have been recently discussed in the literature, both acting on the radial temperature structure of the disc. One is a convective overstability that preferably acts for thermal relaxation times close to the orbital period (Klahr & Hubbard 2014; Lyra 2014), and two is a vertical shear instability (VSI) that

A&A 572, A77 (2014)

operates best for cooling times much shorter than the orbital period or for discs that are adiabatically stratified in the vertical direction. The present paper focuses on the latter instability. Here, the instability is caused by a vertical gradient of the angular velocity, Ω, in the disc. Through linear analysis it has been shown that for a sufficiently strong vertical shear there are always modes that can overcome the stabilizing angular momentum gradient (Rayleigh-criterion) and generate instability (Urpin & Brandenburg 1998; Urpin 2003). This instability is related to the Goldreich-Schubert-Fricke instability that can occur in differentially rotating stars (Goldreich & Schubert 1967; Fricke 1968).

Concerning vertical shears effectiveness with respect to angular momentum transport numerical simulations were performed by Arlt & Urpin (2004) and Nelson et al. (2013). The first authors analysed the instability for globally isothermal discs and found that the instability in this case could only be triggered by applying finite initial perturbation because the equilibrium state of the disc (being strictly isothermal) did not contain a shear in Ω. The maximum values of α obtained by Arlt & Urpin (2004) were around 6×10^{-6}, but the turbulence was decaying in the long run. Nelson et al. (2013) extended these simulations and performed high resolution simulations of the VSI for so-called locally isothermal discs that contain a radial temperature gradient, but are vertically isothermal. Under these conditions the equilibrium state has a vertical gradient in the shear and indeed an instability sets in. As shown by Nelson et al. (2013) the instability has two distinct growth phases, it starts from the surface layers of the disc where the shear is strongest and then protrudes towards the midplane. In the final state the vertical motions in the disc are antisymmetric with respect to the disc's midplane, such that the gas elements cross the midplane, a feature found for the vertical convective motions in discs as well (Kley et al. 1993). For the efficiency of the VSI induced turbulence Nelson et al. (2013) found a weak angular momentum transport with $\alpha = 6 \times 10^{-4}$. They also showed that in the presence of a small viscosity or thermal relaxation the instability is weaker and can easily be quenched.

It is not clear what influence radiation transport will have on this instability. Without external heat sources one might expect that, because of radiative cooling and the dependence of the instability on temperature, the instability will die out. Here, we evaluate the evolution of the instability for radiative discs and an ideal equation of state. Additionally, we extend the radial domain and include irradiation from the central star. We perform 2D and 3D hydrodynamical simulations including radiative transport.

This paper is organised as follows. In Sect. 2, we present the physical setup of our disc models and in Sect. 3 the numerical approach. The isothermal results are presented in Sect. 4, followed by the radiative cases in Sect. 5. Stellar irradiation is considered in Sect. 6 and in Sect. 7 we conclude.

2. Physical setup

In order to study the VSI of the disc in the presence of radiative transport we construct numerical models solving the hydrodynamical equations for a section of the accretion disc in two and three spatial dimensions.

2.1. Equations

The basis our studies are the Euler Eqs. (1)–(3) describing the motion of an ideal gas. These are coupled to radiation transport (4) for which we use the two temperature approximation applying flux-limited diffusion. The equations then read

$$\frac{\partial \rho}{\partial t} + \nabla(\rho \boldsymbol{u}) = 0 \tag{1}$$

$$\frac{\partial}{\partial t}\rho \boldsymbol{u} + \nabla(\rho \boldsymbol{u}\boldsymbol{u}) + \nabla p = \rho \boldsymbol{a}_{\rm ext} \tag{2}$$

$$\frac{\partial}{\partial t} e + \nabla[(e+p)\boldsymbol{u}] = \rho \boldsymbol{u} \boldsymbol{a}_{\rm ext} - \kappa_{\rm P} \rho c (a_{\rm R} T^4 - E) \tag{3}$$

$$\frac{\partial}{\partial t} E + \nabla \boldsymbol{F} = \kappa_{\rm P} \rho c \left(a_{\rm R} T^4 - E\right). \tag{4}$$

Here ρ is the density; $\boldsymbol{u}$ the velocity; e the total energy density (kinetic and thermal) of the gas; p denotes the gas pressure; the acceleration due to external forces, such as the gravitational force exerted by the central star is given by $\boldsymbol{a}_{\rm ext}$; and E and $\boldsymbol{F}$ are the energy density and the flux of the radiation. The last terms on the righ-hand side of Eqs. (3) and (4) refer to the coupling of gas and radiation, i.e. the heating/cooling terms. Here, c stands for the speed of light, $a_{\rm R}$ is the radiation constant, and $\kappa_{\rm P}$ the Planck mean opacity.

We close the equations with the ideal gas equation of state

$$p = (\gamma - 1) e_{\rm th}, \tag{5}$$

where $e_{\rm th} = e - 1/2 \rho u^2$ is the thermal energy density. The temperature of the gas is then calculated from

$$p = \rho \frac{k_{\rm B} T}{\mu m_{\rm H}}, \tag{6}$$

where μ is the mean molecular weight, $k_{\rm B}$ the Boltzmann constant, and $m_{\rm H}$ the mass of the hydrogen atom. In our simulations with radiation transport we use $\gamma = 1.4$ and $\mu = 2.35$. To compare to previous studies we performed additional isothermal simulations where we use $\gamma = 1.001$ and additionally reset to the original temperature profile in every step. This procedure corresponds to an isothermal simulation, but allows for an arbitrary temperature profile. It also allows to use the feature of slowly relaxing to a given original temperature such as used for example in Nelson et al. (2013). Note that without resetting the temperature the gas remains adiabatic, and the perturbation will die out for our setup.

The radiation flux in the flux-limited diffusion (FLD) approximation (Levermore & Pomraning 1981) is given by

$$\boldsymbol{F} = -\lambda \frac{c}{\kappa_{\rm R} \rho} \nabla E, \tag{7}$$

where $\kappa_{\rm R}$ is the Rosseland mean opacity and λ is the flux-limiter, for which we use the description of Minerbo (1978). For the Rosseland mean opacity we apply the model of Bell & Lin (1994). For simplicity, in this initial study we use the same value for the Planck mean opacity, see also Bitsch et al. (2013).

In some of our studies we add viscosity and stellar irradiation to the momentum and energy equations. This will be pointed out below in the appropriate sections.

2.2. Disc model

To be able to study the onset of the instability we start with a reference model in equilibrium. For this purpose, we follow Nelson et al. (2013) and use a locally isothermal disc in force equilibrium, where for the midplane density we assume a power law behaviour

$$\rho(R, Z = 0) = \rho_0 \left(\frac{R}{R_0}\right)^p, \tag{8}$$

and that the temperature is constant on cylinders

$$T(R,Z) = T_0 \left(\frac{R}{R_0}\right)^q . \tag{9}$$

To specify the equilibrium state we have used a cylindrical coordinate system (R, Z, ϕ). However, our simulations will be performed in spherical polar coordinates (r, θ, ϕ) because they are better adapted to the geometry of an accretion disc. In Eqs. (8) and (9), ρ_0 and T_0 are suitably chosen constants that determine the total mass content in the disc and its temperature. The exponents p and q give the radial steepness of the profiles, and typically we choose $p = -3/2$ and $q = -1$. Assuming that in the initial state there are no motions in the meridional plane and the flow is purely toroidal, force balance in the radial and vertical directions then leads to the equilibrium density and angular velocity profiles that we use for the initial setup (Nelson et al. 2013)

$$\rho(R,Z) = \rho_0 \left(\frac{R}{R_0}\right)^p \exp\left[\frac{GM}{c_s^2}\left(\frac{1}{\sqrt{R^2+Z^2}} - \frac{1}{R}\right)\right], \tag{10}$$

and

$$\Omega(R,Z) = \Omega_K \left[(p+q)\left(\frac{H}{R}\right)^2 + (1+q) - \frac{qR}{\sqrt{R^2+Z^2}}\right]^{\frac{1}{2}} . \tag{11}$$

Here, $c_s = \sqrt{p/\rho}$ denotes the isothermal sound speed, $\Omega_K = \sqrt{GM_\odot/R^3}$ the Keplerian angular velocity, and $H = c_s/\Omega_K$ is the local pressure scale height of the accretion disc. We note that the Z dependence of Ω in the equilibrium state is the origin of the VSI because the vertical shear provides the opportunity for fluid perturbations with a wavenumber ratio k_R/k_Z above a threshold to tap into a negative gradient in the angular momentum as the perturbed fluid elements move away from the rotation axis (Nelson et al. 2013). The angular velocity given by Eq. (11) is also used to calculate the Reynolds stress tensor, for details see below.

2.3. Stability

Nelson et al. (2013) repeated the original analysis in Goldreich & Schubert (1967) for a locally isothermal and compressive gas for an accretion disc using the local shearing sheet approximation at a reference radius r_0. They derived the same stability criterion as Urpin (2003) and obtained the following growth rate of the instability

$$\sigma^2 = \frac{-\kappa_0^2(c_0^2 k_Z^2 + N_0^2) + 2\Omega_0 c_0^2 k_R k_Z \frac{\partial \bar{V}}{\partial z}}{c_0^2(k_Z^2 + k_R^2) + \kappa_0^2 + N_0^2}, \tag{12}$$

where κ_0 is the epicyclic frequency, c_0 the sound speed, and N_0 is the Brunt-Vaisaila frequency at the radius r_0; $\bar{V}$ denotes the mean deviation from the Keplerian azimuthal velocity profile, and k_R and k_Z are the radial and vertical wavenumbers of the perturbations in the local coordinates.

For negligible N_0, small H_0/R_0, and $k_Z/k_R \sim O(qH_0/R_0)$, as seen in their numerical simulations, Nelson et al. (2013) find

$$\sigma \sim q\Omega\frac{H}{R}, \tag{13}$$

which implies that the growth rate per local orbit to first order depends on the temperature gradient as given by q and on the absolute temperature, because of H/R. We will compare our numerical results with these estimates.

3. Numerical model

To study the VSI in the presence of radiative transport we perform numerical simulations of a section of an accretion disc in two and three spatial dimensions using spherical polar coordinates (r, θ, ϕ), and a grid which is logarithmic in radial direction, keeping the cells squared. We solve Eqs. (1) to (4) with a grid-based method, where we use the PLUTO code from Mignone et al. (2007) that utilises a second-order Godunov scheme, together with our radiation transport (Kolb et al. 2013) in the FLD approximation, see Eq. (7).

The simulations span a region in radius from $r = 2-10$ AU, this is the range where the dead zone can be expected (Armitage 2011; Flaig et al. 2012). Here, we use a larger radial domain as Nelson et al. (2013) did because we intend to study the global properties of the instability over a wider range of distances. Additionally, this larger range is useful because we need some additional space (typically $\approx$1 AU) to damp possible large scale vortices in the meridional plane that show up at the inner radial boundary of the domain (see below). The origin of these vortices is possibly that the instability moves material along cylindrically shaped shells, a motion that is not adapted to the used spherical coordinates, such that the midplane is cut out at the inner boundary. Vortices can also arise if the viscosity changes apruptly, a situation mimicking a boundary. Additionally, in some cases the wavelengths are large, such that the coupling between different modes cannot be captured in a small domain. We also use a wide range because with radiation transport the growth rates are expected to depend on the opacity, which is a function of ρ and T and thus of the radius. In the meridional direction (θ) we go up to $\pm$5 scale heights above and below the equator in the isothermal case, and we use the same extension for the radiative simulation, where it corresponds to more scale heights. For the 3D simulations we used in the azimuthal direction (ϕ) a quarter circle, from 0 to $\pi/2$.

We use reflective boundaries in the radial direction. In the meridional direction we use outflow conditions for the flow out of the domain and reflective conditions otherwise. For the radiation transport solver we set the temperature of the meridional boundary to 10 K, which allows the radiation to escape freely. We use damping of the velocity near the inner radial boundary within 2–3 AU to prevent the creation of strong vortices arising through the interaction with the reflecting boundary, which can destroy the simulation. This is done by adding a small viscosity of $\nu = 2\times10^{-7}$ with a linear decrease to zero from 2 AU to 3 AU (similar to the damping used in de Val-Borro et al. 2006).

We assume that the disc orbits a solar mass star and we apply a density of $\rho_0 = 10^{-10}$ g/cm^3 at 1 AU. Because the surface density decays with $r^{-0.5}$, we get a surface density $\Sigma = 80$ g/cm^2 at 5 AU. To study the mass dependence we vary ρ_0 for the radiative models. To seed the instability we add a small perturbation of up to 1% of the sound speed to the equilibrium velocity, see Eq. (11).

Because our radiation transport solver is only implemented in full 3D (Kolb et al. 2013), we use two grid cells in the azimuthal direction for the 2D axisymmetric simulations using radiation transport.

4. Isothermal discs

Before studying full radiative discs, we first perform isothermal 2D simulations to compare our results and growth rates to those of Nelson et al. (2013). Then we will extend the simulation to

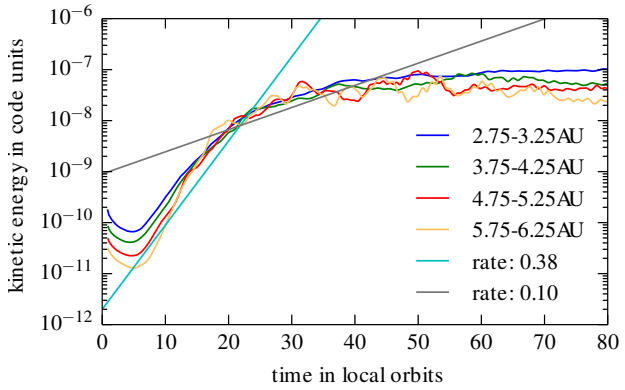

Fig. 1. Kinetic energy of the motion in the meridional plane at different radii in an inviscid disc. The kinetic energy at the different locations is in each case averaged over a radial interval with length 0.5 AU. We note that the unit of time is given in local periods at the centre of the specified interval. Hence, it is different for each curve, but this allows easy comparison.

full 3D using a quarter of a disc and discuss the dependence on resolution and viscosity.

4.1. Growth rates

To analyse the possible growth and instability of the initial equilibrium state, we analyse the time evolution of the kinetic energy in the meridional plane

$$e_{\rm kin} = \frac{1}{2}\rho\left(u_r^2 + u_\theta^2\right), \tag{14}$$

at different radii. The obtained growth of $e_{\rm kin}$ of a run with $q = -1$ and $p = -3/2$ is shown at different radii in Fig. 1 for an inviscid disc model with a grid resolution of 2048×512. We note that the time is measured in local orbits ($2\pi/\Omega(r_i)$) at the corresponding centres of the intervals, r_i. We measure a mean growth rate of 0.38 per orbit for the kinetic energy (light blue line in Fig. 1), which is twice the growth rate (σ) of the velocity. We calculate the growth rate by averaging the kinetic energy at the different r_i over an interval with length 0.5 AU. Our results compare favourably with the growth rates from Nelson et al. (2013) who obtained 0.25 per orbit averaged over 1−2 AU for $q = -1$. Averaging over this larger range leads to a reduced growth because the rate at 2 AU, measured in orbits at 1 AU, is smaller by a factor of $2^{1.5} = 2.8$, and so their result is a slight underestimate.

A closer look at Fig. 1 reveals two distinct growth phases. An initial strong linear growth phase with a rate of 0.38 per orbit lasting about 20 local orbits, and a slower second phase with a rate of 0.10 per orbit (grey line in Fig. 1). To understand these regimes, we present in Fig. 2 the velocity in the meridional direction, u_θ, in 2D contour plots at different times. The top panel reveals that the first phase corresponds to symmetric (mirror symmetry with respect to the equatorial plane) disturbances that grow from the top and bottom surface layers of the disc. Here, the gas does not cross the midplane of the disc. When the disturbances meet in the disc's midplane they develop an anti-symmetric phase with lower growth rates where the gas flow crosses the midplane of the disc as shown in the middle panel. The converged phase shown in the lower panel then shows the fully saturated global flow. Figure 2 indicates that in the top panel the whole domain is still in the anti-symmetric growth phase, in the middle panel only the smaller radii show symmetric

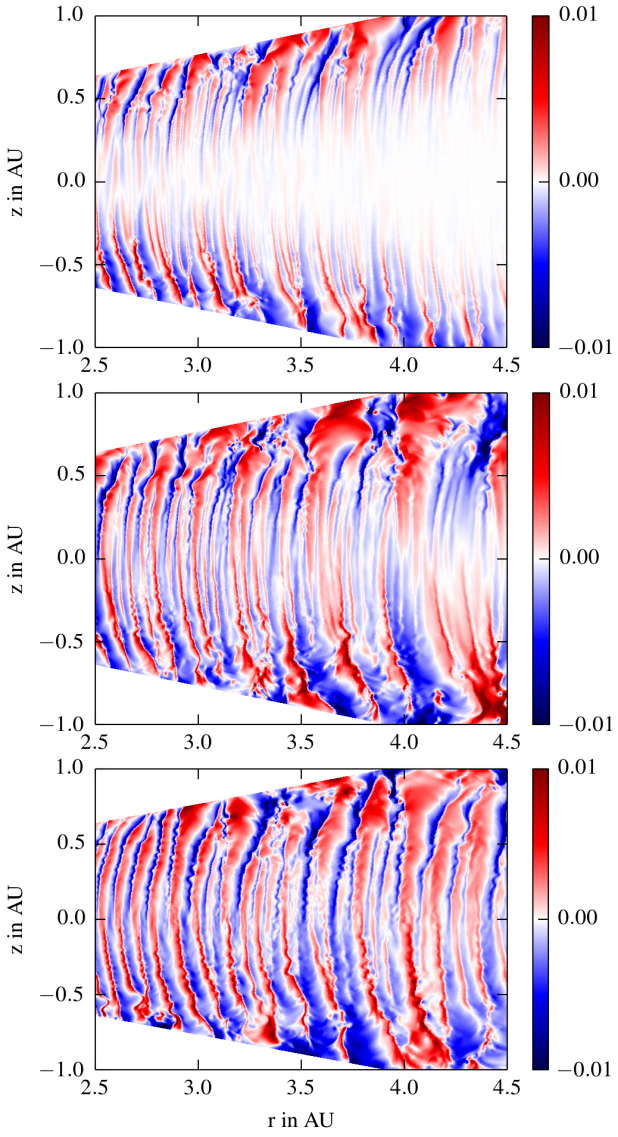

Fig. 2. Velocity in the meridional direction, u_θ, in units of local *Kepler* velocity for an isothermal run without viscosity. The panels refer to snapshots taken at time 100, 210 and 750 (*top to bottom*), measured in orbital periods at 1 AU. In units of local orbits at (2.5, 3.5, 4.5) AU this refers to (25, 15, 10) (53, 32, 22) (190, 115, 79) orbits, *from top to bottom*.

growth, while in the lower panel the whole domain has reached the final equilibrium, in accordance with Fig. 1.

We point out that the growth rate per local orbit ($\sim\sigma/\Omega$) is independent of radius in good agreement with the relation (13), for constant H/R. We will show later that the growth rate is also independent of resolution.

4.2. Comparison to 3D results and Reynolds stress

In addition to the 2D simulation we ran an equivalent 3D case using a quarter of a disc with a resolution of 512×128×128 grid cells. We will use this to discuss the validity of the 2D results, in particular the estimates on the turbulent efficiency factor α. In Fig. 3 we compare the growth of the meridional kinetic energy for the 3D and the 2D simulation. After a slower start, the

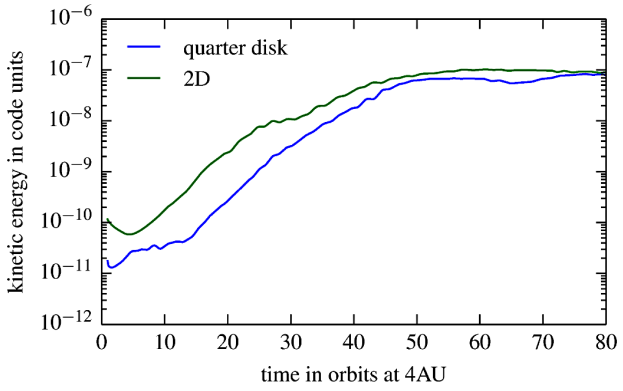

Fig. 3. Growth of the kinetic energy for the quarter of a disc and the 2D equivalent. The kinetic energy is averaged from 4 AU to 5.5 AU.

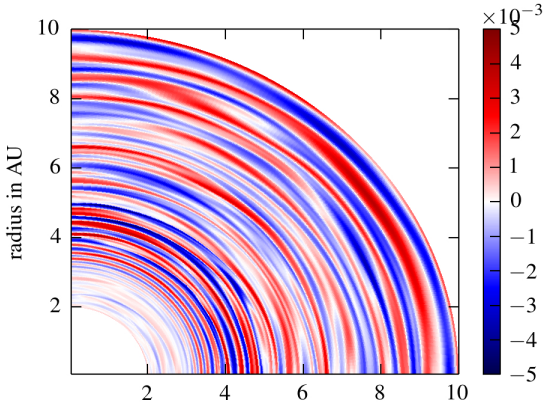

Fig. 4. Vertical velocity in the midplane of the disc for the 3D model after 4000 orbits. The nearly axisymmetric property of the instability is clearly visible.

3D simulation shows very similar growth and reaches the same final saturation level.

To estimate any possible angular momentum transfer caused by the turbulent motions induced by the instability we calculate the corresponding Reynolds stress (Balbus 2003)

$$T_{r\phi} = \frac{\int \rho \delta u_r \delta u_\phi \mathrm{d}V}{\Delta V} = \left\langle \rho \delta u_r \delta u_\phi \right\rangle, \tag{15}$$

where δu_r and δu_ϕ are defined as the fluctuations of the velocity field from the mean flow and ΔV is the volume of the integrated domain. To calculate a coordinate dependent stress we integrate only over thin slices with a thickness of one cell in the apropriate direction. While δu_r is just the radial velocity, u_r, at the point of interest because the initial u_r was zero, δu_ϕ is difficult to calculate, as one has to subtract the mean background rotational velocity. Armitage (2011) defines it as the difference to the *Kepler* rotation, while strictly speaking it is the deviation from the unperturbed equilibrium state that is not Keplerian in our case, see Eq. (11). In 3D simulations it is mostly calculated by averaging over the azimuthal direction (Flock et al. 2011; Fromang & Nelson 2006), but this instability is nearly axisymmetric (see Fig. 4), so this is not appropriate here and the correct way is to average over time to obtain the steady-state velocity. However, this is computationally inconvenient because this time average is not known a priori. In Fig. 5 we show that the time averaging method leads to the same results as the equilibrium method using the analytic Eq. (11), and we use the latter for our subsequent simulations.

To calculate the dimensionless α-parameter, $T_{r\phi}$ has to be divided by the pressure. To show the radial and vertical dependence of α it is useful to use different normalisations. We divide the Reynolds stress in Eq. (15) by the midplane pressure to illustrate the dependence on the meridional (vertical) coordinate, thus making it independent of the number of scale heights of the domain. The stress as a function of the radius, $T_{r\phi}(R)$, is divided by the vertical averaged pressure, making it again independent of the numbers of scale heights. This procedure corresponds to a density weighted height integration (Balbus 2003).

In Fig. 5 we present the different methods for calculating the Reynolds stress, $T_{r\phi}$, for the simulation of a quarter of a disc with a resolution of $512 \times 128 \times 128$ and the same initial conditions as in the 2D case. We can see that indeed the axisymmetric property of the instability leads to incorrect results if one only averages over the azimuthal direction. All further results for the isothermal discs are calculated with the equilibrium method. This allows us to approximate the Reynolds stress

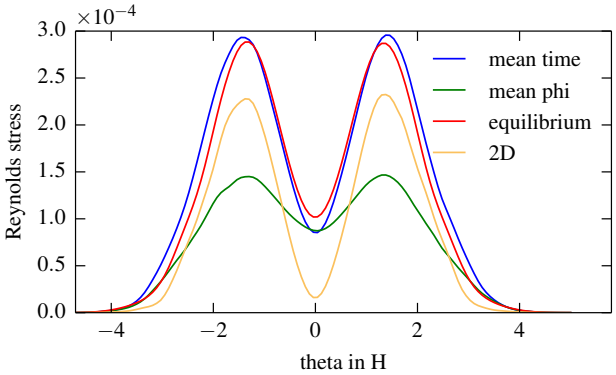

Fig. 5. Reynolds stress (code units) from 3−10 AU averaged over 41 time steps, each step 100 orbits apart beginning with orbit 1000, calculated with different averaging methods. For "mean time" the steady-state $\bar{u}_\phi = u_\phi - \delta u_\phi$, needed to calculate the Reynolds stress at each step, was calculated through averaging over the 41 time steps. For "mean phi" the steady-state velocity was calculated by averaging over the azimuthal direction at each time step. For "equilibrium" $\bar{u}_\phi$ is calculated analytically by using the equilibrium Eq. (11) at each step. For the 2D model we used the equilibrium method as well.

even in a transient disc and calculate the stress continuously during the whole runtime of the simulation, strongly reducing the amount of data needed to be written to the hard drive because the Reynolds stress can now be calculated independent of the other time steps. In addition, the computations show that the stresses of the reduced 2D simulations yield stresses comparable to the full 3D case and can be used as a proxy for the full 3D case. In Fig. 4 we show the vertical velocity in the midplane of the disc for the 3D model. As shown, the motions are only very weakly non-axisymmetric.

4.3. Resolution

In this section we look at the effect of resolution. We start with a resolution of 256×64, where the instability exists, but clearly is not resolved, and go by doubling the resolution in several steps up to a resolution of 2048×512, where the computations start to be expensive. In Fig. 6 we show on the left the Reynolds stress divided by the midplane pressure as a function of vertical distance. This is then averaged over the radius from 3−8 AU. On the

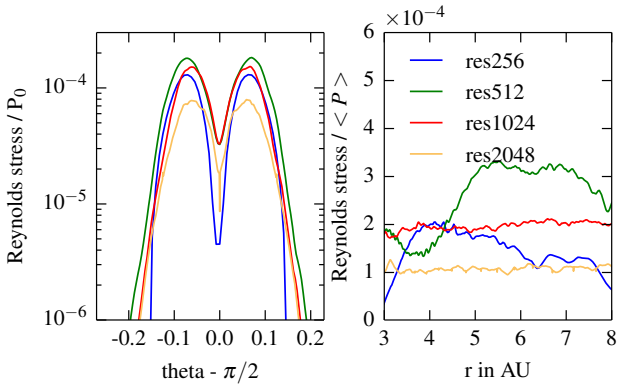

Fig. 6. Radial and vertical distribution of the Reynolds stress. *Left*: the Reynolds stress divided by the midplane pressure over the vertical direction. *Right*: reynolds stress divided by the mean pressure over the radius for different resolutions. Both are averaged over 4001 time steps from orbit 1000 to 5000. The model res2048 corresponds to the results shown in Fig. 1.

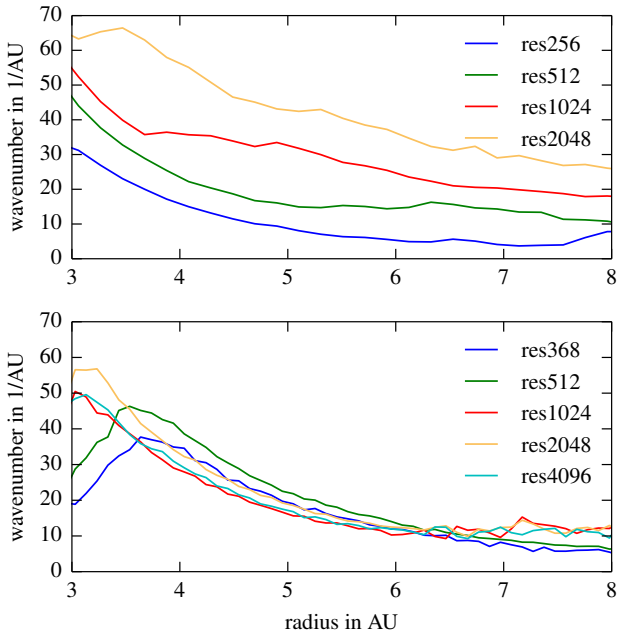

Fig. 7. Mean wavenumber of the instability over the radius for different numerical resolutions in the saturated phase. *Upper panel*: inviscid case with $\nu = 0$, *lower panel*: viscous case with $\nu = 5\times10^{-7}$ (dimensionless).

right we plot the Reynolds stress divided by the pressure, where both pressure and stress have been averaged over the meridional direction.

From this plot it is not clear if the values for α converge to a specific level for higher resolution. Nevertheless, it gives a first impression on the strength of turbulent viscosity caused by this instability being relatively weak with α-values a few times 10^{-4}, which is slightly smaller than the value of 6×10^{-4} found by Nelson et al. (2013).

In Fig. 7 we show the wavelength of the perturbation as a function of radius for different numerical resolutions, where the wavelength has been estimated by measuring the distance between two sucsessive changes of the sign of the vertically averaged vertical momentum after the instability is saturated

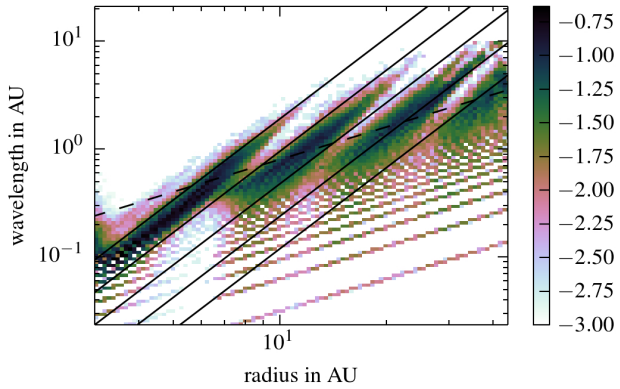

Fig. 8. Histogram: colour coded is the logarithm of the probability for the occurrence of a wavelength at a radius normalised at each radius by the sum of all wavelengths for the specific radius. The black lines are proportional to the radius to the power of 2.5 and the lines are a factor of 2 apart from each other. The dashed line has linear slope. One can see that the instability jumps successively between different modes for the wavelength with corresponding jumps in frequency at the same radius.

(see Fig. 2, third panel, or Fig. 10 along the radius axis, beginning with orbit 1000). This does not, of course, reveal the full spectrum, but at this point we are more interested in the characteristic mean wavelength. We note that the wavelength in the growth phase can be smaller. In all shown resolutions one wavelength is resolved with 15–50 grid cells, while larger radii are better resolved. Despite the variation with radius one notices in Fig. 7 that the wavelength clearly depends on the numerical resolution. One possible cause for this is the lack of physical viscosity. Because the (intrinsic) numerical viscosity of the code decreases with increasing resolution, this may explain the missing convergence, in particular since the growth rates depend of the wavenumbers of the disturbances, see Eq. (12). We repeated the run with an intermediate resolution of 1440×360 with reduced precision by using a first order instead of a second order spatial interpolation. This clearly increased the wavelength (by about 40%) indicating that the problem is caused by the numerical viscosity.

Figure 7 indicates a strong reduction of the wavenumber with radius. To further explore this dependence of the wavelength on the radius, we performed an additional simulation with an extended radial domain from 2 AU to 50 AU. Again, we estimate the wavelength by measuring the distance between two sign changes in the vertical averaged vertical momentum. This time we show all the wavelengths that were detected by this method in Fig. 8, where we show how often a certain wavelength was captured, normalised to the specific radius where it was measured. An interesting behaviour can be observed. While the global radial wavelength does indeed depend linearly on the radius, locally it clearly deviates from this dependence and instead depends on the radius to the power of 2.5. This can also be seen in the simulation with smaller domain, but there it cannot be clearly distinguished from the interaction with the boundary.

This supplies us with an explanation for the resolution dependence of the instability. Since the modes cannot become arbitrarily small (because of the finite grid) or large (because of the limited vertical scale hight) there will be jumps between different modes. The viscosity and the Kelvin-Helmholtz instability, which can be observed in the simulations with high resolution, are the candidates for a physical cause for this cut off at small wavelengths.

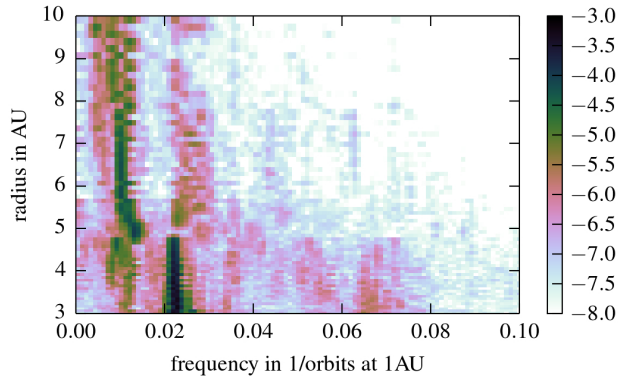

Fig. 9. Fourier power spectrum of the temporal evolution of the instability after saturation (see Fig. 10). Analysed is the averaged meridional momentum of the simulation without viscosity and resolution 1024 × 256. Colour coded is the logarithm of amplitude of the frequency.

Because of the radius dependence of the wavenumber a spatial Fourier transform is not applicable. Additionally, as we show below, the wavelength in radial direction is not constant in time and phase jumps also can occur. However, to obtain more insight into the dynamics of the system, we show in Fig. 9 the results of a Fourier analysis in time of the vertical momentum of the simulation with resolution of 1024×256 (Fig. 10, along the time axis). To reduce the problems that phase jumps pose for the analysis (see below), we step through the data with a Hanning window over 1000 orbits and then average over those 5% of the resulting spectra that give the highest amplitude. We can see a dominant frequency at $0.022\Omega_K$ at the inner region; this frequency is halved at the outer region beginning at about 5 AU. These jumps in the frequency domain coincide with the jumps in wavenumber. When the wavenumber jumps up, the frequency falls down, indicating an inverse relationship. On each branch the frequency is constant, while the wavenumber varies as $\propto r^{-2.5}$. We can understand this relationship starting from Eq. (12) from which one obtains for stable inertial oscillations (see Eq. (36) in Nelson et al. 2013)

$$\sigma^2 \sim -\Omega^2 \frac{k_Z^2}{k_R^2}. \tag{16}$$

The vertical scale is given by the local disc's scale height $H \sim r$ and hence $k_Z \sim r^{-1}$. In the quasistationary phase, we observed $k_R \sim r^{-2.5}$ (see Fig. 8), leading to an oscillation frequency independent of the radius, which we also observed (see Fig. 9).

To obtain further insight into the spatio-temporal behaviour of the flow dynamics in Fig. 10 we show the vertically averaged momentum in the vertical direction as a function of space and time. In this global overview we observe waves that appear to travel slowly from larger to smaller radii. As noticed already in the Fourier analysis in Fig. 9, there is a transition between 4–5 AU with a change in wavelength of the perturbations and occasional phase jumps. Coupled to this is a change in the typical inward speed of the waves. They move more slowly when farther away from the star. As inferred roughly from Fig. 10, the wave speed at $r = 6$ AU is about 0.5 AU per 250 orbits, while at 4 AU it is about 1 AU. However, there is some dependence of this speed on time and space.

Near the outer boundary we sometimes see a region with standing waves, indicating that the radial domain should not be too small. This region is mostly only a few wavelengths in size (less then 1 AU), but can sometimes also reach a few AU into the domain. Reflections with the outer boundary play a role here as well, as can be seen in Fig. 10 for example at $t \approx 500$ or 3600. We note that in contrast to our treatment at the inner radial boundary, we did not apply a damping region at the outer boundary.

To check if the viscosity is important for the wavelength, we add a small viscosity of $\nu = 5 \times 10^{-7}$. As expected, this leads to a wavenumber that is independent of the resolution, as shown in the bottom panel of Fig. 7. The wavelength is of the order of 0.2 AU at a radius of 4 AU after the instability is saturated.

With the wavelength fixed, the Reynolds stress also shows no strong dependence on the resolution as can be seen in Fig. 11 top panel. The inner region is strongly suppressed because we also increased the damping from 2 AU to 3 AU. With that we conclude that a small viscosity is necessary in order to introduce a physical lengthscale for the smallest unstable wavelength. To further explore the role of viscosity we repeat the simulation for different viscosities. This is done with a resolution of 1440 × 360. The growth rate is then calculated by fitting a linear function to the logarithm of the kinetic energy, which was at each point averaged over 100 grid cells. The results in the lower panel of Fig. 11 indicate that for the two lowest viscosities (10^{-8} and 10^{-7}) the stresses are given by the numerical viscosity. For the intermediate case (10^{-7}) the stresses are larger while for very large values the effect of the increased damping near the inner boundary influences the results.

5. Discs with radiation transport

The isothermal discs discussed above do not capture the full physics, and most importantly the transport of energy is missing. In this section we include radiative transport and the heating/cooling interaction of the gas with the radiation. In the first set of models we start from the isothermal models as described above and switch on the radiation according to Eqs. (3) and (4); in a second series of models (in Sect. 6) we include irradiation from the central star.

For the simulations with radiative transport we use a resolution of 1024 × 256 and the same spatial extent and initial conditions as in the isothermal case. In Fig. 12 we show the midplane temperature averaged from 4–5 AU and the meridional kinetic energy when radiation is included, for two different values of the disc density ρ_0. In both cases the kinetic energy initially has larger amplitudes than in the previous isothermal simulations because now the disc is no longer in hydrostatic equilibrium initially, and small motions in the meridional plane set in (lower panel in Fig. 12). For the same disc density as before, $\rho_0 = 10^{-10}$, the disc cools off quickly as soon as the instability begins to be active, at around $t = 10$. The reason lies in the efficient radiative cooling in this case, in particular near the surface layers where the optical depth is small and the instability most active. Hence, any turbulent heating will be radiated away quickly.

We repeated the simulation with a higher density, $\rho_0 = 10^{-9}$ at 1 AU, to increase the optical thickness. Now the disc does not cool efficiently enough, and the instability begins to set in between $t = 10$ and $t = 20$ orbits, very similar to the isothermal models, but then radiative cooling eventually leads again to a cooling of the disc and the instability dies out. From these results it is clear that the instability does not produce enough heat and cannot survive without an external source of heat, for the typical opacities and densities expected in protoplanetary discs. This potential problem was pointed out already by Nelson et al. (2013).

A&A 572, A77 (2014)

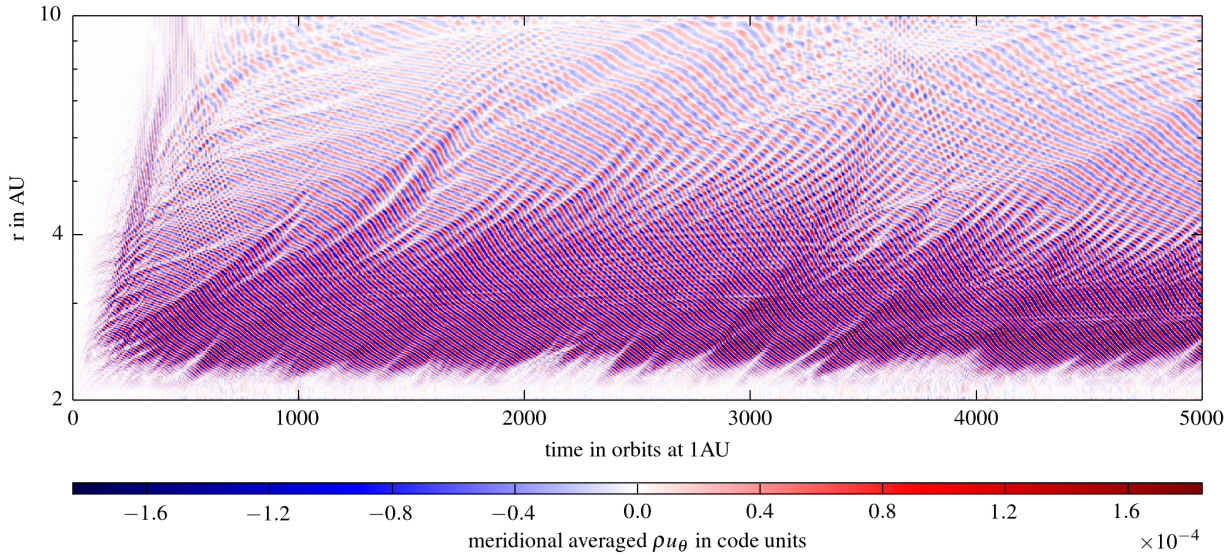

Fig. 10. Large scale time development of the instability. Shown is the vertically averaged momentum in the meridional direction for the inviscid isothermal simulation with a resolution of 1024×256 (red curve in top panel of Fig. 7).

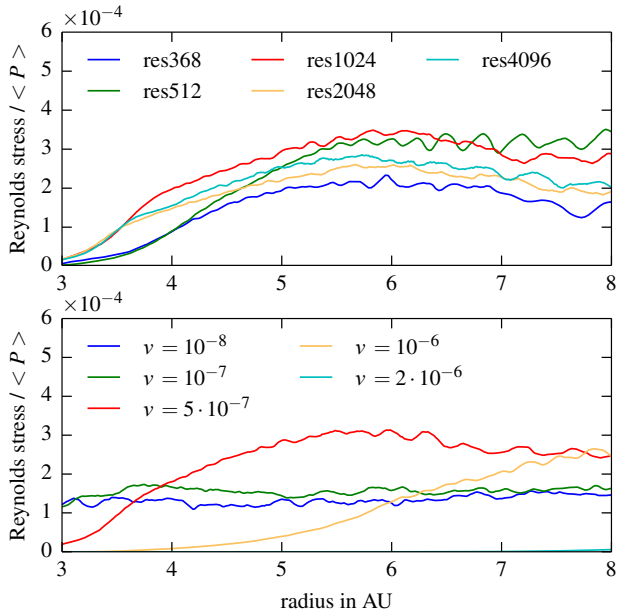

Fig. 11. Vertically averaged Reynolds stress divided by the vertically averaged pressure in the saturated phase. *Upper panel*: for a viscosity of 5×10^{-7} at different numerical resolutions. *Lower panel*: fixed resolution of 1440×360 and different viscosities. Both are averaged from orbits 1000 to 3000.

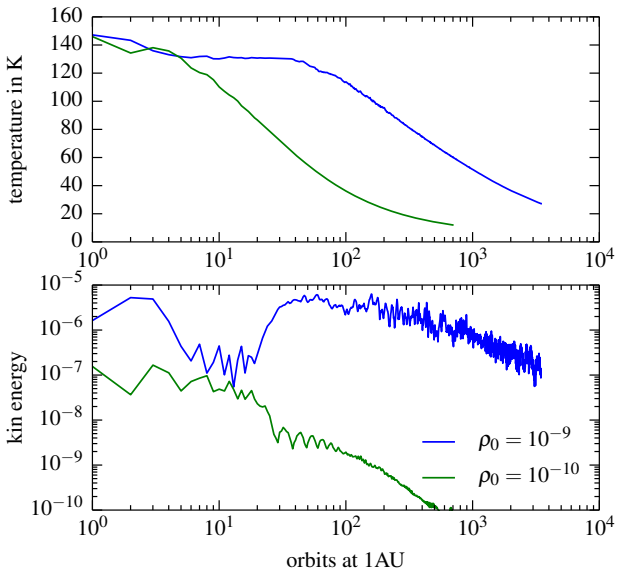

Fig. 12. Discs with radiation transport for two different densities, ρ_0. *Upper panel*: the midplane temperature at 4–5 AU as a function of time. *Lower panel*: kinetic energy in the meridional flow in the discs.

6. Irradiated disc

Here, we extend our models and include irradiation from the central star as an external heat source. Of course there are also other sources possible, for example, the inner region of the disc where the MRI is still active could be important.

6.1. Method of irradiation

We use a simple model for the external heating and consider vertical irradiation from above and below the disc, where the energy flux, $\boldsymbol{F}^{\rm irr}$, depends on radius. This procedure avoids the problem of finding a self-consistent solution for the flaring of the disc, as done for an irradiated and internally heated disc by Bitsch et al. (2013).

To obtain a first approximation for the flux in the meridional direction we assume that the angle of incidence of the flux is approximately $R_\odot/r$, where $R_\odot$ is the star's radius. This applies to an infinitely flat disc as well as to the upper and lower surfaces our computational grid in spherical polar coordinates because all three represent planes that cross the centre of the central star. We obtain for the meridional component of the flux

$$F_\theta^{\rm irr} = F_r \frac{R_\odot}{R}, \tag{17}$$

where $F_r = F_\odot (R_\odot/r)^2$ is the radial flux from the star at a distance r. Applying this impinging vertical irradiation to the

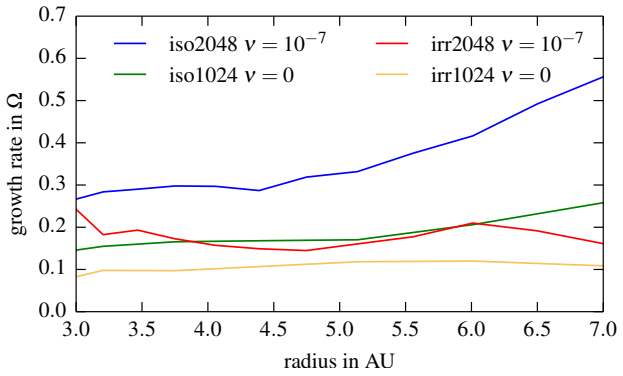

Fig. 13. Growth rates for models with radiation transport and irradiation (irr) and isothermal models (iso) that have the same mean temperature, for comparison. For each radius the kinetic energy was smoothed over a range of 10% of its radius before fitting it to an exponential growth.

disc leads to a radial temperature profile exponent in the disc of $q = -0.55$, in good agreement with the models of Chiang & Goldreich (1997). Our procedure does not allow for self-shadowing effects (Bitsch et al. 2013) but should give a physically realistic estimate of the expected temperatures in the disc.

To simplify the calculations and obtain a first order estimate of the effect, we use for the irradiation opacity the Rosseland opacity of Bell & Lin (1994). Hence, in the simulations we use the same opacity for the irradiation, Rosseland and Planck opacity (Bitsch et al. 2013). Numerically, we perform a ray-tracing method to calculate the energy deposited in each cell of the computational grid (Kolb et al. 2013).

6.2. Growth rate

To measure the growth rates of the instability for discs with radiation transport and irradiation we ran models with zero viscosity and a higher resolution case with $\nu = 10^{-7}$. To be able to compare the growth rates with the previous isothermal cases, we performed additional isothermal simulations using the temperature profile from the simulations with radiation transport and irradiation.

The growth rates for the instability in combination with radiation transport are difficult to capture because the simulation cannot be started in hydrostatic equilibrium because the equilibrium vertical profile is unknown. We use strong damping for the first ten orbits to remove the disturbance caused by the transition to the new density and temperature profile.

The results are shown in Fig. 13. We note that this time the growth rates should depend on radius because the growth depends on H/R which is not constant in the radiative cases. From Fig. 13 it is clear that the growth rates for the isothermal models are now lower than in the cases presented above, first because the temperature is lower and second because the radial profile is flatter as before, and both are important for growth. For the irradiated models the growth is again lower, with 0.1−0.2 per local orbit around half the value for the isothermal case. In Fig. 14 we show the evolution of the kinetic energy for the irradiated and corresponding isothermal model. For the inviscid case the final saturation levels agree very well with each other, while for the viscous disc with $\nu = 10^{-7}$ the instability is weaker in the inner regions of the disc (see below).

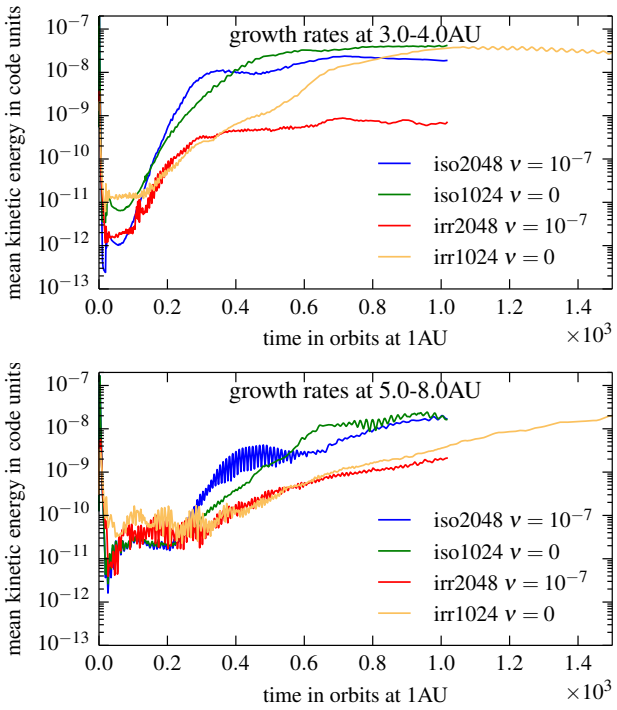

Fig. 14. Growth of the kinetic energy in the 2D plane with radiation transport and isothermal for comparison.

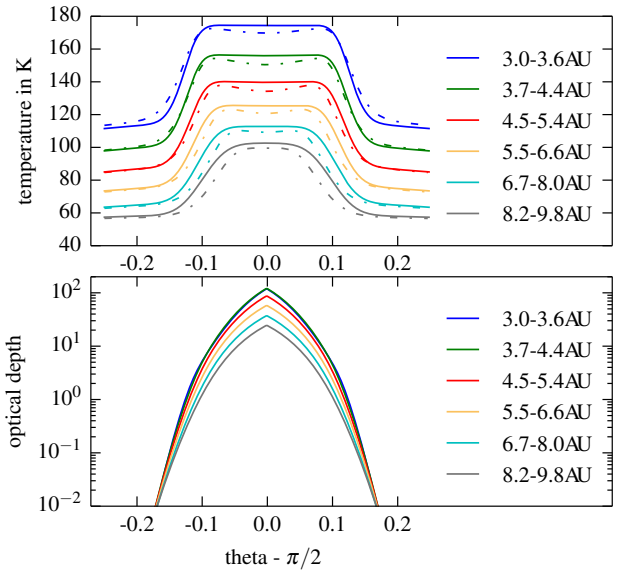

Fig. 15. *Upper panel*: temperature profile for an irradiated disc in the saturated phase without viscosity and a resolution of 1024 × 256. The dotted line is a run without hydrodynamics, only solving for the radiation energy. *Lower panel*: vertically integrated optical depth.

6.3. Quasistationary phase

In the top panel of Fig. 15 we show the vertical temperature distribution for the saturated state at different radii in the disc for the model without viscosity at a resolution of 1024 × 256. The other models look very similar. In the bulk part of the disc the profile is quite flat with a slight drop towards the midplane. A lower central temperature is to be expected for irradiated dics,

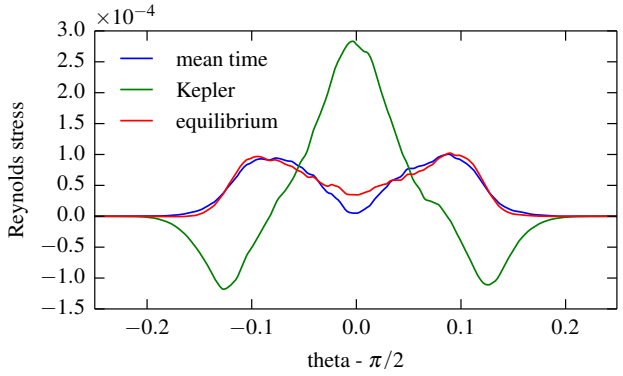

Fig. 16. Irradiated run. The Reynolds stress was averaged over 41 time steps, from orbit 1000 to 5000 each step 100 orbits apart, calculated with different averaging methods. For "mean time" the mean u_ϕ was calculated through averaging over 40 time steps. For "*Kepler*" the velocity was calculated by subtracting the *Kepler* velocity and for the last one u_ϕ is calculated analytically by using the equilibrium Eq. (11). Spatial averages are taken from 4 AU to 10 AU.

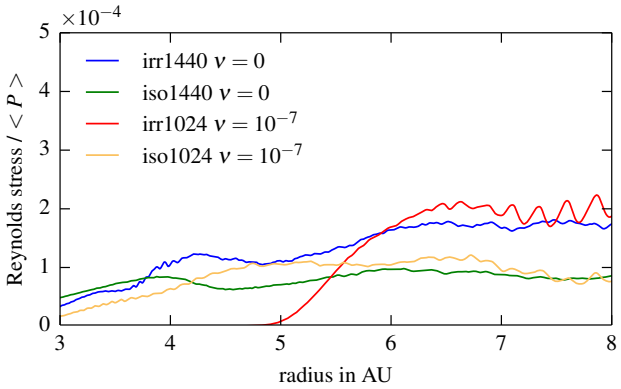

Fig. 17. Comparison of the Reynolds stress divided by the mean pressure, averaged over 2000 orbits, beginning with orbit 2000; "irr" stands for the irradiated disc, "iso" for the isothermal disc with analogous initial conditions.

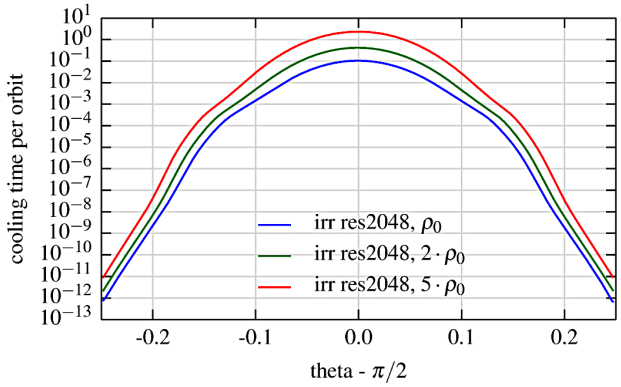

Fig. 18. Radiative diffusion time per Orbit at 4 AU for a lengthscale of 0.1 AU.

detailed radiative transfer models indicate an even larger temperature drop towards the midplane (Dullemond et al. 2002). In the upper layers the temperature falls off because the disc is optically thin and the energy can freely leave the system. This drop of the temperatures towards the surface despite the irradiation is a result of the identical irradiation and Rosseland opacity. If more radiation is allowed to be absorbed in the disc by increasing the irradiation opacity then one can obtain hotter surface layers. For a ten times larger value we find a hot corona similar to Flock et al. (2013) and a cooler midplane. First results seem to indicate a reduction in the Reynolds stress in this case, probably caused by the lower temperature in the bulk of the disc. At this point we leave the details to subsequent studies. The dotted line in Fig. 15 shows the profile for a simulation where we only solve for the radiation energy and disable the hydrodynamic solver. We can infer from this that the flat profile is a result of the combination of turbulent heating and vertical motion. A test simulation with a passive tracer added in the midplane of the disc in the saturated state showed rapid spreading over the whole vertical extent of the disc.

The vertically integrated optical depth is shown in the lower panel, starting from very small values at the disc surfaces it reaches 30–100 at the different radii. The nearly constant vertical temperature within the disc motivates us to use the equilibrium azimuthal velocity for the corresponding isothermal model of the steady state to calculate the Reynolds stress. In Fig. 16 we can see that it is still a good approximation. We note that this time the comparison is done with a 2D-simulation. Additionally shown is the Reynolds stress calculated with the *Kepler* velocity instead of the equilibrium velocity.

While the growth rates are weaker than in the isothermal case, the kinetic energy in the meridional plane for stable saturated phase in Fig. 17 reaches the same level with radiation transport. The values for α are again between 0.5×10^{-4} and 2×10^{-4}, depending on the wavelength and thus viscosity, but independent of radiation transport.

The strength of the instability measured in terms of the value of the viscosity under which it still survives is, of course, different. Here, in the irradiated case, even a low viscosity of 10^{-7} suppresses the instability in the inner regions of the disc. This is not only a result of the radiation transport, but also of the flat temperature profile. The details will depend on the source of the heating and the opacity, but nevertheless the stability will be weaker than in the purely isothermal case.

6.4. Discussion

As we have shown in the previous sections for an irradiated disc there is the possiblity of generating an effective turbulence through the VSI. As pointed out in Nelson et al. (2013) the instability can only be sustained if the diffusion (local relaxation) time is a fraction of the local orbital period. To investigate how this condition is fulfilled in our simulations we analyse the timescale for radiative diffusion for the equilibrium irradiated disc models. In units of the local orbital period this is given by

$$t_{\rm diff} = \Delta x^2 \frac{c_{\rm P}\rho^2\kappa_{\rm R}}{4\lambda acT^3}\cdot\frac{\Omega}{2\pi}, \tag{18}$$

where Δx is the characteristic wavelength of the perturbation. In our case the radial diffusion is relevant (Nelson et al. 2013) and we choose here $\Delta x = 0.05r$, which is a typical radial wavelength at $r = 3$ AU. Using Eq. (18) and the results from the simulation we calculate for the optical thin region a very small cooling time per orbit of $t_{\rm diff} = 10^{-10}$ as expected. For the optically thick region we obtain $t_{\rm diff} = 0.11$ for our standard density, which is indeed a small fraction of the orbital period as required for the instability to operate, see Fig. 18. The cooling time in the vertical direction is longer, about a few orbital periods as implied by

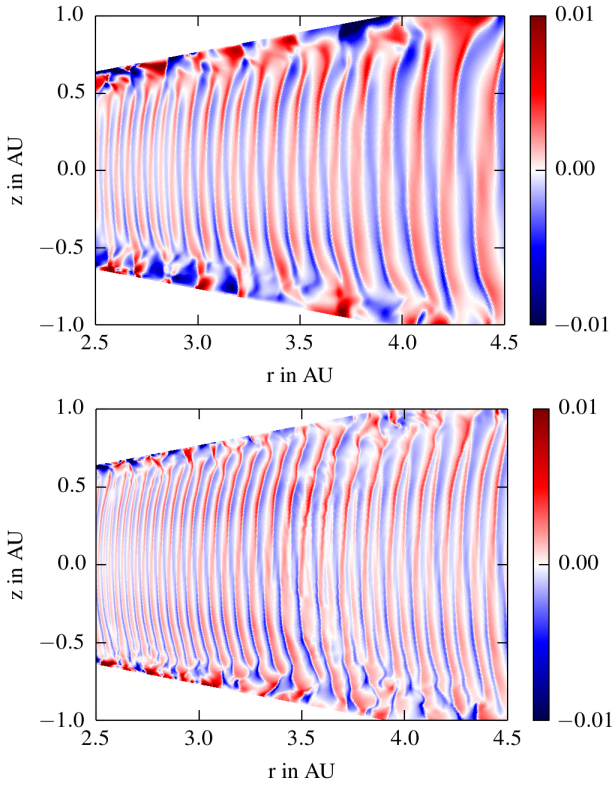

Fig. 19. Velocity in the meridional direction, u_θ, in units of local *Kepler* velocity for an irradiated run without viscosity at resolution 1024×256 (*top*) and with resolution 2048×512 (*bottom*). Compare with Fig. 2 which has a spatial resolution of 2048×512.

the vertical optical depth (see Fig. 15), but this will keep the disc nearly isothermal, again as required for instability.

In Fig. 19 we illustrate that the instability still resembles closely the locally isothermal case except that the small scale perturbations are missing, even in the optically thin region, where we have very short cooling times. For comparison, Nelson et al. (2013) found that the instability was completely suppressed with relaxation times of $t_{\rm relax} = 0.1$, which is the timescale for the flow to relax to the initial isothermal profile. We take this as an indication that physically, radiative diffusion plus irradiation behaves in a different way from a simple model of temperature relaxation as used in Nelson et al. (2013).

As seen in Fig. 15 an increase in the density leads to higher optical depths and longer diffusion times, and consequently to a weaker instability. While doubling the density in a simulation with resolution 2048×512 has no clear influence on the kinetic energy and the cooling times in the optical thin regions, the Reynolds stress was clearly weaker by a factor of around 1.5 in the simulation with doubled density (the model in the middle of Fig. 18). In addition the wavelength of the perturbations is decreased.

A further increase in the density leads also to a strong decrease in the kinetic energy, with again a smaller wavelength. This raises the question whether the simulation with resolution of 2048×512 is sufficiently resolved. These results indicate that in very massive discs with long diffusion times (vertical and radial) the disc will behave more adiabatically, and the instability will be quenched. The minimum solar mass nebula at 5 AU corresponds approximately to our model with 2 ρ_0 and the instability might just be operative.

7. Summary and conclusions

We have studied the vertical shear instability as a source of turbulence in protoplanetary discs. For that purpose we have performed numerical simulations solving the equations of hydrodynamics for a grid section in spherical polar coordinates. To study the global behaviour of the instability we have used a large radial extension of the grid ranging from 2 AU to 10 AU.

In a first set of simulations we show that the instability occurs for locally isothermal discs where the radial temperature gradient is a given function of radius. Our results on the growth rates for the instability are in good agreement with the theoretical estimates by Urpin & Brandenburg (1998) and Urpin (2003), and we find two basic growth regimes for the asymmetric and antisymmetric modes as seen by Nelson et al. (2013). After 20 to 30 local orbits the instability saturates and is dominated by the vertical motions, which cover the whole vertical extent of the disc.

Interestingly, we find that the local radial wavelength of the perturbations scales approximately with $\lambda \propto r^{2.5}$ in the saturated state with a constant frequency. However, on a global scale several jumps occur where the wavelengths are halved, such that the global scaling follows $\bar{\lambda} \propto r$ with $\bar{\lambda}/r = 0.03$. We suspect that the instability has the tendency to generate global modes that show the observed wavelength behaviour according to Eq. (16). Because of the radial stratification of the disc, jumps have to occur at some locations.

The waves approximately keep their shape and travel slowly inwards. The two- and three- dimensional simulations yield essentially the same results concerning the growth rates and saturation levels of the instability because of its axisymmetric property. The motions give rise to a finite level of turbulence and we calculate the associated efficiency, measured in terms of α. We first show that, caused by the two-dimensionality, α can be measured directly from the two-dimensional simulations using the proper equilibrium state of the disc. We find that the angular momentum associated with the turbulence is positive and reaches α-values of a few 10^{-4}. For the isothermal simulations we find that at higher numerical resolution α becomes smaller, but viscous simulations indicate a saturation at a level of about $\alpha = 10^{-4}$ even for very small underlying viscosities that are equivalent to $\alpha < 10^{-6}$.

Adding radiative transport leads to a cooling from the disc surfaces and the instability dies out subsequently. We then constructed models where the disc is irradiated from above and below which leads to a nearly constant vertical temperature profile within the disc. This again leads to a turbulent saturated state with a similar transport efficiency to the purely isothermal simulations, or possibly slightly higher (see Fig. 17).

In summary, our simulations indicate that the VSI can indeed generate turbulence in discs albeit at a relatively low level of about a few times 10^{-4}. This implies that even in (magnetically) dead zones the effective viscosity in discs will never fall below this level. Our results indicate that in fully 3D simulations the transport may be marginally larger, but further simulations will have to be performed to clarify this point.

Acknowledgements. Moritz Stoll received financial support from the Landesgraduiertenförderung of the state of Baden-Württemberg. Wilhelm Kley acknowledges the support of the German Research Foundation (DFG) through grant KL 650/8-2 within the Collaborative Research Group FOR 759: The formation of Planets: The Critical First Growth Phase. Some simulations were performed on the bwGRiD cluster in Tübingen, which is funded by the Ministry for Education and Research of Germany and the Ministry for Science, Research and Arts of the state Baden-Württemberg, and the cluster of the Forschergruppe FOR 759 "The Formation of Planets: The Critical First Growth Phase" funded by the DFG.

References

Arlt, R., & Urpin, V. 2004, A&A, 426, 755
Armitage, P. J. 2011, ARA&A, 49, 195
Balbus, S. A. 2003, ARA&A, 41, 555
Bell, K. R., & Lin, D. N. C. 1994, ApJ, 427, 987
Bitsch, B., Crida, A., Morbidelli, A., Kley, W., & Dobbs-Dixon, I. 2013, A&A, 549, A124
Chiang, E. I., & Goldreich, P. 1997, ApJ, 490, 368
de Val-Borro, M., Edgar, R. G., Artymowicz, P., et al. 2006, MNRAS, 370, 529
Dullemond, C. P., van Zadelhoff, G. J., & Natta, A. 2002, A&A, 389, 464
Flaig, M., Ruoff, P., Kley, W., & Kissmann, R. 2012, MNRAS, 420, 2419
Flock, M., Dzyurkevich, N., Klahr, H., Turner, N. J., & Henning, T. 2011, ApJ, 735, 122
Flock, M., Fromang, S., González, M., & Commerçon, B. 2013, A&A, 560, A43
Fricke, K. 1968, Z. Astrophys., 68, 317
Fromang, S., & Nelson, R. P. 2006, A&A, 457, 343
Goldreich, P., & Schubert, G. 1967, ApJ, 150, 571
Klahr, H., & Hubbard, A. 2014, ApJ, 788, 21
Klahr, H. H., & Bodenheimer, P. 2003, ApJ, 582, 869
Kley, W., Papaloizou, J. C. B., & Lin, D. N. C. 1993, ApJ, 416, 679
Kolb, S. M., Stute, M., Kley, W., & Mignone, A. 2013, A&A, 559, A80
Levermore, C. D., & Pomraning, G. C. 1981, ApJ, 248, 321
Lin, D. N. C., & Pringle, J. E. 1987, MNRAS, 225, 607
Lyra, W. 2014, ApJ, 789, 77
Mignone, A., Bodo, G., Massaglia, S., et al. 2007, ApJS, 170, 228
Minerbo, G. N. 1978, J. Quant. Spectr. Rad. Transf., 20, 541
Nelson, R. P., Gressel, O., & Umurhan, O. M. 2013, MNRAS, 435, 2610
Pringle, J. E. 1981, ARA&A, 19, 137
Ruden, S. P., Papaloizou, J. C. B., & Lin, D. N. C. 1988, ApJ, 329, 739
Shakura, N., & Sunyaev, R. 1973, A&A, 24, 337
Turner, N. J., Fromang, S., Gammie, C., et al. 2014, in Protostars and Planets VI, eds. H. Beuther et al. (University of Arizona Press)
Urpin, V. 2003, A&A, 404, 397
Urpin, V., & Brandenburg, A. 1998, MNRAS, 294, 399

A&A 594, A57 (2016)
DOI: 10.1051/0004-6361/201527716

Astronomy & Astrophysics

Particle dynamics in discs with turbulence generated by the vertical shear instability

Moritz H. R. Stoll and Wilhelm Kley

Institut für Astronomie und Astrophysik, Universität Tübingen, Auf der Morgenstelle 10, 72076 Tübingen, Germany
e-mail: [moritz.stoll;wilhelm.kley]@uni-tuebingen.de

Received 9 November 2015 / Accepted 7 July 2016

ABSTRACT

Context. Among the candidates for generating turbulence in accretion discs in situations with low intrinsic ionization, the vertical shear instability (VSI) has become an interesting candidate, since it relies purely on a vertical gradient in the angular velocity. Existing numerical simulations have shown that α-values a few times 10^{-4} can be generated.
Aims. The particle growth in the early planet formation phase is determined by the dynamics of embedded dust particles. Here, we address, in particular, the efficiency of VSI-turbulence in concentrating particles to generate overdensities and low collision velocities.
Methods. We perform three-dimensional (3D) numerical hydrodynamical simulations of accretion discs around young stars that include radiative transport and irradiation from the central star. The motion of embedded particles within a size range of a fraction of mm up to several m is followed using standard drag formula.
Results. We confirm that, under realistic conditions, the VSI is able to generate turbulence in full 3D protoplanetary discs. The irradiated disc shows turbulence within 10 to 60 au. The mean radial motion of the gas is such that it is directed inward near the midplane and outward in the surface layers. We find that large particles drift inward with the expected speed, while small particles can experience phases of outward drift. Additionally, the particles show bunching behaviour with overdensities reaching five times the average value, which is strongest for dimensionless stopping times around unity.
Conclusions. Particles in a VSI-turbulent discs are concentrated in large-scale turbulent eddies and show low relative speeds that allow for growing collisions. The reached overdensities will also enable the onset of streaming instabilities, further enhancing particle growth. The outward drift for small particles at higher disk elevations enable the transport of processed high temperature material in the solar system to greater distances.

Key words. instabilities – hydrodynamics – accretion, accretion disks – radiative transfer

1. Introduction

To drive mass flow in accretion discs, an anomalous source of angular momentum is required (Frank et al. 2002). A strong candidate is the magneto-rotational instability (MRI), which gives rise to turbulent magnetohydrodynamical (MHD) flows that create an outward angular momentum transport disc (Balbus & Hawley 1998). Driven by magnetic fields, the MRI requires a sufficient level of ionization to sustain a turbulent state within the disc. However, protoplanetary discs only have a very low temperature regime and insufficient thermal ionization. Even considering external sources of ionization, there appears to be a region of insufficient ionization level such that the MRI cannot operate, as shown by resistive MHD simulations, including radiative transport (Flaig et al. 2012). Hence, there may exist a dead zone somewhere between 2−20 au (Armitage 2011), where the MRI can only produce very weak turbulence. Recent simulations that also included, in addition to Ohmic resistivity, ambipolar diffusion have even shown no signs of turbulence at all in this region (Gressel et al. 2015). The Hall effect creates strong winds on the surface of the disc and may even reintroduce angular momentum transport in the dead zone, but this depends on the sign of the magnetic field (Bai 2014, 2015). Thus another origin of instability inside the dead zones is warranted to drive accretion in protoplanetary discs.

As an alternative to the MRI, different examples of purely hydrodynamic instabilities in discs have been suggested, such as gravitational instability (Lin & Pringle 1987), convective instability (Ruden et al. 1988), or baroclinic instability (Klahr & Bodenheimer 2003), but they do not operate under general conditions. One possibility, that has recently attracted more attention is the vertical shear instability (VSI) suggested for accretion discs by Urpin (2003). The mechanism was first examined in relation to differential rotating stars (Goldreich & Schubert 1967; Fricke 1968), and it is also known as Goldreich-Schubert-Fricke instability. In the context of discs, first simulations have been carried out by Arlt & Urpin (2004). While there is a much stronger radial gradient in the angular velocity, Ω, to feed instabilities, most instabilities cannot overcome the stabilising effect of rotation. In the context of the VSI, it is the vertical shear in Ω, created by a radial temperature gradient, that allows the disc to become unstable. The numerical work of Nelson et al. (2013) shows that a small turbulent α-value in the range of a few 10^{-4} was possible for isothermal discs. For non-isothermal discs, Nelson et al. (2013) point out that radiative cooling (diffusion) and viscosity reduce the instability, and they developed a theoretical model describing

A&A 594, A57 (2016)

the initial vertical elongated modes that destabilise the disc. In simulations that included full radiative transport, Stoll & Kley (2014) showed that, for situations typical in protoplanetary discs, a sustained VSI was possible providing an $\alpha \sim 10^{-4}$. They found the development of a global wave pattern within the disc whose wavelength was determined partly by viscous effects. Later, Barker & Latter (2015) analysed the VSI through linear analyses of locally isothermal discs and support the modal behaviour seen in the non-linear simulations by Nelson et al. (2013) and Stoll & Kley (2014). They also stress the importance of viscosity to set the smallest length scale.

Recently, Lin & Youdin (2015) shed light on the cooling requirements of the VSI that arise because the VSI has to compete with the stabilising vertical buoyancy. Their theoretical models predict activity in regions with long cooling time only for very large wavenumbers. Thus the VSI is limited by the cooling time on large scales and by viscosity on small scales. With this in mind they predict VSI activity for typical disc models only between 5 and 100 au.

We test this idea by expanding our previous work (Stoll & Kley 2014), where we used a self-consistent radiation transport module and a vertically irradiated disc in the simulations. Here, we treat the irradiation in a more realistic way as originating from the central star, and show that, even under this condition, the VSI can be sustained.

The turbulence in protoplanetary discs is also critical for the initial dust evolution that leads eventually to planet formation. Numerical simulations performed by Johansen & Klahr (2005) and Fromang & Nelson (2005) showed that particles can be caught in the local pressure maxima generated by the MRI turbulence. This clustering of dust particles can then trigger a streaming instability (Youdin & Goodman 2005) that will lead to further clustering and subsequently to the formation of *km*-planetesimals. In the context of the VSI the large-scale velocity patterns of the corrugation mode promises interesting behaviour for embedded dust grains and larger particles. To investigate the impact of the VSI modes on the dust particles we add particles into our disc model and follow their dynamical evolution.

The paper is organized as follows. In Sect. 2 we present our numerical and physical setup. We present a detailed analysis of an isothermal disc model in Sect. 3, and we discuss in Sect. 4 the results for the particle evolution is this model. In Sect. 5 we describe the results of a viscous model. The simulations with radiation transport and stellar irradiation are presented in Sect. 6 and in Sect. 7 we conclude.

2. The model setup

We use the same equations and physical disc setup, as described in detail in our first paper (Stoll & Kley 2014) and give here only a very brief outline. In summary, for the integration of the hydrodynamical equations we use PLUTO, a publicly available code, based on a Godunov scheme for viscous hydrodynamical flow (Mignone et al. 2007), extended by flux-limited diffusion module for radiation transport and a ray-tracing method for stellar irradiation (Kolb et al. 2013). Having used a two-dimensional, axisymmetric disc setup in our previous work, we now extend the computational domain in the azimuthal direction to three dimensions (3D) and add particles to the flow. For this purpose we added a particle solver based on the method by Bai & Stone (2010), that we describe in the next section.

2.1. Particle Solver

We use Lagrangian particles with drag and gravitation:

$$\frac{\mathrm{d}\boldsymbol{v}_\mathrm{p}}{\mathrm{d}t} = \boldsymbol{a} = \boldsymbol{f} + \frac{\boldsymbol{v}_\mathrm{p} - \boldsymbol{u}}{t_\mathrm{s}}, \tag{1}$$

where $\boldsymbol{f}$ is an acceleration due to an external force, here the gravitation of the star. $\boldsymbol{v}_\mathrm{p}$ and $\boldsymbol{u}$ are the particle and gas velocity and t_s is the stopping time.

We treat all particles as if they were in the Epstein regime, where the mean free path of the gas molecules is typically greater than the particle cross section (Epstein 1924). The stopping time is then

$$t_\mathrm{s} = \frac{r_\mathrm{p}\rho_\mathrm{p}}{\rho_\mathrm{g}\sqrt{8/\pi}c_\mathrm{s}}, \tag{2}$$

where r_p is particle radius, ρ_p the particle bulk density, ρ_g the gas density, and c_s is the sound speed. In addition we use $\tau_\mathrm{s} = t_\mathrm{s}\Omega_\mathrm{K}$ for the dimensionless stopping time.

To solve the equation of motion of the particles (1) we follow Bai & Stone (2010). If the stopping time is longer than the time step, Δt, of the simulation, we solve the semi-implicit equations

$$\begin{aligned}
\boldsymbol{x}' &= \boldsymbol{x}^{(n)} + \frac{\Delta t}{2}\boldsymbol{v}_\mathrm{p}^{(n)},\\
\boldsymbol{v}_\mathrm{p}^{(n+1)} &= \boldsymbol{v}_\mathrm{p}^{(n)} + \Delta t\boldsymbol{a}\left[(\boldsymbol{v}_\mathrm{p}^{(n)} + \boldsymbol{v}_\mathrm{p}^{(n+1)})/2, \boldsymbol{x}'\right],\\
\boldsymbol{x}^{(n+1)} &= \boldsymbol{x}' + \frac{\Delta t}{2}\boldsymbol{v}_\mathrm{p}^{(n+1)},
\end{aligned}$$

where n denotes the timestep level, and $\boldsymbol{x}'$ an intermediate position of the particle. The particle acceleration, $\boldsymbol{a}$, is a function of the particle velocities, $\boldsymbol{v}_\mathrm{p}$, see Eq. (1).

For stopping times smaller than the time step we solve the following implicit equation, where the velocity update does not depend on the old velocity.

$$\begin{aligned}
\boldsymbol{x}' &= \boldsymbol{x}^{(n)} + \Delta t\boldsymbol{v}_\mathrm{p}^{(n)}\\
\boldsymbol{v}_\mathrm{p}^{(n+1)} &= \boldsymbol{v}_\mathrm{p}^{(n)} + \frac{\Delta t}{2}\left(\boldsymbol{a}\left[\boldsymbol{v}_\mathrm{p}^{(n+1)}, \boldsymbol{x}'\right) + \boldsymbol{a}\left[\boldsymbol{v}_\mathrm{p}^{(n+1)} - \Delta t\boldsymbol{a}\left(\boldsymbol{v}_\mathrm{p}^{(n+1)}, \boldsymbol{x}'\right), \boldsymbol{x}^{(n)}\right)\right)\\
\boldsymbol{x}^{(n+1)} &= \boldsymbol{x}^{(n)} + \frac{\Delta t}{2}\left(\boldsymbol{v}_\mathrm{p}^{(n)} + \boldsymbol{v}_\mathrm{p}^{(n+1)}\right).
\end{aligned}$$

This enables the drag force to damp the particle velocity without unphysical oscillations. The test simulations to verify the correct implementation of the particle solver are described in the appendix in Sect. A.

2.2. Physical setup

In order to study the importance of radiative effects we decided to perform first a sequence of isothermal simulations. We describe briefly the setup of our fiducial disc model, which consists of a 3D isothermal model that simulates one eighth (covering 45° in azimuth) of the disc at a resolution of $1024 \times 256 \times 64$ (in r, θ, ϕ) without viscosity. The full radiative model is described in Sect. 6.

We use the same general disc setup as in Stoll & Kley (2014), where we started with a disc in force equilibrium,

$$\rho(R, Z) = \rho_0 \left(\frac{R}{R_0}\right)^p \exp\left[\frac{GM}{c_\mathrm{s}^2}\left(\frac{1}{\sqrt{R^2 + Z^2}} - \frac{1}{R}\right)\right], \tag{3}$$

with a temperature that is constant on cylinders

$$T(R, Z) = T_0 \left(\frac{R}{R_0}\right)^q. \tag{4}$$

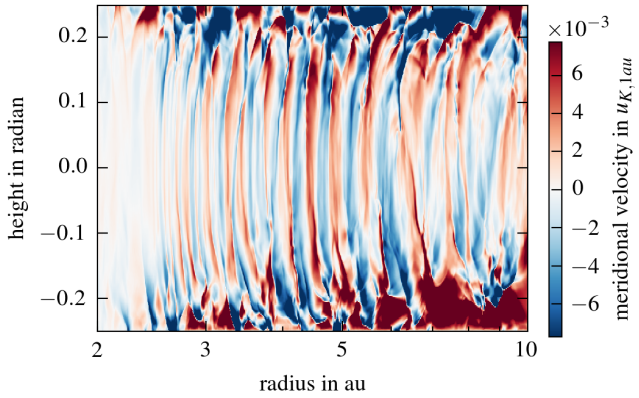

Fig. 1. Velocity in the meridional direction, u_θ, in units of the Kepler velocity for the fiducial isothermal run without viscosity and a resolution of $1024\times256\times64$. Displayed is the quasi-stationary state after 1200 yr.

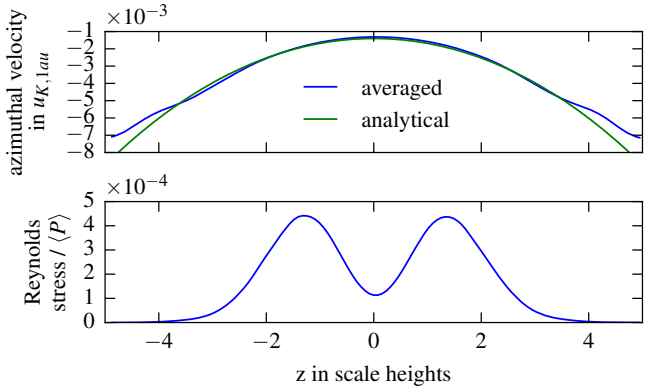

Fig. 2. Averaged azimuthal velocity compared to the analytical velocity (*upper panel*) and $\alpha(z)$ (*lower panel*). For the green (analytical) curve Eq. (9) has been used for the mean value of u_ϕ. The blue curve shows the average from 1000 to 1800 yr over 800 time levels and radially from 4.5 au to 5.5 au.

Here, $c_s = \sqrt{p/\rho}$ denotes the isothermal sound speed, and $H = Rh = c_s/\Omega_K$ is the local pressure scale height of the accretion disc. We use (R,Z,ϕ) for cylindrical coordinates and (r,θ,ϕ) for the spherical coordinates that we use in our simulations. Typical values for the density and temperature exponents are $p = -1.5$ and $q = -1$.

The computational domain of the fiducial model is limited to $r = 2{-}10$ au in the radial and ±5 scale heights in the meridional direction. In contrast to Stoll & Kley (2014), where we only simulated 2D, axisymmetric discs, we use here in the azimuthal direction one eighth of the full disc ($\phi_{max} = \pi/4$) to capture the complete 3D physics of the turbulent disc.

3. The turbulent isothermal disc

Before embedding the particles we first describe the turbulent properties of the VSI for several disc models. We start with the fiducial isothermal and inviscid model for one eighth of the disc and compare this below to models with viscosity and a larger azimuthal domain. In the subsequent section we use the fiducial model for the simulations with particles. Finally, in the last section we also show the results of a radiative, irradiated disc model.

As shown in previous numerical simulations of the VSI the turbulent state is characterized by vertically elongated flow structures as shown in Fig. 1 for the meridional velocity, for more details see Nelson et al. (2013) and Stoll & Kley (2014). To characterize the turbulence of the disc we measure the Reynolds stress that we define here as

$$T_{r,\phi} = \left\langle \rho u_r \delta u_\phi \right\rangle_{\phi,t}, \tag{5}$$

where $\delta u_\phi(r,\theta,\phi) = u_\phi(r,\theta,\phi) - \left\langle u_\phi(r,\theta,\phi)\right\rangle_t$ is the deviation of the angular velocity from the (time averaged) mean azimuthal velocity. We denote averages taken over certain variables by $\langle\,\rangle$ with the appropriate indices. In this definition, $T_{r,\phi}$ is a 2D array in r,θ. The time average, $\left\langle u_\phi \right\rangle_t$, needed in Eq. (5) is in general not known in advance but one can rewrite the Reynolds stress as

$$T_{r,\phi} = \left\langle \rho u_r u_\phi \right\rangle_{\phi,t} - \langle \rho u_r \rangle_{\phi,t} \left\langle u_\phi \right\rangle_{\phi,t}, \tag{6}$$

where the right hand side can in principle be calculated "on the fly" during the simulation. For convenience, we chose to store ϕ-averaged 2D data sets at regular time intervals, and then average these over time to obtain $T_{r,\phi}(r,\theta)$.

From these we calculate the dimensionless α-parameter as a function of radius

$$\alpha(r) = \frac{\left\langle T_{r,\phi} \right\rangle_\theta}{\langle P \rangle_\theta}, \tag{7}$$

where $P = \langle p \rangle_{\phi,t}$ is the azimuthal and time averaged pressure. For the vertically dependent $\alpha(z)$-parameter at a certain radius r_c,

$$\alpha_{r_c}(z) = \frac{\left\langle T_{r,\phi} \right\rangle_r}{\langle P \rangle_r}, \tag{8}$$

we only integrate over a small radial domain around the desired radius, r_c. This averaging procedure to calculate α has to be used for general discs, for example the radiative discs below.

However, for the isothermal simulations, one can approximate the time averaged $\left\langle u_\phi \right\rangle_t$ in the calculation of the Reynolds stress, by the analytically calculated solution for the equilibrium angular velocity (Nelson et al. 2013), that can be obtained from the initial equilibrium disc setup

$$\Omega(R,Z) = \Omega_K \left[(p+q)\left(\frac{H}{R}\right)^2 + (1+q) - \frac{qR}{\sqrt{R^2+Z^2}} \right]^{\frac{1}{2}}, \tag{9}$$

where $\Omega_K = \sqrt{GM_\odot/R^3}$ is the Keplerian angular velocity. In Fig. 2 (upper panel) we can see that this is indeed a valid approximation. Aside from reducing noise in α, since it no longer depends on the time averaged velocity, this has the further advantage of allowing us to directly calculate the α-parameter at each timestep and we thus only need to store 1D arrays, which we then can later average over arbitrary timespans.

In Fig. 3 we compare the radial α-parameter for different isothermal simulations. The averaging was done from 1000 yr to 1800 yr with 800 snapshots taken at regular intervals. Shown are cases with different resolutions, where the labels indicate the radial number of grid cells, and also viscous models. The dimensionless viscosity is given in units of ($u_{K,1\,au} \cdot 1$ au), where $u_{K,1\,au}$ is the Kepler velocity at 1 au. We can see that in contrast to the 2D simulations in Stoll & Kley (2014), where the α-parameter differed by more than 50% when we doubled the resolution,

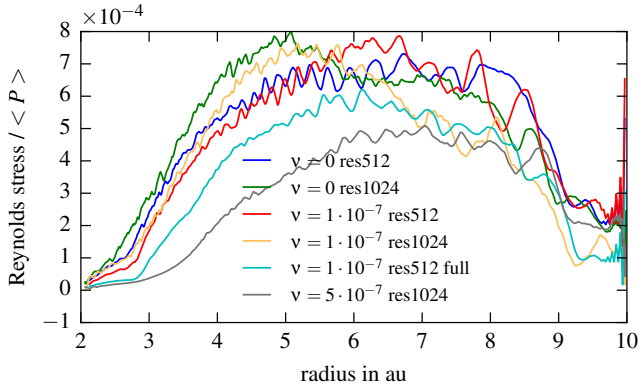

Fig. 3. Comparison of the radial $\alpha(r)$ obtained for different isothermal simulations used in this paper. Values are averaged from 1000 to 1800 yr. All simulations except "full" are for one eighth of a complete disc. The specified resolution refers to the number of radial grid cells in the simulations, where "res1024" denotes the resolution of our fiducial model and "res512" has half the resolution in all spatial directions. In addition to the inviscid fiducial model we ran also simulation with non-zero viscosity, and the labels refer to the dimensionless value of the constant kinematic viscosity coefficient ν.

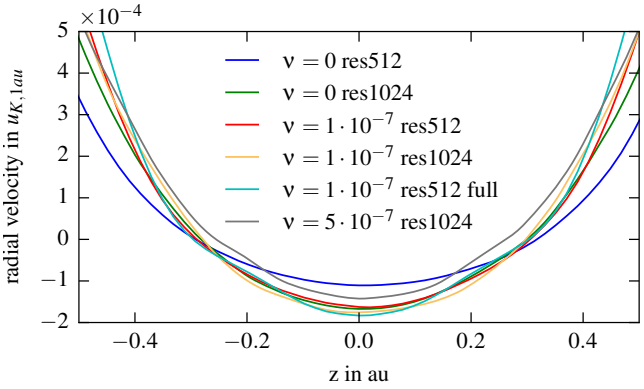

Fig. 4. Radial velocity u_r (in units of the Kepler velocity at 1 au) for the different isothermal simulations evaluated at 5 au. Shown are the same models as in the previous Fig. 3, averaged again from 1000 to 1800 yr. Negative velocities correspond to inflow towards the star.

these 3D simulations show no clear dependence on resolution, with all curves being within 10% of each other at 6 au. We ran a further, shorter simulation without viscosity and double resolution of $2048 \times 512 \times 128$ and could not see a difference in wavelength or Reynolds stress in the early equilibrium phase from 500 to 800 yr. Additionally, we see only a weak dependence on viscosity with noticeable differences beginning with the strongest kinematic viscosity, which starts to suppress the VSI in the inner region. A further increase in viscosity would suppress the instability completely, as shown already in Nelson et al. (2013).

Since we are interested in the particle drift, we also show in Fig. 4 the radial velocity in the disc at 5 au as a function of height. We averaged from 1000 yr to 1800 yr, which is roughly the quasi-stationary phase. The radial velocity is inwards in the midplane and outwards in the corona. There are only minor differences in height were the direction of the flow changes. Interestingly, this profile is opposite to that of a laminar viscous flow, where it is outwards in the midplane, and inward near the disc surfaces (Urpin 1984; Kley & Lin 1992). Our findings are in agreement with results of isothermal MHD simulations of global turbulent accretion discs without a net magnetic vertical flux that also show gas inflow near the disc midplane and outflow in the disc's surface layers (Flock et al. 2011). Within the framework of viscous discs the vertical variation of α (shown in the lower panel of Fig. 2) will play a role in determining the $u_r(z)$-profile, see also Kley & Lin (1992) and Takeuchi & Lin (2002), who studied the $u_r(z)$-profile for constant α.

3.1. 3D-simulation: full disc

In this subsection we present a full disc, meaning an azimuthal domain from 0 to 2π in contrast to the 0 to $\pi/4$ of our fiducial model, in order to check the validity of our results obtained from calculations with the reduce domain. Since this full simulation is computationally expensive, we used a lower resolution of $512 \times 128 \times 512$. The full simulation is compared to the one eighth simulation of the disc with a resolution of $512 \times 128 \times 64$, which has the same azimuthal extent as the fiducial model, but not the resolution. We added a small dimensionless physical viscosity, $\nu = 10^{-7}$, to be independent of the unknown numerical viscosity, allowing better comparison with other simulations. To give an impression of possible differences in the flow structures, between the full and fiducial model, we display in Fig. 5, from top to bottom, the fluctuations of the density, and the radial and vertical velocity components in the midplane of the disc, where the top inset in each panel refers to the fiducial model with $\phi_{\max} = \pi/4$ and the bottom part to the full disc. The two top panels for the density and radial velocity clearly show non-axisymmetric, wave-like features in the disc. The bottom panel seems to indicate a more axisymmetric structure which is a result of the VSI eigenmode dominating the vertical motion in the disc, as seen above in Fig. 1.

To analyse the turbulent structure in more detail we calculated azimuthal power spectra of the radial and vertical kinetic energy fluctuations in the disc midplane for two different times, spatially averaged from 3 to 7 au. We can see in Fig. 6 that during the initial growth phase (top panel) the instability is driven at two length scales. The smaller one, at azimuthal wave numbers $m \approx 200$, is most likely due to the initial noise as given by the finite discretization which is enhanced by the growth phase of the instability. The larger one (at $m \approx 10$) is on the scale of the wavelength of the strongest growing VSI mode. This feature is also visible in the azimuthal direction even though the VSI should be axisymmetric. We speculate that this is due to a disturbance created in the radial direction by a Kelvin-Helmholtz instability that is sheared into the azimuthal direction. We can also see that in the quasi stationary phase (bottom panel) the turbulence decays faster than Kolmogorov turbulence for wavenumbers around $m \approx 20$, which is the scale at which the VSI is driven. There the energy is concentrated in the VSI modes and not in the turbulent kinetic energy and thus the model of Kolmogorov decay is not applicable (Dubrulle 1992). Only at small scales the vertical kinetic energy fluctuations decay with a Kolmogorov spectrum. This can be seen in both simulations. From this we infer that the local properties of the turbulence generated by the VSI are very similar for the restricted and full azimuthal domain and is already fully captured by the smaller disc.

To analyse the locality of the VSI further, we also compare the two point correlation functions for the two disc models. This is defined as

$$\xi_f(\Delta r, \Delta\phi) = \langle f(r,\phi) f(r + \Delta r(r), \phi + \Delta\phi) \rangle \,, \tag{10}$$

where f is the quantity to be correlated, which has a zero mean, $\langle f \rangle = 0$. We evaluate the correlation in the disc midplane and

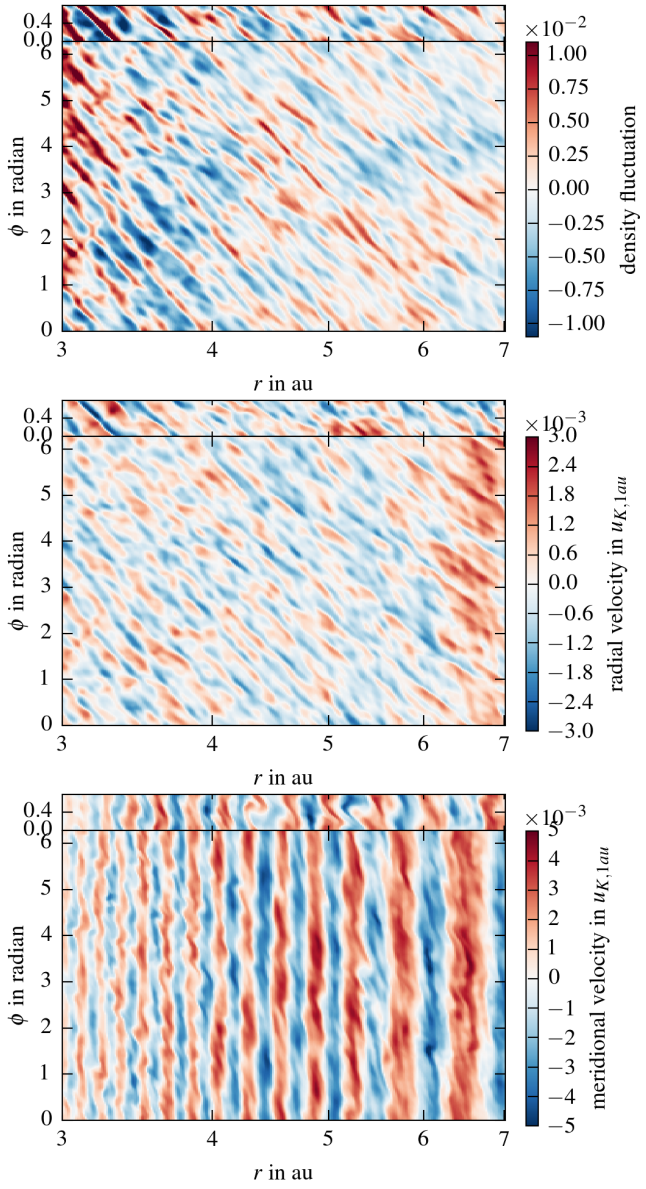

Fig. 5. Fluctuations of density, the radial and vertical velocity (*from top to bottom*) in the midplane of the disc with 3 to 7 au after 1700 yr. The *top part* in each panel refers to the fiducial model with one eighth of the full azimuthal domain while the full model is shown in the *lower part* of each panel.

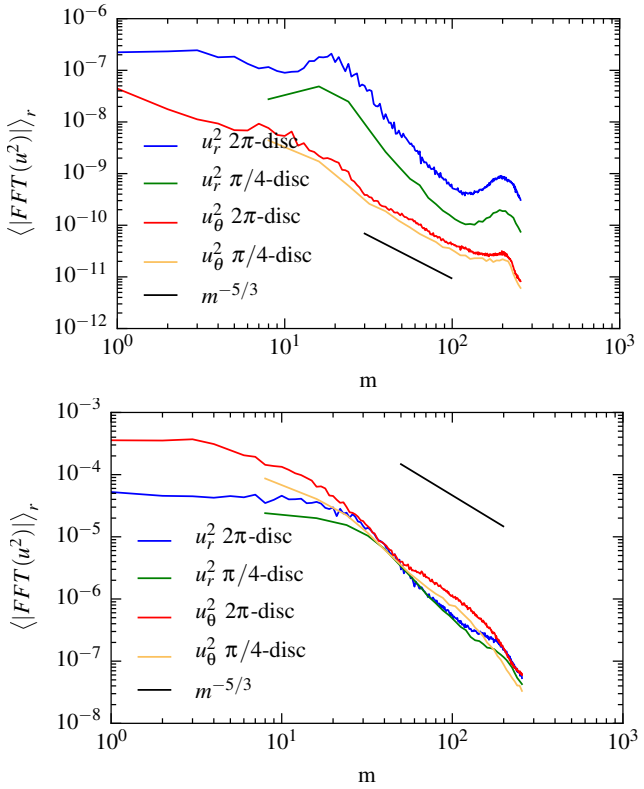

Fig. 6. Power spectrum for the different kinetic energy components along the azimuthal direction in the disc midplane averaged over the radial direction. The black line shows the Kolmogorov spectrum decaying with $|u(m)|^2 \propto m^{-5/3}$, where m denotes the azimuthal wave number. The *top panel* refers to the growth phase after 200 yr and the *lower panel* to the quasi-stationary phase after 1700 yr.

take the radial domain from 3 to 7 au, which we treat for this calculation as periodic. The correlations are evaluated on a logarithmic grid, to better capture the properties under investigation.

In Fig. 7 we present the results of the two point correlations for the density fluctuations and the radial and meridional velocity after 1700 yr. The fluctuations are clearly non-isotropic and correlated not only on a local scale but also weakly over the whole domain. We can see again that the smaller domain is a reasonable approximation to the larger domain, even though the correlations are enhanced in the smaller domain, but for the vertical velocity we have a global correlation for both cases. This again strengthens the impression that the fluctuations in azimuthal direction are driven by a Kelvin-Helmholtz instability that feeds off the strongest VSI mode. From this we conclude that our reduced domain captures all of the important physics even though it enforces stronger correlations[1].

The models for different levels of background viscosity were shown already in Fig. 3. The full model has a slightly smaller α, but is apart from this very similar. We also compared the results from the particle motions (not shown), but also only found minor differences. Hence, we conclude that we can use the reduced model with $\phi_{\max} = \pi/4$ to analyse the motion of embedded particles.

4. Isothermal discs with dust

The particles are added into the fiducial model after 200 yr when the VSI is reaching the quasi-stationary phase at the inner part of the disc. After further 800 yr both VSI and particles are then in quasi-equilibrium. The particles are inserted in the midplane, randomly distributed over the radius and azimuthal angle, with the velocity of the gas at their current position. If a particle leaves the domain in the inner edge we insert it again randomly positioned over 1 au at the outer edge. This ensures that a clump of particles that leaves the domain is sufficiently smoothed out when added again. We add 10 000 particles per size with 20 different sizes, beginning with 1 μm up to 3000 m. The Epstein regime is strictly valid only up to sizes of 10 m, and particles greater than that are added as a numerical experiment. Note, that

[1] A simulation with a quarter disc still shows the same enhanced correlations.

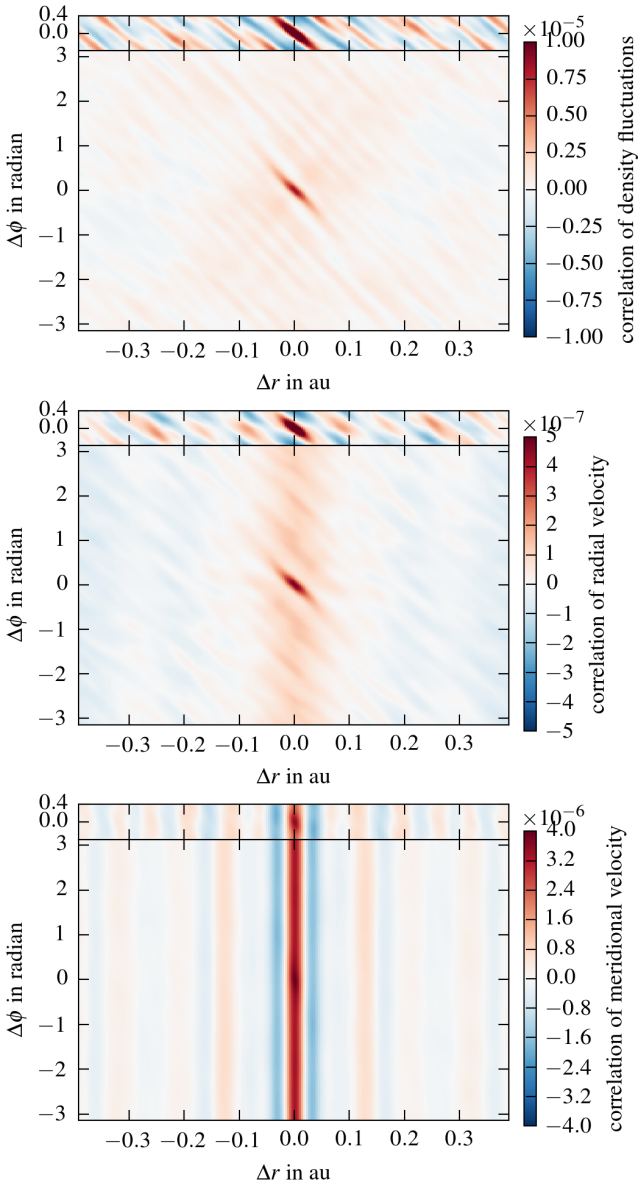

Fig. 7. Two point correlation of the density, the radial and vertical velocity (*from top to bottom*) in the midplane of the disc with 3 to 7 au after 1700 yr. The *top part* in each panel refers to the fiducial model with one eighth of the full azimuthal domain while the full model is shown in the *lower part* of each panel.

for the isothermal discs the scale for the density is not fixed and thus the particle size regime may be different for different choices of the disc density. This is not the case for the disc with radiation transport as shown in the next section, where the chosen disc mass (the density) fixes the disc temperature, and hence the disc scale height, through specific values of the opacity.

We begin with the results for the radial drift and diffusion of the dust particles, then we discuss the vertical diffusion and finally the relative velocity distribution for colliding particles. We discuss our results either in terms of the physical size of the particles or the stopping time. For the models in this section the correspondence between these can be read off from Table 1.

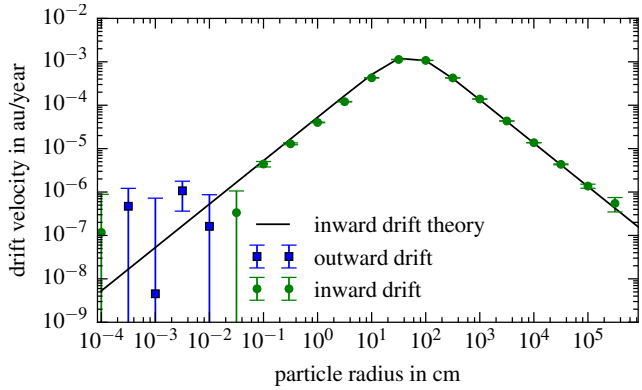

Fig. 8. Mean radial drift velocity of the dust particles depending on the radius of the particles at $r = 5$ au. This is compared to expected drift velocity for pressure supported discs as given by Eq. (11). Shown are isothermal disc simulation with resolution $1024\times256\times64$ from 1000 to 2000 yr. Different colours and symbols are used for inward and outward drift. We estimate the error from the radial diffusion coefficient.

4.1. Radial particle drift

The radial drift velocity for the dust in the midplane in the Epstein regime is given by (Nakagawa et al. 1986)

$$u_{\rm drift} = \frac{\partial \ln p}{\partial \ln R} \frac{(H/R)^2 u_{\rm K}}{\tau_{\rm s} + \tau_{\rm s}^{-1}}. \tag{11}$$

This is due to the drag force resulting from the difference between the Kepler velocity of the particles and the gas velocity, which is modified by the pressure support p. We use the midplane pressure for our theoretical curves, since most particles are in the midplane, at least the larger ones. Here $\tau_{\rm s}$ is the dimensionless stopping time (see Eq. (2)) and $u_{\rm K}$ is the Kepler velocity.

We start by comparing the radial drift of the dust particles in our simulation with this theoretical prediction for the drift velocity in Fig. 8. The results from the simulation are extracted by fitting a linear function to the mean radial position of the particles starting with a distance to the star of 5 ± 0.5 au. We fit over the span of 1000 yr beginning with 800 yr after inserting the particles or over the time the particles need to travel 0.5 au, whichever is smaller. The inwardly directed drift is plotted in green (dots), and outward drift in blue (squares). Since the error in the measurement of the velocity stems from the random walk of the particles due to the turbulence, we estimate the error from the radial diffusion coefficient (see Fig. 12). The error is then given by the half-width of the distribution divided by the square-root of the number of involved particles.

We can see that the speed of large particles is similar to the predictions. A difference in speed of approximately 20% can be seen for the smaller particles in a size range between 0.1 cm to 10 cm. This deviation can be partly attributed to the spread of the particles in the vertical direction, because particles not in the midplane have a longer stopping time (lower gas density), and the prediction is calculated using the stopping time of particles in the midplane. An additional factor is that they can be caught temporarily in small scale vortices (Johansen & Klahr 2005).

The drift velocity for the smallest particles can even be positive for some time intervals. This is shown for particles at 5 au in Fig. 8. At distances closer to the star they clearly drift inwards even though the gas momentum is the same (not shown). We return to the analysis for those particles later in Sect. 5.1, where the sign of the migration direction is better constraint.

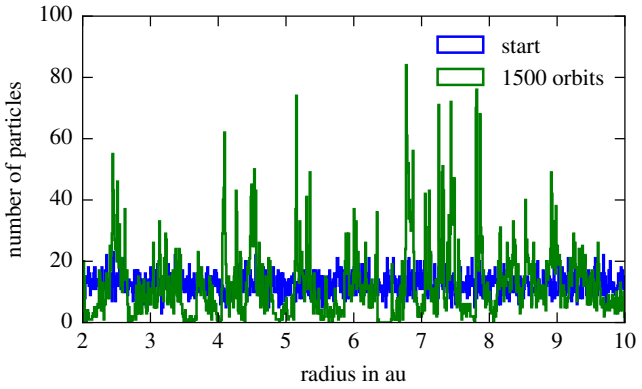

Fig. 9. Histogram of particles with size of 31 cm, after 1500 yr (green line) and at the start (blue line, Poisson distributed). We divide the distance from the star from 2 to 10 au into 800 bins and count the number of particles in each bin. The average number of particles per bin is 12.5.

An interesting behaviour of the particles is shown in the histogram in Fig. 9. For this plot we divide the distance from the star from 2 to 10 au into 800 equal sized bins and count the number of particles per bin. We can clearly see that 1500 yr after we inserted the particles, the distribution clearly deviates from the initial Poisson distribution and instead they clump together. This happens only for particles with a dimensionless stopping time of the order of unity.

To further illustrate this feature, we show the number of particles per radial bin over time for different particles sizes in Fig. 10. We note that the colour scale is logarithmic. For this image and the following analysis we correct the particle density per 1 au to remain constant, as it was at the beginning of the simulations, by weighting the number of particles per bin by the number of particles per 1 au. Since the particles move faster in the inner region and the particles that leave the inner region are added in the outer region, we would produce overdensities otherwise. This does not change the bunching statistics, however.

After we insert the particles, the VSI is only active in the inner region, but is quickly spreading out to the whole disc, until after 1000 yr the whole domain is active. One can see that the onset of the VSI leads to bunching of the particles. Due to the bunching we can clearly see the different drift velocities of the particles. But we can also see that at certain radii the particles are sometimes caught in the pressure fluctuations for a short time before moving on, which leads to the visible lines in the image.

To make the dynamics involved clearer, we calculate another statistic property. This time we count how often a certain number of particles in a radial bin occurs. We average over 50 snapshots, each 10 yr apart, beginning 1300 yr after we inserted the particles. We then normalise by the total number of particles to find the probability for certain number of particles in a radial bin with width $\Delta r = 0.01$. This is shown in Fig. 11.

We can see that for the limit of small stopping time we still follow the initial Poisson distribution, which has its peak at 12.5 particles per bin (the average number) and decays with $\propto\exp(-n^2)$. These particles are tightly coupled to the gas and can not be caught in pressure fluctuations. In contrast, particles with (dimensionless) stopping time near unity decay with $\propto\exp(-n)$. This increases the likelihood to find bins with a high number of particles which can easily lead to overdensities in dust by a factor of around 10. This is caused by short lived pressure fluctuations originating from the VSI, which briefly slow down the crossing particles. The largest particles again revert to the Poisson statistics, since they are not coupled to the gas.

4.2. Radial diffusion of particles

Next we compare the radial diffusion of the embedded particles with theoretical predictions. Since the power spectra of $u_r, \delta u_\phi, u_\theta$ are similar, the radial diffusion coefficient for particles (Youdin & Lithwick 2007) is given by

$$D_{\mathrm{d},r} = t_{\mathrm{eddy}} \frac{\left\langle u_r^2 \right\rangle + 4\tau_\mathrm{s}^2 \left\langle \delta u_\phi^2 \right\rangle + 4\tau_\mathrm{s} \left\langle u_r \delta u_\phi \right\rangle}{\left(1+\tau_\mathrm{s}^2\right)^2}. \tag{12}$$

For the simulation used for Fig. 12 we measure $\left\langle u_r^2 \right\rangle_{r,\phi,t} = \left\langle \delta u_\phi^2 \right\rangle_{r,\phi,t} = 2 \times 10^{-6} \cdot u_{\mathrm{K},1\,\mathrm{au}}^2$ and $\left\langle u_r \delta u_\phi \right\rangle_{r,\phi,t} \leqslant 10^{-8} \cdot u_{\mathrm{K},1\,\mathrm{au}}^2$ near the midplane, indicating isotropic turbulence. With these values and Eq. (11) for the radial drift we can use the radial diffusion to measure t_{eddy}. Surprisingly, from this we calculate a small dimensionless, $\tau_{\mathrm{eddy}} = t_{\mathrm{eddy}}\Omega_\mathrm{K}$ of 0.1, compared with the large-scale oscillations of the VSI on a timescale of 5 orbits per oscillation.

In Fig. 12 we show the radial distribution of particles with different sizes from which we extracted the radial drift and diffusion during a timespan of 100 yr for different particle sizes, again for particles starting at 5 ± 0.5 au. While the smallest particles (blue and green curves) follow directly the prediction, the particles with $\tau_\mathrm{s} = 0.19$ (red curve) seem to lag behind the theoretical curve. As described below this difference is caused by the fact that the particles are more spread out vertically. Even larger particles (yellow) again show bunching behaviour and are collected in two distinct peaks, due to being caught in different VSI waves.

From this we can also calculate the radial Schmidt number, which Youdin & Lithwick (2007) determine for homogeneous isotropic turbulence in the xy-plane with $\left\langle u_r^2 \right\rangle = \left\langle \delta u_\phi^2 \right\rangle$, to be

$$\mathrm{Sc}_r = \frac{D_{\mathrm{g},r}}{D_{\mathrm{p},r}} = \frac{\left(1+\tau_\mathrm{s}^2\right)^2}{1+4\tau_\mathrm{s}^2}, \tag{13}$$

where for the gas diffusion coefficient, $D_{\mathrm{g},r}$, we use in our case the dust diffusion of the smallest particles.

For smaller particles we find good agreement with Eq. (13) but for τ_s of unity and larger, we measure Schmidt numbers smaller as predicted by Eq. (13) by a factor up to three at a stopping time of $\tau_\mathrm{s} = 200$. This is just noticeable in Fig. 12 for the stopping time of $\tau_\mathrm{s} = 1.9$. There we can see that the predicted diffusion fits a single peak well, but not the whole curve, which is 50% wider. This can be explained by particles crossing large-scale VSI modes which are not expected by the theoretical model of homogeneous isotropic turbulence used to calculate the predictions for the Schmidt number.

4.3. Vertical diffusion of particles

After the radial diffusion shows a small eddy lifetime, we are now interested in the vertical diffusion. In Fig. 13 we selected particles between 4.5 and 5.5 au and calculated a histogram of the vertical position to show the vertical distribution of different sized dust particles. For better statistics we added up the 50 last snapshots, spanning from 1200 yr to 1700 yr. While the small particles with stopping time smaller than unity show the expected Gaussian distribution with a scale height equal to the

A&A 594, A57 (2016)

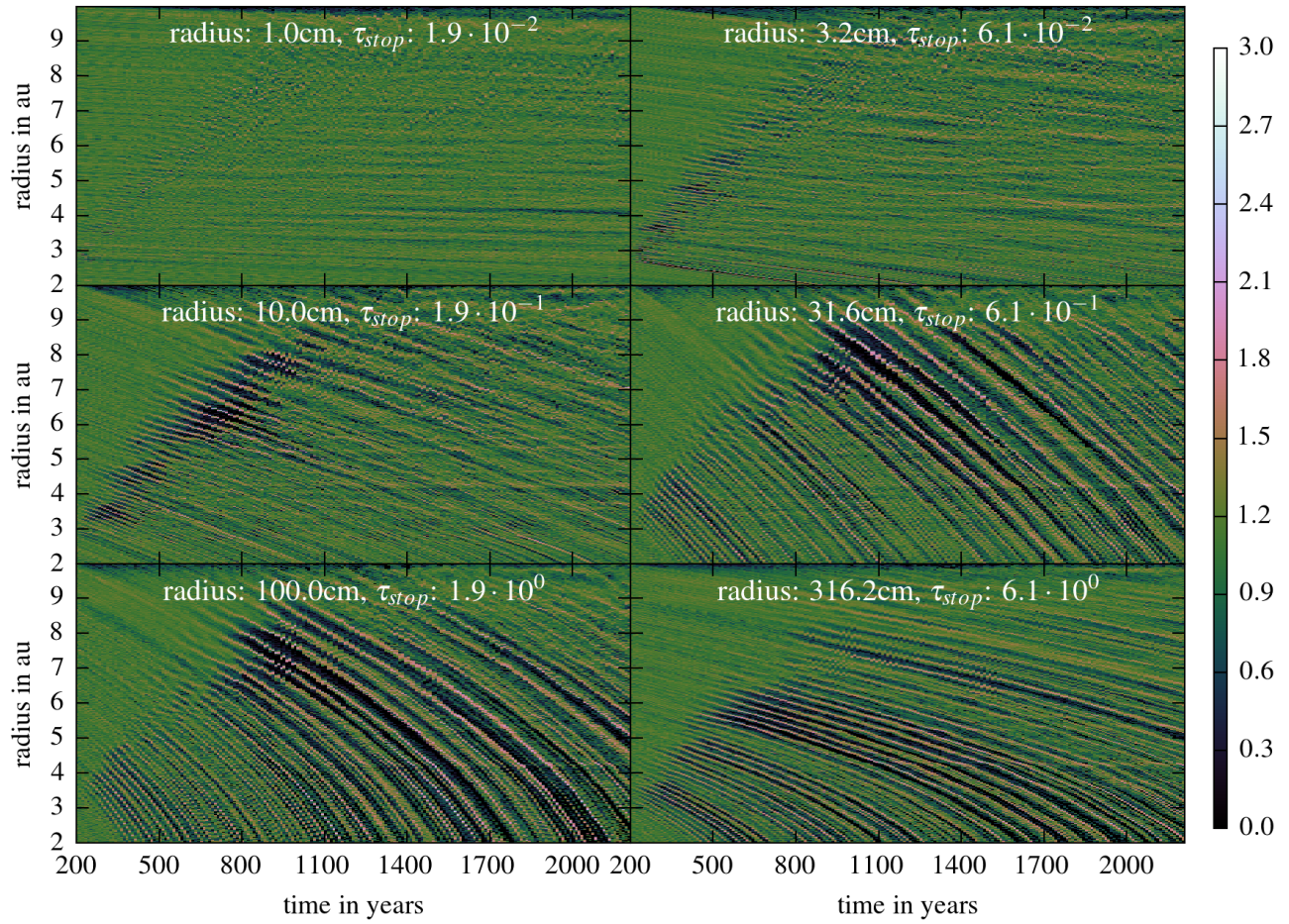

Fig. 10. Visualisation of the radial drift of the particles. We show the logarithm with base 10 of the number of particles per bin. One can see the clumping behaviour as the VSI growths, but also the velocity of the particles.

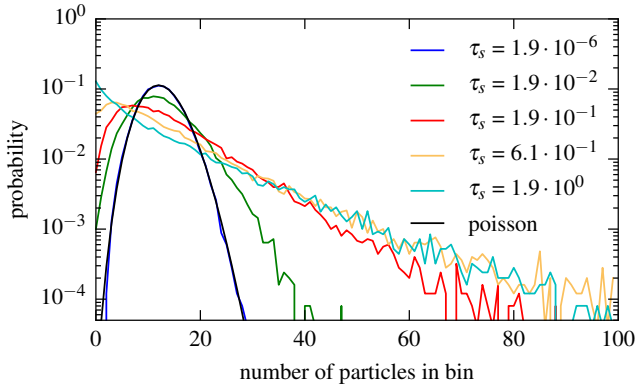

Fig. 11. Probability to find a certain number of particles in a radial bin with $\Delta r = 0.01$ au in the region from 3 to 9 au, for different stopping times (refer to Fig. 9). The average number of particles per bin is 12.5. We averaged over 50 snapshots, each 10 yr apart, beginning with year 1500.

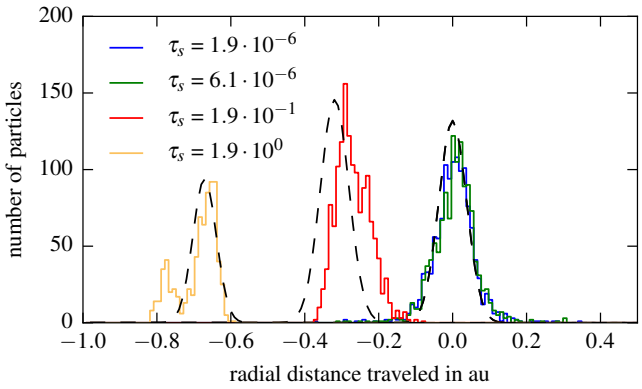

Fig. 12. Radial particle diffusion over 100 yr, after 1000 yr. The black dashed lines are calculated from theory for the different stopping times and with $\tau_{\text{eddy}} = 0.1$ and $\langle u_{g,r}^2 \rangle = 2 \times 10^{-6} \cdot u_{\text{K,1 au}}^2$, see Eq. (12).

gas scale height, the particles with stopping time around unity clearly deviate from this. This can be explained by the large-scale velocity pattern of the gas with active vertical shear as displayed in Fig. 1. The corrugation mode of the gas will move the particles upward away from the disc's midplane, up to the point where the density of the gas is so small that the drag force can no longer overpower gravity. The particle then can swiftly "surf" on the updraft of the large-scale VSI-mode. Since these corrugation modes oscillate, the particles will also oscillate around the midplane.

Table 1. Measured dust scale heights and inferred eddy lifetimes, from Eq. (14), for the inviscid isothermal model.

Radius cm	Stopping time τ_s at 5 au	$h_{p,z}$ h_{gas}	$\tau_{eddy,z}$ at 5 au
1.0×10^{-4}	1.9×10^{-6}	1.0×10^{0}	–
3.2×10^{-4}	6.1×10^{-6}	9.9×10^{-1}	–
1.0×10^{-3}	1.9×10^{-5}	9.3×10^{-1}	–
3.2×10^{-3}	6.1×10^{-5}	8.5×10^{-1}	–
1.0×10^{-2}	1.9×10^{-4}	8.3×10^{-1}	–
3.2×10^{-2}	6.1×10^{-4}	7.6×10^{-1}	8.1×10^{-2}
1.0×10^{-1}	1.9×10^{-3}	6.6×10^{-1}	1.4×10^{-1}
3.2×10^{-1}	6.1×10^{-3}	5.1×10^{-1}	2.1×10^{-1}
1.0×10^{0}	1.9×10^{-2}	4.3×10^{-1}	4.3×10^{-1}
3.2×10^{0}	6.1×10^{-2}	3.0×10^{-1}	6.1×10^{-1}
1.0×10^{1}	1.9×10^{-1}	1.9×10^{-1}	7.0×10^{-1}
3.2×10^{1}	6.1×10^{-1}	9.4×10^{-2}	5.4×10^{-1}
1.0×10^{2}	1.9×10^{0}	3.5×10^{-2}	2.3×10^{-1}
3.2×10^{2}	6.1×10^{0}	1.8×10^{-2}	1.9×10^{-1}
1.0×10^{3}	1.9×10^{1}	6.7×10^{-3}	8.6×10^{-2}

Notes. A Gaussian $f(z) = N_0 \exp(-(z \pm \mu)^2/(2r^2 h_p^2)$ was fitted to the data of the vertical distribution to find h_p and calculated τ_{eddy}. The first five values for τ_{eddy} were not calculated, since the gas scale height is nearly equal to the dust scale height.

For isotropic turbulence Dubrulle et al. (1995) and Zhu et al. (2015) calculate a dust scale height of

$$h_p = \frac{h}{\sqrt{H^2 \Omega^2 t_s / \left(\left\langle u_z^2 \right\rangle t_{eddy}\right) + 1}}, \tag{14}$$

where $h = H/R$ is the relative gas scale height. Together with the measured velocity dispersion $\langle u_z^2 \rangle = 5 \times 10^{-6} \cdot u_{K,1\,au}^2$ we can use this equation to calculate again the eddy timescale by fitting a Gaussian to the data for different stopping times, thus extracting the dust scale height. We note that for a very small stopping time this does not work, since the dust scale height is equal to the gas scale height, independent of the eddy time scale. Also we superimpose two Gaussian with the same scale height for the distributions with two peaks, which then fits well. These peaks are then usually two scale heights apart for particles with dimensionless stopping time around one. Without this scheme, we would get a larger scale height and thus a longer eddy lifetime, which makes sense, since they are caused by the large-scale structures that have a long life time. We present the results in Table 1. Again we find $\tau_{eddy} \approx 0.2$, which is similar for other types of turbulence, for example MRI has $\tau_{eddy} \approx 1$ (Youdin & Lithwick 2007; Carballido et al. 2011). We note that the longer eddy lifetimes for the larger particles indicate that the eddy lifetime is longer in the midplane, since the smaller particles also see the eddy lifetime of the corona.

4.4. Collision statistics

In this section we evaluate the relative velocity distribution for colliding particles. Since we do not have enough particles to directly measure this distribution, we take each particle between 4 and 7 au and check for other particles in a sphere with radius smaller than 0.05 au. To make them independent of translation we remove the Kepler velocity (for independence of radius) and rotate all particles into the same r-θ plane, after we calculate the distance (for independence of the azimuthal angle, since they are all in circular orbits). We then calculate histograms of the relative velocity between two particles depending on the size of the particles. We normalise by the number of particles to get a probability.

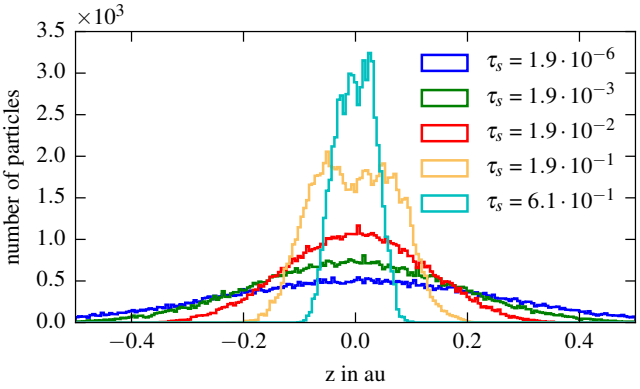

Fig. 13. Vertical distribution of the particles depending on size, summed over 50 snapshots in the interval from 1200 to 1700 yr. Bin size is $\Delta z = 0.02$ au.

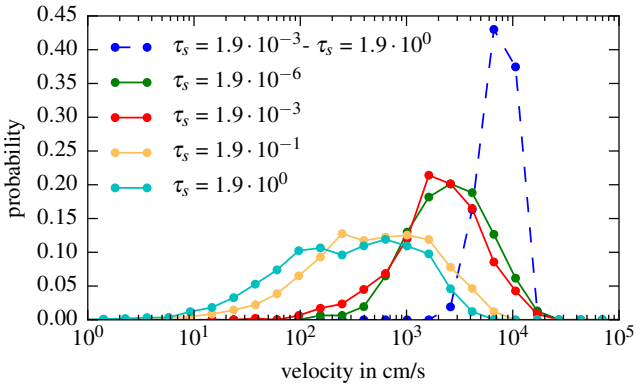

Fig. 14. Relative velocity between particles for different stopping times after 2200 yr. The dashed line represents particles of different sizes and the solid lines denote collisions between same sized particles. Only particles with separation smaller than 0.05 au are considered for potential collisions. Lines to guide the eye.

This can be seen in Fig. 14. Lost by the normalization procedure is the fact that there are around 300 same sized particles in the sphere for small particles, while there are around 11 000 same sized particles with stopping time around unity in the sphere. Since the median relative velocity for larger particles is reduced by an order of magnitude relative to the smaller particles, the number of collisions will also be reduced. The blue dashed line represents the relative velocity between small and large particles, since those are dominated by the velocity difference that is created by the strongly coupled small particles, moving with the gas, and weakly coupled particles moving with Keplerian velocity.

Using an alternative way of estimating the bunching behaviour of particles, we also calculate the pair correlation function $g(r)$.

$$g(r) = \frac{V}{\pi r \Delta r N^2} \sum_{i}^{N} \sum_{j \neq i}^{N} \delta(r - d_{ij}), \tag{15}$$

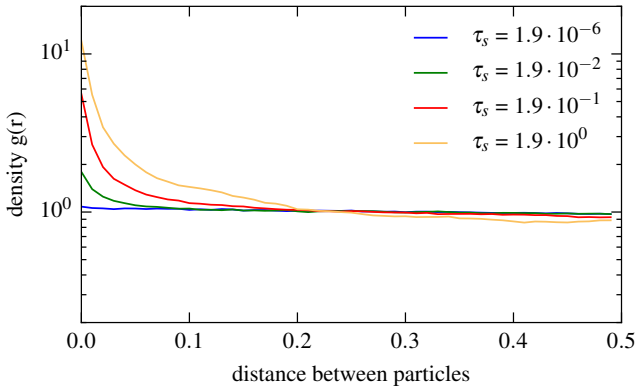

Fig. 15. Pair correlation function: enhancement of surface density in a shell with radius r for different stopping times. Averaged over 5 snapshots in the interval from 1800 to 2200 yr.

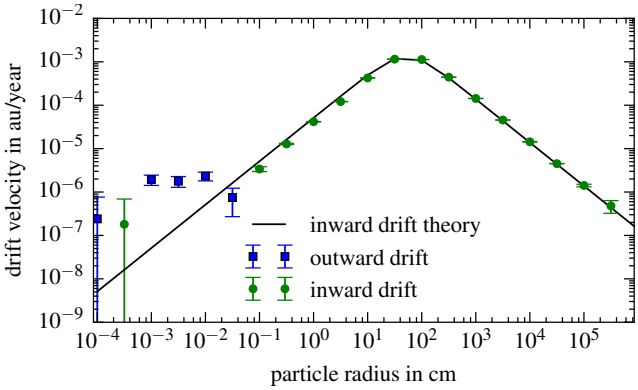

Fig. 16. Drift velocity of the dust particles depending on the radius of the particles at $r = 5$ au for a viscous disc. This is compared to expected transport for pressure supported discs. Simulation with resolution $1024 \times 256 \times 64$ and viscosity $\nu = 5 \times 10^{-7}$. Different colours are used for inward and outward drift. We estimate the error from the radial diffusion coefficient.

where V is the area of integration, d_{ij} is the distance between particle i and j and $\delta(r)$ is one if $|r| < \Delta r/2$ and we use $\Delta r = 0.01$ au. This function returns one for Poisson distributed particles and greater than one if there is an increased surface density in the ring around the particles at this radius and thus picks up 2D clustering instead of the 1D clustering in the earlier analysis. We calculate this property for particles between 4 and 7 au projected in the $r-\phi$ plane, and show it for different particle sizes in Fig. 15. We can see that small particle positions are uncorrelated, but the particle positions with stopping time near unity display a clear correlation, as we could already infer from Fig. 11. Particles with a stopping time closer to unity have a larger correlation length. This makes the VSI a possible candidate to trigger the streaming instability.

5. 3D-simulations: viscosity

In this section we present the same simulation but using now a dimensionless kinematic viscosity coefficient of $\nu = 5 \times 10^{-7}$, in order to check the influence of viscosity, which in turn influences the α-parameter and the velocity dispersion. We also add the same amount of viscosity to the model with radiation transport, as shown below. This viscosity corresponds to an α-value of 9×10^{-5} at 5 au or 4×10^{-5} at 25 au. There it limits the smallest length scale of the VSI, which can not be resolved otherwise. We only show the results if there is a clear difference to the previous simulation. From the hydro-dynamic perspective they are very similar, but the α-parameter is smaller by a factor of 2 and the wavelength of the instability slightly smaller.

5.1. Radial drift

If we include viscosity and repeat the analysis for radial drift, here from 2700 yr to 3700 yr, due to the slower diffusion, we can see in Fig. 16 that particles larger than about 0.1 cm drift inward with approximately the theoretical speed (see Eq. (11)) with slightly higher deviations than in the inviscid case. The smallest particles now clearly drift away from the star at $r = 5$ au. This is true for different radii of the disc.

In Fig. 17 we see that the particles are moving inwards at the midplane and outwards otherwise. The smallest particles follow the gas velocity and larger particles are moving outwards away from the midplane faster than the gas, similar to Takeuchi & Lin (2002), where they move outwards even though the gas is moving inwards, due to the gas being super-Keplerian in the disc's corona. This leads to a massflow (shown in Fig. 18) that is inward in the midplane and outward farther away from the midplane. As seen in Figs. 17 and 18 small particles (blue and green line) show the same radial velocity profile and mass flux behaviour as the disk's gas flow (black dashed lines). To estimate the overall mean flow of the particles it is necessary to consider the vertical dependence of the mass flow (Fig. 18) rather than the radial velocity z-profile (Fig. 17). For example, from Fig. 17 we notice that the particles with stopping time $\tau = 6.1 \times 10^{-5}$ (green line, 3.2×10^{-3} cm radius) move inward slower than the particles with stopping time $\tau = 6.1\times10^{-4}$ (red line, 3.2×10^{-2} cm radius) even though the mean radial dust velocities in Fig. 16 are *smaller* for the larger particles. This is due to the different vertical distribution of the particles (see Fig. 18 and Table 2). In addition, the velocity and mass flow profiles of the smallest displayed particles (blue lines in Figs. 17 and 18, 3.2×10^{-4} cm radius) look very similar to the particles with stopping time $\tau = 6.1 \times 10^{-5}$ (green line), while having drift rates in the opposite direction in Fig. 16.

Thus the net particle flow is very sensitive to the gas flow profile and the ratio of particles near the midplane, which is decided by the stopping time. This also means that, independent of the mean flow, there will always be a small fraction of particles drifting away from the star, faster than one would expect from diffusion alone.

5.2. Radial diffusion

The increase in viscosity leads to an decrease of the velocity dispersion to $\langle u_r^2 \rangle = 1\times10^{-6} \cdot u^2_{\mathrm{Kepler,1\ au}}$ which is smaller by a factor of two. In Fig. 19 we compare our results to theoretical predictions with $\tau_{\mathrm{eddy}} = 0.1$. The diffusion is clearly smaller than in the inviscid case, as predicted by the decreased velocity dispersion. This is in contrast to the vertical eddy lifetime were we measure an increase in eddy lifetime due to vertical diffusion.

We can also see (right wing of green and blue curves) that a small fraction of the small particles diffuse faster outwards than the rest of the particles. These are particles far away from the midplane, where the stopping time is magnitudes longer, typically longer than 10^{-2}, and the gas flow is in average outwards. These weaker coupled particles can quickly travel a short distance away from the star, before drifting back inwards nearer to

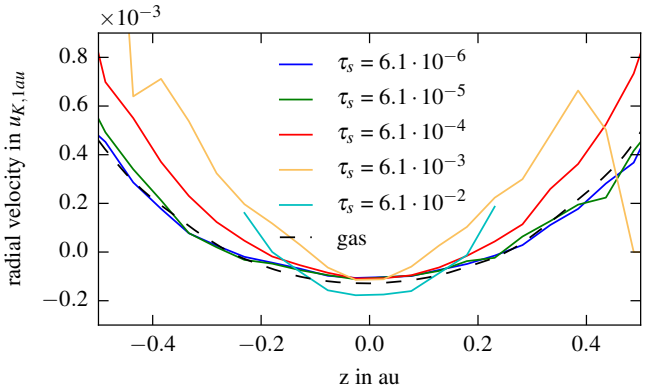

Fig. 17. Drift velocity of the dust particles at $r = 5$ au depending on the vertical direction compared to the gas velocity for the simulation with viscosity $\nu = 5 \times 10^{-7}$ averaged from 2700 to 3700 yr.

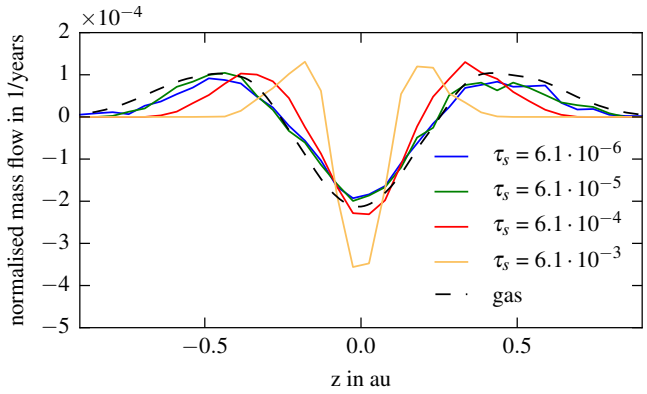

Fig. 18. Normalised mass flux $u_{\rm drift}\rho/\Sigma$ at $r = 5$ au for the simulation with viscosity $\nu = 5 \times 10^{-7}$ averaged from 2700 to 3700 yr.

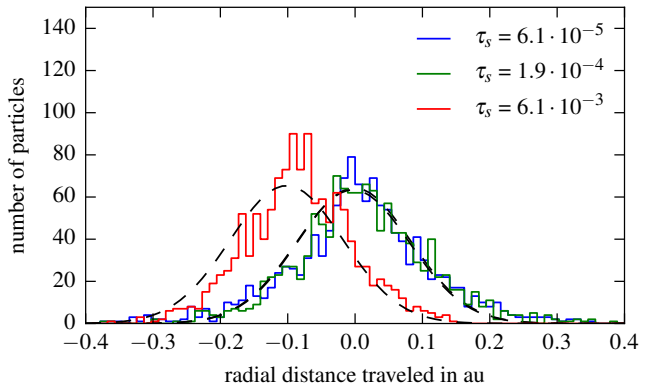

Fig. 19. Radial diffusion over 1000 yr after 2700 yr for the simulation with viscosity $\nu = 5 \times 10^{-7}$. The dashed lines are calculated from theory for the different stopping times and with the same $\tau_{\rm eddy} = 0.1$ and $\langle u^2_{\rm gas,radial}\rangle = 1 \times 10^{-6} \cdot u^2_{\rm Kepler,1\ au}$. Compare with Fig. 12, but note that here the particles had 10 times as much time to diffuse.

the midplane. The difference in radial drift between theory and simulation noticed in Fig. 16 causes the offset for the results of the longer stopping time (red curve).

Table 2. Measured dust scale heights and inferred eddy lifetimes, from Eq. (14), for the viscous isothermal model.

Radius cm	Stopping time $\tau_{\rm s}$ at 5 au	$h_{{\rm p},z}$ $h_{\rm gas}$	$\tau_{{\rm eddy},z}$ at 5 au
1.0×10^{-4}	1.9×10^{-6}	9.5×10^{-1}	–
3.2×10^{-4}	6.1×10^{-6}	9.4×10^{-1}	–
1.0×10^{-3}	1.9×10^{-5}	1.0×10^{0}	–
3.2×10^{-3}	6.1×10^{-5}	9.5×10^{-1}	–
1.0×10^{-2}	1.9×10^{-4}	8.9×10^{-1}	–
3.2×10^{-2}	6.1×10^{-4}	8.0×10^{-1}	1.0×10^{-1}
1.0×10^{-1}	1.9×10^{-3}	5.5×10^{-1}	8.1×10^{-2}
3.2×10^{-1}	6.1×10^{-3}	3.9×10^{-1}	1.1×10^{-1}
1.0×10^{0}	1.9×10^{-2}	3.3×10^{-1}	2.2×10^{-1}
3.2×10^{0}	6.1×10^{-2}	2.8×10^{-1}	4.8×10^{-1}
1.0×10^{1}	1.9×10^{-1}	2.1×10^{-1}	8.3×10^{-1}
3.2×10^{1}	6.1×10^{-1}	9.4×10^{-2}	5.2×10^{-1}

Notes. We fitted a Gaussian $f(z) = N_0 \exp\left(-(z \pm \mu)^2/(2r^2 h_{\rm p}^2)\right)$ to the data of the vertical distribution to find $h_{\rm p}$ and calculated $\tau_{\rm eddy}$ for the simulation with viscosity of 5×10^{-7}.

5.3. Vertical Diffusion

For vertical diffusion we obtain slightly longer eddy lifetimes as can be seen in Table 2 where we measured from 2700 yr to 3700 yr. In these simulations it took four times as long for the dust scale height to converge to the gas scale height for the smallest particles, even though the vertical velocity dispersion is identical to the inviscid case.

5.4. Clustering

Finally we present the particle distribution in the $r - \phi$ plane in Fig. 20. We show the particles with dimensionless stopping time of $\tau_{\rm s} = 0.6$ and $\tau_{\rm s} = 1.9$ at 5 au. One can see for both displayed particles sizes that the VSI modes have produced nearly axisymmetric clusters. The bunching leading to the ring structure is strongest for the simulation with high viscosity. We also show in Fig. 21 the same effect for the full disc with small viscosity of 10^{-7} and resolution of $512 \times 128 \times 512$. For this simulation we also increased the number of particles to 500 000. We can see that the ring structure already seen in the histogram of Fig. 9 does indeed persist even in a full disc. Particles with more than a magnitude longer or smaller stopping time do not show this features.

6. 3D-simulations: radiative model

In this section we present the results for a radiative disc with radiation transport and irradiation from the central star. In contrast to our first paper (Stoll & Kley 2014), we model the stellar irradiation in a more realistic fashion as coming from the central star, similar to the treatment in Bitsch et al. (2013). This star has a temperature of 4000 K and a radius of $4\,R_\odot$.

6.1. Setup

For this simulation we have to take into account that the cooling time has to be sufficiently small for the VSI to be active (Nelson et al. 2013; Lin & Youdin 2015), which made changes in the domain necessary. We moved the radial extent of the disc

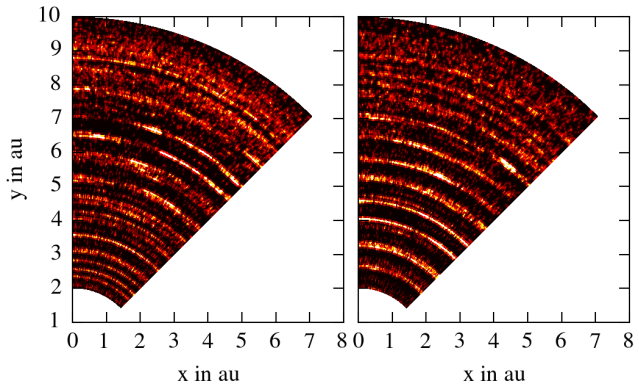

Fig. 20. Dust distribution for the disc with viscosity of 5×10^{-7}. Shown are the particles with dimensionless stopping time $\tau_s = 0.6$ (*left panel*) and $\tau_s = 1.9$ (*right panel*) at 5 au.

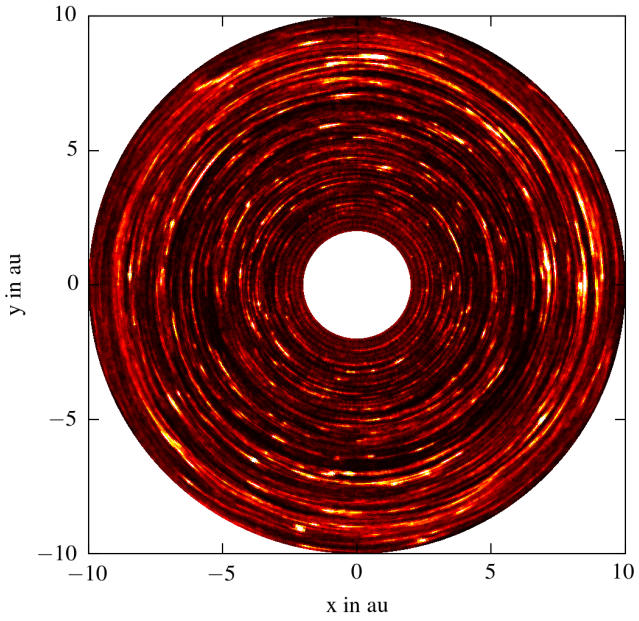

Fig. 21. Dust distribution for the full disc with viscosity of 10^{-7}. Shown are the particles with dimensionless stopping time $\tau_s = 0.6$. For this simulation we added 500 000 particles of the same size after 3400 yr and let them evolve for 400 yr.

for the inner boundary from 2 to 8 au and for the outer boundary from 10 to 80 au. This radial range is expected to be the active region of the VSI (Lin & Youdin 2015). We simulate again one eighth of the disc in the azimuthal direction and this domain is resolved by $1200 \times 260 \times 60$ grid cells. We also changed the density profile exponent from $p = -1.5$ to a value that is more in line with the observations $p = -1.8$ (Williams & Cieza 2011). Initially the temperature drops with $T = T_0 \cdot r^{-1}/r_0$, thus we have $\rho = 10^{-9}\,\mathrm{g/cm^3} \cdot r^{-1.8}/r_0$. This translates to $\Sigma = 1700\,\mathrm{g/cm^2}$ at 1 au, which corresponds to is the MMSN-model with a shallower decay of the density. The radiation transport then quickly leads to a new equilibrium with $T = 900\,\mathrm{K} \cdot r^{-0.6}/r_0$ in the corona and $T = 700\,\mathrm{K} \cdot r^{q}/r_0$ in the midplane, where the temperature gradient exponent q varies slightly around the mean of $q = -0.9$, from $q = -1.1$ in the inner region to $q = -0.6$ in the outer region.

During the evolution to the new equilibrium we damp the velocities in the whole disc.

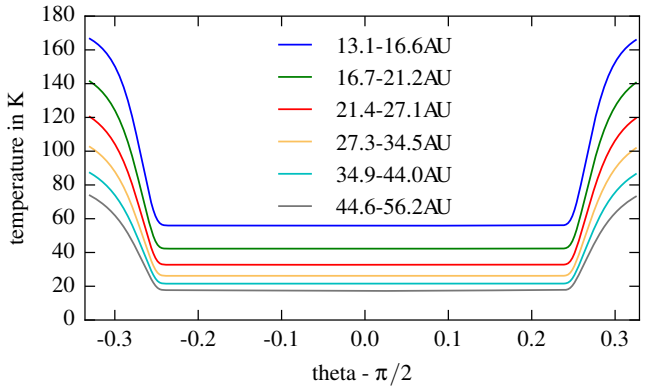

Fig. 22. Vertical temperature profile for the irradiated disc in the quasi-equilibrium state at different distances from the central star.

We add a small viscosity of $\nu = 5 \times 10^{-7}$. This suppresses the VSI in the inner region, where it would otherwise be weakly active, but due to a wavelength on grid scale clearly not resolved, which in turn would lead to unphysical numerical artifacts. As shown above, we observe only a small change of the VSI activity in the active domain with viscosity enabled compared to the inviscid case. Thus we see no harm in adding it.

In our first paper on the behaviour of the VSI in radiative discs we only considered vertical irradiation onto the disc surfaces (Stoll & Kley 2014). Here, we make the simulations more realistic and irradiate the disc from a central stellar source from the origin along the radial direction, see Bitsch et al. (2013). In this procedure the inner rim of the disc in our simulation is directly exposed to the stellar irradiation. To prevent unphysical heating of the midplane at the inner boundary, we absorb the irradiation flux coming from the star in a fictitious ghost cells with a width 0.25 au using the gas properties of the adjacent innermost active cells of the domain.

For the irradiation opacity we choose a value 10 times higher than the gas opacity, to compensate for the fact, that this radiation is emitted by a hot star and not the surrounding gas. This leads to a heated corona with a cooler midplane as can be seen in Fig. 22, instead of the cooler corona in Stoll & Kley (2014). At the boundary of the corona we can also see a change in the VSI mode. They have a larger wavelength in the hotter corona region and split where the temperature changes to a smaller wavelength in the midplane, see lower panel Fig. 24.

To make a direct comparison between the isothermal and radiative case, we ran an additional isothermal model with $p = -1.8$ and $q = -0.9$ and $\nu = 5 \times 10^{-5}$ and damping in the vertical and radial velocity in the region between 8 and 10 au to avoid boundary effects. In principle one could also compare the radiative case directly to the isothermal models from Sect. 4, because in isothermal simulations the unit of length is not fixed and can be scaled to a different regime. However, the gradients in density and temperature are not the same. We thus included a new isothermal model that can be directly compared to.

6.2. Hydrodynamic properties

We begin by presenting the α-parameter in Fig. 23, here calculated by time averaging the azimuthal velocity, since the equilibrium velocity cannot be computed analytically for radiative discs with a vertically varying temperature. In the inner region the VSI is suppressed by the viscosity of $\nu = 5 \times 10^{-7}$ on small wavelengths and by the high cooling time on large wavelengths.

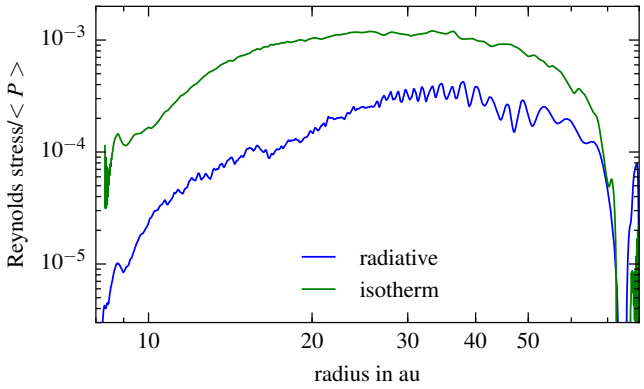

Fig. 23. α-parameter for the irradiated disc, calculated with time averaging. We average from 7500 yr to 37 500 yr using 60 snapshots.

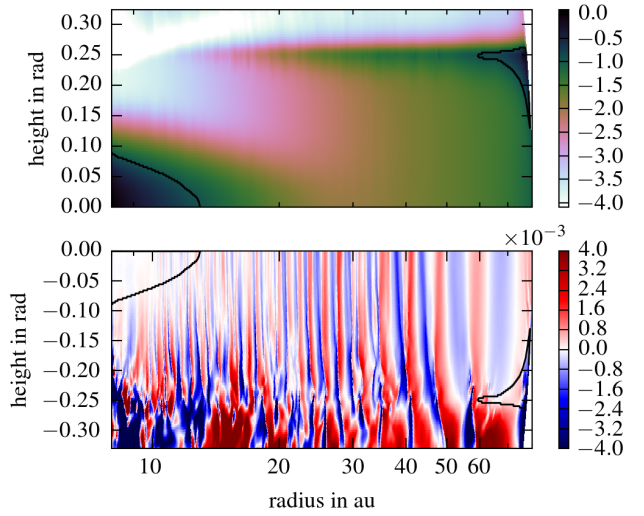

Fig. 24. Dimensionless cooling time (*upper panel*) and vertical velocity (*lower panel*) for the irradiated disc after 13 500 yr. The *top panel* shows the upper half of the disc while the *lower panel* the lower one at the same time slice. The black line indicates the location of the critical cooling time $\tau_{\rm crit}$ (see text), which separates the active from the inactive region.

Compare this to the isothermal simulation, where the same viscosity is not able to suppress even at 4 au (see Fig. 3). This is followed by an active region beginning at 15 au, where we reach $\alpha = (1\text{–}4) \times 10^{-4}$, which is still smaller than the isothermal simulations. The drop off in the outer region may be linked to the reduced activity in this region, see also Fig. 24, but is also visible in the isothermal model.

As the VSI is critically dependent on small cooling times, we analyse the cooling times due to radiative diffusion in the irradiated disc models. The radiative diffusion coefficient is given by:

$$\eta_{\rm rad} = \frac{4\lambda a c T^3}{\kappa_{\rm R} \rho^2 c_v}, \tag{16}$$

where λ is the flux limiter, a the radiation constant, c the speed of light and $\kappa_{\rm R}$ the Rosseland mean opacity. To calculate the cooling time we also need the appropriate length scale. For the optically thick region we simply take the length scale of the perturbation, which we approximate as a fourth of the scale height $l_{\rm thick} = H/4$. In the optically thin region we use the optical mean free path $l_{\rm thin} = 1/\kappa_R \rho$ for the length scale. This leads to a combined dimensionless cooling time of

$$\tau_{\rm cool} = \frac{l_{\rm thick}^2 + l_{\rm thin}^2}{\eta_{\rm rad}} \Omega_{\rm K}. \tag{17}$$

In Fig. 24 we compare the cooling time, $\tau_{\rm cool}$, as calculated from our numerical irradiated disc models with the critical cooling time, $\tau_{\rm crit}$, as estimated by Lin & Youdin (2015), who compared the destabilising vertical shear rates with the stabilising vertical buoyancy frequency. They obtained

$$\tau_{\rm crit} = \frac{h|q|}{1-\gamma}. \tag{18}$$

We see a good agreement in the inner region between the active regions as predicted by the critical cooling time and the active regions in our simulation. The inner midplane region up to 10 au is completely inactive and the following region which is also predicted to be inactive is only active with a higher order mode. We note that without viscosity one expects modes with higher wavenumber in this region.

In the outer region beyond 60 au the VSI is inactive despite a small enough cooling time. This may be due the dynamics of the VSI that shows larger wavelengths in the outer region, thus requiring a smaller cooling time, or to boundary effects.

One can also see that the jump in temperature and cooling time, that also defines the boundary between disc and corona, creates a boundary for the VSI, where the surface modes can attach to (Barker & Latter 2015).

6.3. Dust properties

For this simulation we add 20 000 particles per size after 1000 yr. In Fig. 25 we present a histogram of the distribution of particles with a size of 31 cm, after 13 500 yr. We see that in the outer region with the inactive VSI the particles are still Poisson distributed, but in the active region they are caught in the eddies. The particles in the outer region are only collected weakly, since the VSI is reduced, due to the long cooling time. The isothermal case we compare to has clustering throughout the whole disc and the overdensities are stronger by a factor of around two, even though the velocity dispersion is higher by a factor of 5 to 10.

These results show that, even with realistic cooling times, the VSI can create small axisymmetric regions with overdensities in the dust by a factor of three. This is the right range of metallicity and size of particles which is needed for the streaming instability to set in (Youdin & Goodman 2005). This instability can further enhance the clumping until gravity is strong enough to directly form planetesimals out of the cluster of particles.

In Fig. 26 we repeat the statistical analysis for the distribution of particles. We take into account all particles in the region from 15 to 40 au, in the timespan between 11 000 and 13 500 yr over 50 snapshots. We note that the average number of particles per bin is the same as in the isothermal case in the earlier section, since we increased the size of the bins to compensate for the lower density of particles. Again we see a clear deviation from the initial Poisson distribution for the particles with stopping time around unity, even though it is weaker. Interestingly the effect is now most powerful for $\tau_{\rm s} = 6.3 \times 10^{-2}$ (particles with 10 cm radius), where the inward drift velocity for the particles and the inward drift of the vertical motion of the VSI mode is the same, thus the particles move with the bunching gas mode instead of through the mode. Those are only bunched at around 30 au, and are diffused again after they have passed this region.

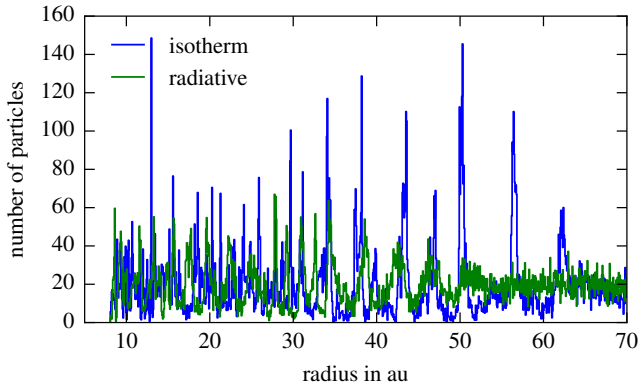

Fig. 25. Histogram of particles with size of 31 cm and stopping time $\tau_s = 0.2$, after 13 500 yr. We divide the radial domain from 8 to 80 au into 1000 bins and count the number of particles in each bin. The average number of particles per bin is 20.0.

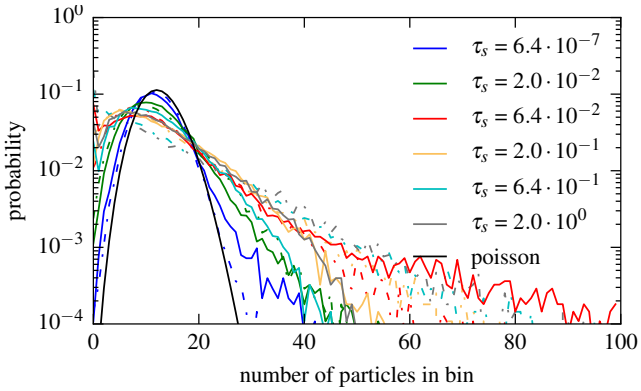

Fig. 26. Probability to find a certain number of particles in a radial bin with $\Delta r = 0.05$ au. The dashed-dotted lines correspond to the isothermal model.

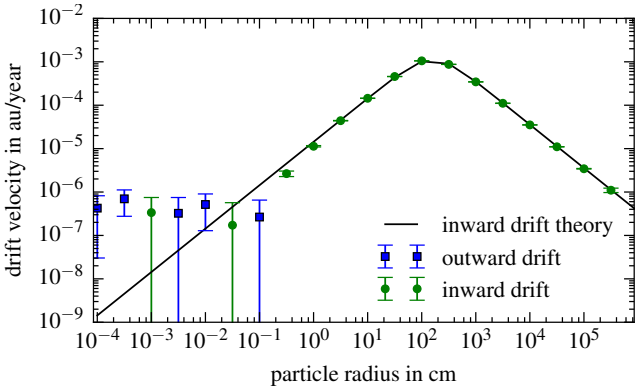

Fig. 27. Drift velocity of the dust particles depending on the radius of the particles. This is compared to expected transport for pressure supported discs. Results are shown for the radiative simulation with irradiation, resolution 1024 × 256 ×64 and viscosity $\nu = 5\times10^{-7}$ at $r = 20$ au. Different colours are used for inward and outward drift. We estimate the error from the radial diffusion coefficient.

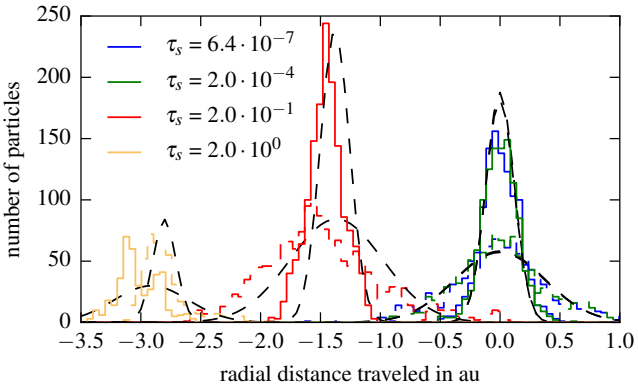

Fig. 28. Radial diffusion after 11 000 yr for 500 yr for the radiative simulation with irradiation and viscosity $\nu = 5\times10^{-7}$. The black dashed lines are calculated from theory for the different stopping times and with the same $\tau_{\rm eddy} = 1.0$ and $\langle u^2_{\rm gas,radial}\rangle = 5\times10^{-8}\cdot u^2_{\rm Kepler,1\ au}$. The isothermal simulation (dashed lines) has a velocity dispersion of $\langle u^2_{\rm gas,radial}\rangle = 5\times10^{-7}\cdot u^2_{\rm Kepler,1\ au}$.

This resonance does not exist in the isothermal case, because the wavelength is greater than in the radiative case. The isothermal case in general behaves very similar to the isothermal case in the earlier section. Both show the strongest bunching for particles with stopping time close to unity.

The radial drift shown in Fig. 27 measured at 20 ± 2 au from 13 500 yr to 18 500 yr is similar to the isothermal case with the same viscosity. While the outward migration is no longer as clear as in the isothermal case with viscosity, there is still a trend to outward migration. That the effect is weaker can be explained by the weaker effect the viscosity has at 20 au.

More important for the radial motion of a single particle is the diffusion. For the radial and vertical velocity dispersion in the region at 20 ± 5 au we measure for the radiative case $\langle u_r^2\rangle = 5\times10^{-8}\cdot u^2_{\rm Kepler,1\ au}$ and $\langle u_z^2\rangle = 5\times10^{-7}\cdot u^2_{\rm Kepler,1\ au}$ and for the isothermal case we measure $\langle u_r^2\rangle = 5\times10^{-7}\cdot u^2_{\rm Kepler,1\ au}$ and $\langle u_z^2\rangle = 2\times10^{-6}\cdot u^2_{\rm Kepler,1\ au}$. Both values lead to a dimensionless eddy time of $\tau_{\rm eddy} = 1.0$ even though the velocity dispersion differs by a factor of ten. The larger difference between prediction and simulation in Fig. 28 results from the error in the measurement of q, the exponent in the radial temperature distribution. Here, $T(r)$ is determined through the radiation transport and q varies now with radius. For the plot we use an average value of $q = -1.1$.

In Table 3 we can see that in this simulation the dust scale height is smaller than the gas scale height even for the smallest particles. We averaged from 13 500 yr to 18 500 yr. In this simulation the radial and vertical calculated eddy lifetimes are again very similar, despite the turbulence not being isotropic.

For the collision statistics we increased the cutoff distance within which we compare particle velocities to 0.2 au to compensate the decreased density of particles. As the distribution of particles already indicated the clustering is indeed weaker. This is reflected additionally in Fig. 30, where we can see that the correlation is slightly weaker. For this radiative case the effect appears to be strongest for a dimensionless stopping time $\tau_s \approx 0.1$ instead of 1 for the isothermal case. The correlation length is larger for the particles with stopping time around one, reflecting the larger wavelength of the VSI in the isothermal case.

The histogram of the relative velocities between particles as displayed in Fig. 29 illustrates this situation. For $\tau_s \approx 0.1$ the particles have about an order of magnitude smaller relative velocities than for large and small values. We can also see that the wider velocity dispersion in the isothermal model leads to greater relative velocities.

Table 3. Measured dust scale heights and inferred eddy lifetimes, from Eq. (14), for the radiative model.

Radius cm	Stopping time τ_s at 20 au	$h_{p,z}$ h_{gas}	$t_{eddy,z}$ at 20 au
1.0×10^{-4}	6.3×10^{-7}	9.4×10^{-1}	–
3.2×10^{-4}	2.0×10^{-6}	9.4×10^{-1}	–
1.0×10^{-3}	6.3×10^{-6}	9.5×10^{-1}	–
3.2×10^{-3}	2.0×10^{-5}	8.0×10^{-1}	1.3×10^{-2}
1.0×10^{-2}	6.3×10^{-5}	8.7×10^{-1}	7.3×10^{-2}
3.2×10^{-2}	2.0×10^{-4}	8.7×10^{-1}	2.4×10^{-1}
1.0×10^{-1}	6.3×10^{-4}	6.6×10^{-1}	1.8×10^{-1}
3.2×10^{-1}	2.0×10^{-3}	5.4×10^{-1}	3.1×10^{-1}
1.0×10^{0}	6.3×10^{-3}	4.2×10^{-1}	5.0×10^{-1}
3.2×10^{0}	2.0×10^{-2}	3.4×10^{-1}	9.9×10^{-1}
1.0×10^{1}	6.3×10^{-2}	2.3×10^{-1}	1.3×10^{0}
3.2×10^{1}	2.0×10^{-1}	8.9×10^{-2}	5.9×10^{-1}
1.0×10^{2}	6.3×10^{-1}	3.1×10^{-2}	2.3×10^{-1}
3.2×10^{2}	2.0×10^{0}	1.5×10^{-2}	1.6×10^{-1}
1.0×10^{3}	6.3×10^{0}	4.1×10^{-3}	3.9×10^{-2}

Notes. We fitted a Gaussian $f(z) = N_0 \exp(-(z \pm \mu)^2/(2r^2 h_p^2)$ to the data of the vertical distribution to find h_p and calculated τ_{eddy} for the irradiated simulation with viscosity of 5×10^{-7}.

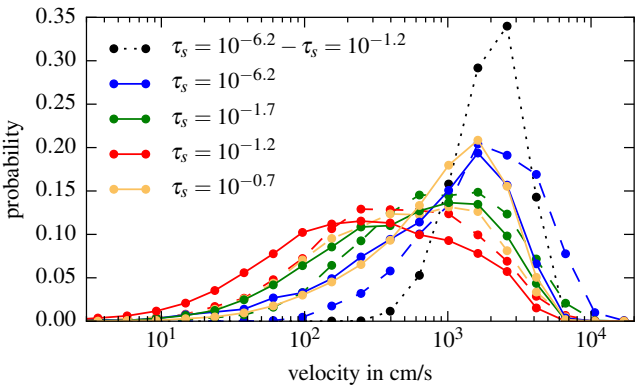

Fig. 29. Relative velocity between particles of the same size for different stopping times after 11 000 yr for the irradiated simulation. The dotted lines correspond to two different particle sizes as indicated in the legend. The dashed lines correspond to the isothermal model. Lines to guide the eye.

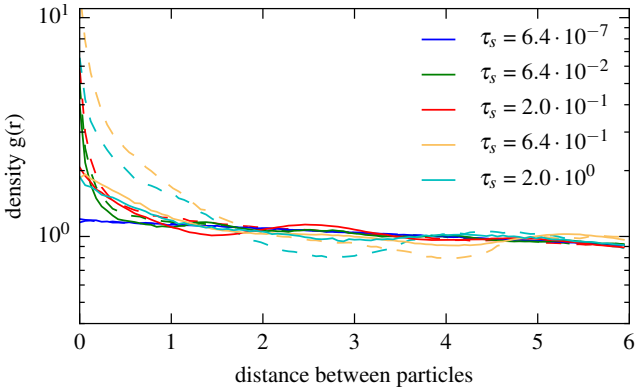

Fig. 30. Pair correlation function for the irradiated simulation: enhancement of surface density in a shell with radius r for different stopping times. Averaged over 5 snapshots in the interval from 11 000 to 13 500 yr. The dashed lines correspond to the isothermal model.

7. Summary and conclusions

In the paper we analysed the dynamics of particles embedded in hydrodynamic discs that show fully developed turbulence as induced by the VSI.

In a first step we calculated isothermal disc models in full three dimensions and analysed the properties of the turbulence generated by the VSI. Our standard model consisted of an eighth of a full circle ($\phi_{max} = \pi/4$) and showed in the fully developed turbulent state α-values around 6×10^{-4}, which is of the same order of magnitude or even slightly larger than the corresponding 2D models (Stoll & Kley 2014). The 3D models shows variations in the azimuthal direction and these fluctuations follow a Kolmogorov-type spectrum. The mean radial velocity of the gas in a VSI turbulent disc turned out to be directed inward in the disc midplane and outward in the upper layers, in agreement with global MHD simulations using zero net vertical magnetic flux (Flock et al. 2011). This flow is opposite to viscous laminar discs (Urpin 1984; Kley & Lin 1992) or MHD discs with non-zero vertical magnetic field (Suzuki & Inutsuka 2014). For 3D discs covering the full circle ($\phi_{max} = 2\pi$) we found very similar results, which allowed us to treat particle evolution in the reduced domain.

In addition to the isothermal case we studied fully radiative models including heating from the central star. To allow for regimes where the VSI instability can operate we extended to radial domain from 8−80 au. The temperature structure in the disc displayed a central disc region with a nearly constant temperature in the vertical direction and hotter surface layers produced by the stellar irradiation. The vertically varying opacity in the disc resulted in different cooling times and the turbulence turned out to be slightly weaker in comparison to the purely isothermal situation. For the effective α-parameter values of around 10^{-4} were reached in the active state that extended from about 10 to 60 au.

After having reached the equilibrium state we inserted particles of different sizes to study their motion in the disc, where the drag force between gaseous disc and particles was treated in the Epstein regime. Overall we found for both, isothermal and radiative discs, comparable results. On average the particles drift inwards with the expected speed. For all disc models we found that the smallest particles show an outwardly directed radial drift. This comes about because the small particles are coupled more to the gas flow and are lifted upward by the vertical motions of the VSI induced large-scale flows. Since the average flow direction in the upper layers is positive small dust particles that are elevated above the disk's midplane are dragged along and move outwards. Particles below about 1 mm in size experience this fate. This outward drift might be beneficial in transporting strongly heated solid material to larger radii as required to explain for example the presence of chondrules at larger radii in the Solar System (Bockelée-Morvan et al. 2002). The upward drift of small particles in the disc by the VSI modes will also help to explain the observed presence of a population small particles in the later stages of the disc evolution that were produced by a fragmentation process (Dullemond & Dominik 2005).

Using the information of histograms, probability functions and pair correlation functions we analysed the spatial re-distribution of particles in the disc that were initially homogeneously distributed. We found that the particles are strongly "bunched" together by the large-scale motions of the VSI turbulence. The bunching effect is strongest for particles with a stopping time of the order unity and the maximum overdensities reached were about 5 times the average initial density of the particles. The relative velocity between particles of the same size is smallest (about a few m/s) for those particles that show the strongest bunching. This combination of high density and low relative speed is highly beneficial for the early formation process of planetary precursors. First, at these relative speeds collisions between two particles can lead to sticking collisions (Blum & Wurm 2008; Meru et al. 2013). The higher relative velocities between particles of different sizes does not necessarily lead to fragmentation. The experiments of Teiser & Wurm (2009) have shown that particles with different size can stick to each other even for collisions up to 50 m/s and possibly more. Secondly, through the concentration of particles it is possible to trigger streaming instabilities in the disc which can further increase the particle concentration and growth (Youdin & Goodman 2005).

The two dimensional distribution of particles in the disc shows axisymmetric ring-like concentration zones of the particles resembling very roughly the features observed recently in the disc around HL Tau (Brogan et al. 2015). Even though the strongest effect is seen here in our simulations for particles about one meter in size, it is possible that through collisions of nearly equal sized bodies much smaller particles that could generate the observed emission can be produced and which follow a similar spatial distribution. Obviously the observed spacing of the "bright" rings in our simulations is smaller than those observed in HL Tau but the inclusion of variations in opacity or chemical abundances may create larger coherent structures.

Acknowledgements. Moritz Stoll received financial support from the Landesgraduiertenförderung of the state of Baden-Württemberg and through the German Research Foundation (DFG) grant KL 650/16. Simulations were performed on the bwGRiD cluster in Tübingen or the ForHLR cluster in Karlsruhe (both funded by the DFG and the Ministry for Science, Research and Arts of the state Baden-Württemberg), and the cluster of the Forschergruppe FOR 759 "The Formation of Planets: The Critical First Growth Phase" funded by the DFG.

References

Arlt, R., & Urpin, V. 2004, A&A, 426, 755
Armitage, P. J. 2011, ARA&A, 49, 195
Bai, X.-N. 2014, ApJ, 791, 137
Bai, X.-N. 2015, ApJ, 798, 84
Bai, X.-N., & Stone, J. M. 2010, ApJS, 190, 297
Balbus, S. A., & Hawley, J. F. 1998, Rev. Mod. Phys., 70, 1
Barker, A. J., & Latter, H. N. 2015, MNRAS, 450, 21
Bitsch, B., Crida, A., Morbidelli, A., Kley, W., & Dobbs-Dixon, I. 2013, A&A, 549, A124
Blum, J., & Wurm, G. 2008, ARA&A, 46, 21
Bockelée-Morvan, D., Gautier, D., Hersant, F., Huré, J.-M., & Robert, F. 2002, A&A, 384, 1107
Brogan, C. L., Pérez, L. M., et al. ALMA Partnership 2015, ApJ, 808, L3
Carballido, A., Bai, X.-N., & Cuzzi, J. N. 2011, MNRAS, 415, 93
Dubrulle, B. 1992, A&A, 266, 592
Dubrulle, B., Morfill, G., & Sterzik, M. 1995, Icarus, 114, 237
Dullemond, C. P., & Dominik, C. 2005, A&A, 434, 971
Epstein, P. S. 1924, Phys. Rev., 23, 710
Flaig, M., Ruoff, P., Kley, W., & Kissmann, R. 2012, MNRAS, 420, 2419
Flock, M., Dzyurkevich, N., Klahr, H., Turner, N. J., & Henning, T. 2011, ApJ, 735, 122
Frank, J., King, A., & Raine, D. J. 2002, Accretion Power in Astrophysics, 3rd edn. (Cambridge University Press)
Fricke, K. 1968, Z. Astrophys., 68, 317
Fromang, S., & Nelson, R. P. 2005, MNRAS, 364, L81
Goldreich, P., & Schubert, G. 1967, ApJ, 150, 571
Gressel, O., Turner, N. J., Nelson, R. P., & McNally, C. P. 2015, ApJ, 801, 84
Johansen, A., & Klahr, H. 2005, ApJ, 634, 1353
Klahr, H. H., & Bodenheimer, P. 2003, ApJ, 582, 869
Kley, W., & Lin, D. N. C. 1992, ApJ, 397, 600
Kolb, S. M., Stute, M., Kley, W., & Mignone, A. 2013, A&A, 559, A80
Lin, M.-K., & Youdin, A. N. 2015, ApJ, 811, 17
Lin, D. N. C., & Pringle, J. E. 1987, MNRAS, 225, 607
Meru, F., Geretshauser, R. J., Schäfer, C., Speith, R., & Kley, W. 2013, MNRAS, 435, 2371
Mignone, A., Bodo, G., Massaglia, S., et al. 2007, ApJS, 170, 228
Nakagawa, Y., Sekiya, M., & Hayashi, C. 1986, Icarus, 67, 375
Nelson, R. P., Gressel, O., & Umurhan, O. M. 2013, MNRAS, 435, 2610
Ruden, S. P., Papaloizou, J. C. B., & Lin, D. N. C. 1988, ApJ, 329, 739
Stoll, M. H. R., & Kley, W. 2014, A&A, 572, A77
Suzuki, T. K., & Inutsuka, S.-I. 2014, ApJ, 784, 121
Takeuchi, T., & Lin, D. N. C. 2002, ApJ, 581, 1344
Teiser, J., & Wurm, G. 2009, MNRAS, 393, 1584
Urpin, V. 2003, A&A, 404, 397
Urpin, V. A. 1984, Sov. Astron., 28, 50
Williams, J. P., & Cieza, L. A. 2011, ARA&A, 49, 67
Youdin, A. N., & Goodman, J. 2005, ApJ, 620, 459
Youdin, A. N., & Lithwick, Y. 2007, Icarus, 192, 588
Zhu, Z., Stone, J. M., Rafikov, R. R., & Bai, X.-N. 2014, ApJ, 785, 122
Zhu, Z., Stone, J. M., & Bai, X.-N. 2015, ApJ, 801, 81

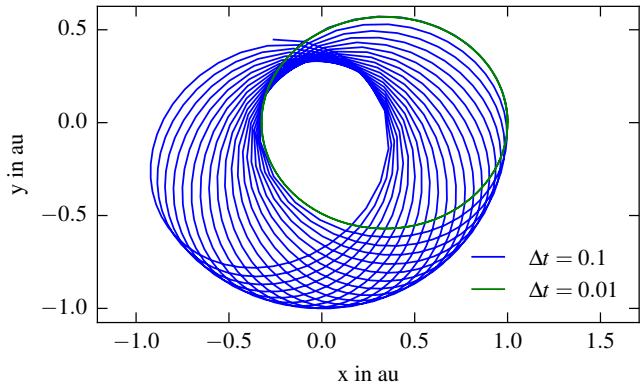

Fig. A.1. Orbital evolution of a test particle on an eccentric orbit.

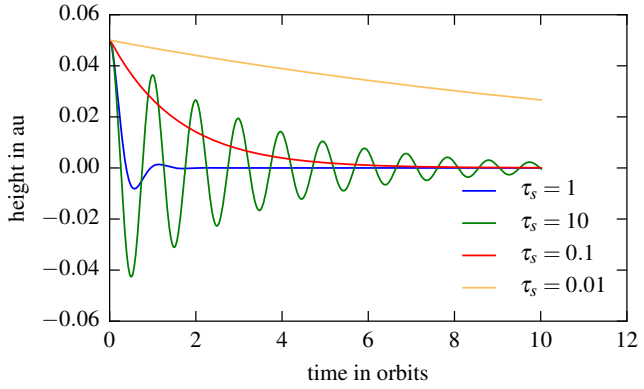

Fig. A.2. Settling of test particles with different stopping times.

Appendix A: Particle solver

To verify the correct implementation of our particle solver we repeat some of the tests of Zhu et al. (2014).

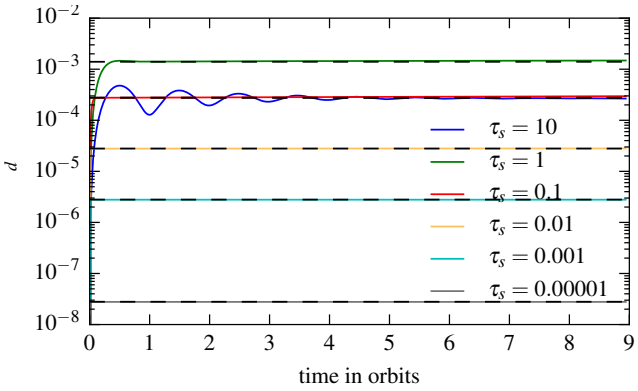

Fig. A.3. Drift velocity for particles with different stopping times.

A.1. Orbit test

We release the particle at $r = 1$, at the midplane with a velocity of $u_\phi = 0.7$ and integrate for 20 orbits. The presented timesteps are $\Delta t = 0.1$ and $\Delta t = 0.01$ for an orbital time of 2π. Even though the orbit precesses for the longer timestep, the geometric property is conserved. There is no visible precession in Fig. A.1 for the timestep of $\Delta t = 0.01$, which we use in our simulations.

A.2. Settling test

We release particles with different stopping times at one scale height from the midplane. For particles with $\tau_s < 1$ we can see in Fig. A.2 the exponential decay of the vertical position. Particles with $\tau_s > 1$ oscillate around the midplane and instead the amplitude decays exponentially.

A.3. Drift test

For the drift test we use the disc in hydrostatic equilibrium and release particles with different stopping times at $r = 5$ au on Keplerian orbits in Fig. A.3. We compare to the theoretical expected drift velocity of Eq. (11) (black line).

A&A 599, L6 (2017)
DOI: 10.1051/0004-6361/201630226

Astronomy & Astrophysics

Letter to the Editor

Anisotropic hydrodynamic turbulence in accretion disks

Moritz H. R. Stoll[1], Wilhelm Kley[1], and Giovanni Picogna[1,2]

[1] Institut für Astronomie und Astrophysik, Universität Tübingen, Auf der Morgenstelle 10, 72076 Tübingen, Germany
e-mail: [moritz.stoll; wilhelm.kley]@uni-tuebingen.de
[2] Universitäts-Sternwarte, Ludwig-Maximilians-Universität München, Scheinerstr. 1, 81679 München, Germany
e-mail: picogna@usm.lmu.de

Received 9 December 2016 / Accepted 1 February 2017

ABSTRACT

Recently, the vertical shear instability (VSI) has become an attractive purely hydrodynamic candidate for the anomalous angular momentum transport required for weakly ionized accretion disks. In direct three-dimensional numerical simulations of VSI turbulence in disks, a meridional circulation pattern was observed that is opposite to the usual viscous flow behavior. Here, we investigate whether this feature can possibly be explained by an anisotropy of the VSI turbulence. Using three-dimensional hydrodynamical simulations, we calculate the turbulent Reynolds stresses relevant for angular momentum transport for a representative section of a disk. We find that the vertical stress is significantly stronger than the radial stress. Using our results in viscous disk simulations with different viscosity coefficients for the radial and vertical direction, we find good agreement with the VSI turbulence for the stresses and meridional flow; this provides additional evidence for the anisotropy. The results are important with respect to the transport of small embedded particles in disks.

Key words. accretion, accretion disks – turbulence

1. Introduction

The exact origin of the driving mechanism of accretion disks is still not fully understood. To accrete matter onto the central object, the matter needs to lose its angular momentum, and because molecular viscosity is by many orders of magnitudes too small to facilitate the required angular transport, it has been suggested that disks are driven by turbulence. The discovery of a linear magneto-rotational instability (MRI) for rotating flows with a negative angular velocity gradient has led to the suggestion that accretion disks are driven by magnetohydrodynamical (MHD) turbulence (Balbus & Hawley 1998). However, the MRI only works efficiently for well-ionized media, for example, in disks around compact objects, but for lower ionization levels the non-ideal MHD effects become stronger and the operability of the MRI questionable. In particular for the cool and low-ionized regions, so-called dead zones with very low turbulent activity have been predicted (Gammie 1996).

Hence, other alternatives are sought for. In the past years the purely hydrodynamical vertical shear instability (VSI) has attracted some attention because the only requirement is a vertical shear in the angular velocity profile, which is in fact a natural consequence of a radial temperature gradient in the disk, for example, induced by irradiation from the central object. Through numerical simulations and linear analysis it has been shown that the VSI operates efficiently for vertically isothermal disks (Nelson et al. 2013) as well as for fully radiative disks that include stellar irradiation (Stoll & Kley 2014). This makes the VSI a promising candidate to bring at least some life back into the dead zones. For many astrophysical applications it is useful to parameterize the turbulence and describe the angular momentum transport by an effective viscous prescription, for example, the well-known ansatz by Shakura & Sunyaev (1973) where the uncertainties of the turbulence are summarized in one constant parameter α (Balbus & Papaloizou 1999). Such an approach using one parameter is applicable for an isotropic turbulence, and useful when the interest is in the overall radial evolution of the disk. To analyze the internal flow field of the disk, which is important for the motion of embedded small particles, it is necessary to take possible non-isotropy effects into account.

Here, we demonstrate that the flow reversal found in recent VSI-turbulent disks (Stoll & Kley 2016) can in fact be traced back to the intrinsic anisotropy of the VSI-turbulence. Using multidimensional hydrodynamical simulations, we calculate the effective radial and vertical transport coefficients and use them in viscous disk simulations.

Table 1. Model parameter: domain size and grid resolution.

Parameter	α-model	VSI
Radial range [5.2 au]	0.4–2.5	0.4–2.5
Vertical range [H]	±4	±5
Phi range [rad]	2D	$0–2\,\pi$
Radial grid size	600	600
Theta grid size	121	128
Phi grid size	2D	1024

2. Model setup

We use the PLUTO code (Mignone et al. 2007) for our simulations, where we model a section of a locally isothermal accretion disk. For the direct turbulent simulations we use a full 3D setup and spherical coordinates (R, θ, ϕ), while for comparison laminar viscous simulations (α-disk), we use a 2D axisymmetric setup and cylindrical coordinates (r, z). The model parameters are given in Table 1. Even though some of the simulations are performed in spherical coordinates, the results are analyzed in cylindrical coordinates. The initial disk is axisymmetric and

extends from 0.4 r_0 to 2.5 r_0, where $r_0 = 5.2$ au. The initial density profile is given by vertical hydrostatic equilibrium

$$\rho(r,z) = \rho_0 \left(\frac{r}{r_0}\right)^p \exp\left[\frac{GM}{c_s^2}\left(\frac{1}{R} - \frac{1}{r}\right)\right], \quad (1)$$

where ρ_0 is the gas mid-plane density at $r = r_0$, and $p = -1.5$. In our locally isothermal approximation the temperature of the disk is a function of the cylindrical radius only,

$$T(r) = T_0 \left(\frac{r}{r_0}\right)^q, \quad (2)$$

where we choose $q = -1$, which causes the disk aspect ratio to be constant and T_0 such that $H/r = h = 0.05$. The pressure is given by $P = c_s^2\rho$, where c_s is the isothermal sound speed with $c_s \propto r^{-1/2}$. The gas moves initially with the angular velocity given by the Keplerian value, corrected by the pressure support (Nelson et al. 2013)

$$\Omega(r,z) = \Omega_K \left[(p+q)\left(\frac{H}{r}\right)^2 + (1+q) - \frac{qr}{\sqrt{r^2+z^2}}\right]^{\frac{1}{2}}, \quad (3)$$

with $\Omega_K^2(r) = GM_*/r^3$, and the meridional flow (u_r, u_z) is set to zero. At the inner and outer boundary we use reflecting boundaries. To increase numerical stability for the turbulent runs, we damp the variables ρ, u_r, u_z to the initial values on a timescale of half a local orbit following the recipe by de Val-Borro et al. (2006), with a damping applied at the inner boundary from 0.4−0.5 r_0 and at the outer boundary from 2.3−2.5 r_0. At the vertical boundaries we use reflective boundaries when the flow is directed inward and zero gradient otherwise. The VSI model is inviscid, and for the α-disk model the kinematic viscosity is given by $\nu = 2/3\alpha c_s H$, with a constant $\alpha = 5 \times 10^{-4}$, which matches the outcome of VSI model.

3. Disk structure

We compare the structure of the VSI unstable disk to viscous disks described by an α-parameter, and study the main differences. The VSI disk is evolved to a quasi-equilibrium state before the analysis is performed. We focus in particular on the flow field and stress tensor, and refer to Nelson et al. (2013) and Stoll & Kley (2014, 2016) for an analysis of the turbulent flow structure.

While the density distributions of the viscous and turbulent disks in equilibrium are very similar due to the necessary pressure equilibrium, there is an important difference in the meridional flow within the disk in particular for the radial velocity. We show the azimuthally averaged radial velocity u_r at $r = r_0$ as a function of the vertical distance for the turbulent and the standard viscous disk in Fig. 1. For the turbulent disk we averaged the velocity in time over 50 orbits and in space around r_0 in the region $(0.8-1.25)r_0$. For better visibility we rescaled the viscous case by a factor of 200. Obviously, the two radial velocity profiles have an opposite behavior. The standard viscous disk using a single (isotropic) value of α shows the typical outflow in the midplane that has been predicted analytically by Urpin (1984) and was later shown in fully time-dependent numerical simulations (Kley & Lin 1992). This behavior of $u_r(z)$ can be derived from the equilibrium angular momentum equation that contains the vertical disk structure (Urpin 1984). In spite of the outwardly directed flow in the midplane, the total vertically integrated mass flow is nevertheless directed inward in case of accreting disks (Kley & Lin 1992).

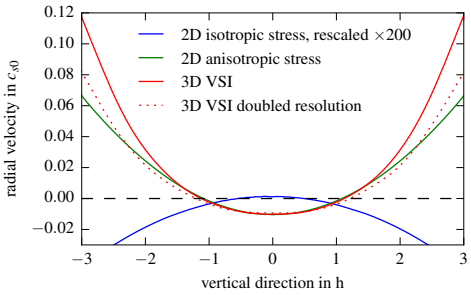

Fig. 1. Radial velocity averaged over 50 orbits. We compare the disk with alpha-viscosity ($\alpha = 5\times10^{-4}$, blue curve) to a disk with active VSI (red curve), a disk with active VSI and doubled resolution (red dotted curve) and a viscous disk with anisotropic stress similar to the VSI disk (green curve, details see Sect. 4). For the turbulent disk the velocity has been azimuthally averaged. The profile shown is in units of sound speed c_{s0} and at $r = r_0$. The viscous case has been rescaled to better visualize the difference.

In contrast, the mean flow field for the turbulent flow (labeled 3D VSI and shown also with a dotted line for a model with double resolution in all directions) is fully reversed; it is not only negative in the midplane and positive in the corona, but also much stronger, as indicated by the different scaling of the curves in Fig. 1. This special feature of the meridional flow field in the VSI case has been found for isothermal as well as radiative disks in Stoll & Kley (2016), but was not analyzed with respect to anisotropic turbulence. From the direct comparison to the viscous case, it is clear that with a standard shear viscosity prescription using a constant α-value or a constant kinematic viscosity, no agreement can be obtained because this will always lead to an inverted parabolic type of profile (Jacquet 2013). This raises the general question whether the VSI turbulence in disks can be described by a standard Navier-Stokes approach to model the angular momentum diffusion. In Sect. 4 we show that we obtain a good match of a fully turbulent and viscous flow for a non-anisotropic turbulent viscosity where the radial and vertical parts enter with a different strength (see curve 2D anisotropic stress), which might be expected for the clearly non-isotropic character of the flow structure in VSI turbulence (Stoll & Kley 2014).

To analyze the effect of the turbulence with respect to angular momentum transport in the disk, it is necessary to calculate the turbulent stresses of the VSI disk. For the overall mass flow in accretion disks, which is driven by outward angular momentum transport, the $r\phi$-component of the Reynolds stress tensor, R, is the most important component because it is generated by the strong shear in the azimuthal velocity. In the case of VSI turbulent disks, it is clear that the vertical dependence of the turbulent stresses ($z\phi$-component) may be of importance as well. Hence, from our simulations we calculate the following turbulent Reynolds stresses

$$R_{i,\phi}(z) = \langle \rho u_i \delta u_\phi \rangle_{t,\phi,r}, \quad (4)$$

where u_i with i in (r,z) denote the radial and vertical flow velocity (u_r, u_z) and δu_ϕ is the deviation of the azimuthal velocity, $u_\phi = r\Omega$, from unperturbed equilibrium, as given by Eq. (3). For the later analysis it is beneficial that the stresses are calculated in cylindrical coordinates (r,z), see Sect. 4. Since we are interested in particular in the vertical dependence of the stresses, $R_{i,\phi}$ is calculated by averaging over the full azimuth (2π), over a small radial range around a reference radius, and over time. Here, we time-average from orbit 80 to orbit 200 using a series of over 60 snap shots and space-average in radius from 0.75−1.35 r_0.

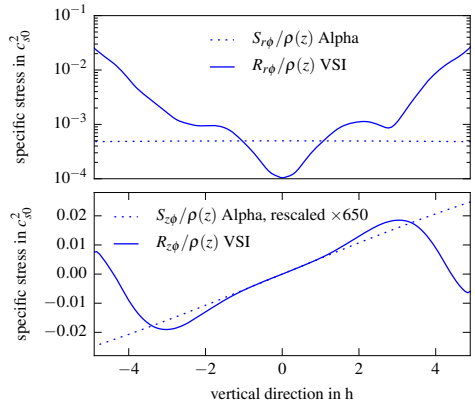

Fig. 2. Specific stress tensor (stress per density) in units of c_{s0}^2. The solid lines represent the Reynolds stress (R) of the VSI simulation and the dotted lines refer to the viscous stress tensor (S) using $\alpha = 5 \times 10^{-4}$. The $S_{z\phi}$ line was rescaled by a factor of 650 to match to the VSI model. The dotted line in the upper panel has a constant value of 5×10^{-4}.

The results of this averaging procedure are shown in Fig. 2. The solid curves refer to the specific stresses $R_{i,\phi}(z)/\rho(r_0, z)$ ($i = r, z$) in units of c_{s0}^2, where $\rho(r_0, z)$ is the equilibrium density distribution, given by Eq. (1), and c_{s0} is the sound speed, both at the reference radius r_0.

We compare it to the viscous shear stress prescription (see Eq. (6) with $\nu = \nu_r = \nu_z$) using $\alpha = 5 \times 10^{-4}$ (dotted lines), which is close to the average of the $r\phi$-component of the specific VSI stress, 4×10^{-4}. We rescaled the $z\phi$-component of the viscous shear stress by a factor of 650 to match the value from the VSI stress. From this large rescaling factor it is immediately clear that $R_{z\phi}$ is far larger than expected from an isotropic viscous shear prescription. We note that the deviation of the vertical $R_{r\phi}/\rho$-profile from the constant $S_{r\phi}/\rho$-profile is not important for our argument, which is why for simplicity we chose a constant α. For the angular momentum transport only the vertical average of this stress component plays a role. In our case, the very large $z\phi$-component of the stress dominates the meridional flow and the influence of $R_{r\phi}$ is small.

4. Anisotropic viscosity of the VSI turbulence

From our numerical studies of the VSI turbulence, in particular the vertical component of the Reynolds stress tensor, we can infer that the turbulence is non-isotropic. Even though we have integrated the hydrodynamical equations using spherical coordinates, we calculated and display $R_{i\phi}$ in cylindrical coordinates because this is simpler to analyze, as we explain in the following. In our approach we investigate whether the turbulent Reynolds stresses, R, can be modeled by a viscous ansatz where R is replaced by the standard viscous stress tensor, S, with an effective turbulent eddy viscosity as introduced by Boussinesq. In cylindrical coordinates the change in angular momentum is given by the following evolution equation:

$$\frac{\partial \rho r^2 \Omega}{\partial t} + \nabla \cdot (\boldsymbol{u} \rho r^2 \Omega) = -\frac{\partial P}{\partial \phi} + \nabla \cdot (r \boldsymbol{S}_\phi). \tag{5}$$

For an axisymmetric flow, that is, when $\partial/\partial\phi$ vanishes, the vector $\boldsymbol{S}_\phi$ (the ϕ-row of the viscous stress tensor) is given by (Tassoul 1978)

$$\boldsymbol{S}_\phi = (S_{r\phi}, S_{z\phi}) = \left(\rho \nu_r r \frac{\partial \Omega}{\partial r}, \rho \nu_z r \frac{\partial \Omega}{\partial z} \right). \tag{6}$$

Axisymmetry is expected for accretion disk flows, and we found this in our simulations. In Eq. (6) we allowed for the option of an anisotropic viscosity by splitting the kinematic viscosity into two components ν_r and ν_z, where ν_r refers to the radial part, which typically is the main contribution in accretion disks in driving the angular momentum transport and mass accretion. The ν_z part connects to the vertical variation of the angular velocity Ω and has commonly been assumed to be on the same order as ν_r. Indeed, using $\nu_z = \nu_r$ and performing viscous axisymmetric, two-dimensional simulations, we find the typical meridional flow field in disks with outflow in the midplane and inflow in upper layers of the disk, as shown in Fig. 1 by the curve labeled "isotropic stress", as found in classic studies (Urpin 1984; Kley & Lin 1992). The outflow in the midplane can easily be derived by an analysis of the radial flow that can be obtained from the angular momentum equation (see also Fromang et al. 2011; Jacquet 2013). From Eq. (5) we find for the equilibrium state that

$$u_r \propto \frac{1}{\rho r^2 \Omega} \left(\frac{1}{r} \frac{\partial (r^2 S_{r\phi})}{\partial r} + \frac{\partial r S_{z\phi}}{\partial z} \right). \tag{7}$$

Expanding Eq. (3) around the midplane (small z), we find

$$\Omega(r, z) = \Omega_K(r) \left(1 + \frac{q}{4} \frac{z^2}{r^2} + \frac{q + p}{2} h^2 \right), \tag{8}$$

where q and p are the exponents in the radial power laws of the density and temperature, respectively, and $h = H/r$ denotes the relative scale height of the disk. Using this relation for $\Omega(r, z)$, we find

$$\frac{\partial \Omega}{\partial z} = \Omega_K \frac{q}{2} \frac{z}{r^2} \tag{9}$$

and then, neglecting terms of order z^2/r^2

$$S_{z\phi} = q \rho \nu_z \frac{\Omega_K}{2} \frac{z}{r} \qquad \text{and} \qquad S_{r\phi} = -\rho \nu_r \frac{3}{2} \Omega_K. \tag{10}$$

Combining this with the $S_{z\phi}$ relation, we find

$$S_{z\phi} = -\frac{q}{3} S_{r\phi} \frac{\nu_z}{\nu_r} \frac{z}{r}. \tag{11}$$

This is plotted in the lower panel in Fig. 2 using $\nu_z = 650 \nu_r$, which demonstrates that the linear dependence of the specific $S_{z\phi}$-stress is a direct consequence of Eq. (11). From Eq. (7) we find for the relation determining the sign of u_r in the midplane the following relation:

$$\begin{aligned} u_r(z = 0) &\propto \left(2 S_{r\phi} + r \frac{\partial S_{r\phi}}{\partial r} + r \frac{\partial S_{z\phi}}{\partial z} \right) \\ &\propto \rho \left[\nu_r \left(-3 - \frac{3}{2} \left(q + p + \frac{3}{2} \right) + \frac{9}{4} \right) + \frac{q}{2} \nu_z \right], \end{aligned} \tag{12}$$

where for the last step we assumed that the viscosity has an α-type behavior with $\nu \sim \alpha c_s^2 / \Omega_K$ and $\rho \propto r^p$ and $c_s^2 \propto r^q$. We note that the direction of flow in the disk midplane can be influenced by the slopes (p, q) in the disk stratification (Fromang et al. 2011; Philippov & Rafikov 2017). From the above relation we find directly that for our disk with slopes $q = -1$ and $p = -3/2$ that

$$u_r(z = 0) \propto \left[\frac{3}{2} \alpha_r - \alpha_z \right]. \tag{13}$$

For isotropic turbulence with $\alpha_r = \alpha_z$ we therefore have outflow in the disk midplane. For the turning point we find that α_z must be larger than $1.5\alpha_r$. Upon increasing α_z over α_r, the midplane radial velocity becomes more and more negative, and the entire vertical flow profile eventually reverses. In our numerical simulations of viscous disks using different values for ν_z we could indeed find the observed flow reversal for moderate values of ν_z/ν_r. By increasing ν_z further, we found that the VSI turbulence can be modeled by an anisotropic eddy viscosity with ν_z over two magnitudes larger than ν_r (650 for our chosen parameter, as shown in Fig. 2).

In performing the comparison simulations, we initially tried to use the same spherical coordinate system that we used for the turbulent VSI simulations by just increasing ν_θ over ν_R in the corresponding components of the stress tensor in spherical coordinates. However, this did not lead to the expected results, in particular, the inversion of the parabola of $u_r(z)$. The results displayed in Fig. 1 were therefore obtained using a cylindrical coordinate system. Because the usage of a spherical coordinate system is beneficial in disk simulations, the equations need to be transformed from r, z to R, θ.

This means we need to transform the viscous part, $\nabla \cdot (r\boldsymbol{S}_\phi)$, to spherical coordinates. The transformation equations are

$$r = R\sin\theta \qquad \text{and} \qquad z = R\cos\theta, \tag{14}$$

and the components of the stress tensor transform according to

$$S_{R\phi} = S_{r\phi}\sin\theta + S_{z\phi}\cos\theta. \tag{15}$$

$$S_{\theta\phi} = S_{r\phi}\cos\theta - S_{z\phi}\sin\theta\cdot \tag{16}$$

The derivatives of Ω transform then as

$$\frac{\partial\Omega}{\partial r} = \sin\theta\frac{\partial\Omega}{\partial R} + \frac{\cos\theta}{R}\frac{\partial\Omega}{\partial\theta} \tag{17}$$

$$\frac{\partial\Omega}{\partial z} = \cos\theta\frac{\partial\Omega}{\partial R} - \frac{\sin\theta}{R}\frac{\partial\Omega}{\partial\theta}. \tag{18}$$

Using Eq. (6) in Eqs. (15) and (16) and substituting this into Eqs. (17) and (18), we obtain for the stress tensor components in spherical coordinates

$$S_{R\phi} = \rho R\sin\theta\left[\left(\nu_r\sin^2\theta + \nu_z\cos^2\theta\right)\frac{\partial\Omega}{\partial R} + (\nu_r - \nu_z)\frac{\cos\theta\sin\theta}{R}\frac{\partial\Omega}{\partial\theta}\right] \tag{19}$$

$$S_{\theta\phi} = \rho R\sin\theta\left[\sin\theta\cos\theta\,(\nu_r - \nu_z)\frac{\partial\Omega}{\partial R} + \left(\nu_r\cos^2\theta + \nu_z\sin^2\theta\right)\frac{1}{R}\frac{\partial\Omega}{\partial\theta}\right]. \tag{20}$$

As can be inferred from these equations, the relatively simple anisotropic relation in cylindrical coordinates leads to complex coupled equations in spherical coordinates with cross terms in the derivatives for Ω. For the isotropic case we can set $\nu_r = \nu_z = \nu$ and obtain the standard relations for the stress tensor components in $R\theta$-coordinates (Tassoul 1978). Now it becomes clear why merely increasing the θ part of the viscosity in $R\theta$-coordinates did not yield the correct answer when compared to the VSI case. Using the full viscosity terms as described in Eqs. (19) and (20) in the numerical simulations yields the correct behavior. However, this comes with a serious drawback because in this case the numerical integration required much smaller time steps for numerical stability than the cylindrical simulation with the same viscosity coefficients. Performing multidimensional simulations of viscous disks mimicking the non-isotropic behavior of the VSI turbulence in $R\theta$-coordinates therefore requires a considerable numerical effort. One solution to this problem may be the usage of an implicit solver for the viscous terms.

5. Conclusions

From direct three-dimensional simulations of locally isothermal accretion disks we observed that the eddies introduced by the VSI generate stresses that are strongly anisotropic. Specifically, we found that the vertical $z\phi$-component of the Reynolds stress is enhanced by a factor of 650 over the standard $r\phi$-part. By performing viscous disk simulations using a non-isotropic viscosity with α_z highly enlarged over α_r, we could obtain the same flow reversal as seen in the VSI disk, which verifies the non-isotropy of the viscosity. Hence, the reversal of the radial flow profile compared to the usual α-model is a clear consequence of the anisotropy. This will have an effect on the dust migration processes (Stoll & Kley 2016) that need to be contrasted to the outward drift in the midplane viscous models (Takeuchi & Lin 2002). From this we can conclude that we need to be careful with turbulence models imposed on accretions disks when we adopt viscous models to describe them.

The meridional circulation of MRI-turbulent disks has been analyzed by Fromang et al. (2011), who found a similar mean flow dynamics in the disk but did not attribute it to a non-isotropic turbulence (with large $S_{z\phi}$) but rather to a radial variation in the magnitude of the viscosity. However, their turbulent $R_{z\phi}$ profile (in Fig. 5) indicates that it may be enhanced over the standard viscous value as well, which could also be a reason for the flow reversal.

Even though the analysis is performed for simplicity for a locally isothermal disk, our results are quite general as simulations for fully radiative disks show the same behavior although they have different radial and vertical temperature profiles. For this purpose, we reanalyzed our radiative simulations in Stoll & Kley (2016) and found a similar anisotropy. Concerning numerical resolution, simulations with double resolution show the same results as shown in Fig. 1. Nevertheless, further exploration needs to be done in order to check how the anisotropy factor varies for different disk parameters and to explore the possibility of anisotropic stresses in MRI models.

Acknowledgements. Moritz Stoll received financial support from the Landesgraduiertenförderung of the state of Baden-Württemberg and through the German Research Foundation (DFG) grant KL 650/16. G. Picogna acknowledges the support through DFG-grant KL 650/21 within the collaborative research program "The first 10 Million Years of the Solar System". Some simulations were performed on the bwGRiD cluster in Tübingen, funded by the state of Baden-Württemberg and the DFG. We thank Roman Rafikov for providing us with a preprint and very useful discussions.

References

Balbus, S. A., & Hawley, J. F. 1998, Rev. Mod. Phys., 70, 1
Balbus, S. A., & Papaloizou, J. C. B. 1999, ApJ, 521, 650
de Val-Borro, M., Edgar, R. G., Artymowicz, P., et al. 2006, MNRAS, 370, 529
Fromang, S., Lyra, W., & Masset, F. 2011, A&A, 534, A107
Gammie, C. F. 1996, ApJ, 457, 355
Jacquet, E. 2013, A&A, 551, A75
Kley, W., & Lin, D. N. C. 1992, ApJ, 397, 600
Mignone, A., Bodo, G., Massaglia, S., et al. 2007, ApJS, 170, 228
Nelson, R. P., Gressel, O., & Umurhan, O. M. 2013, MNRAS, 435, 2610
Philippov, A. A., & Rafikov, R. R. 2017, ApJ, submitted [arXiv:1701.01912]
Shakura, N. I., & Sunyaev, R. A. 1973, A&A, 24, 337
Stoll, M. H. R., & Kley, W. 2014, A&A, 572, A77
Stoll, M. H. R., & Kley, W. 2016, A&A, 594, A57
Takeuchi, T., & Lin, D. N. C. 2002, ApJ, 581, 1344
Tassoul, J.-L. 1978, Theory of rotating stars (Princeton: University Press)
Urpin, V. A. 1984, Sov. Astron., 28, 50

Astronomy & Astrophysics manuscript no. vsi-planet
February 21, 2017

Planet-disc interaction in laminar and turbulent discs

Moritz H. R. Stoll[1], Giovanni Picogna[1,2], and Wilhelm Kley[1]

[1] Institut für Astronomie und Astrophysik, Universität Tübingen, Auf der Morgenstelle 10, D-72076 Tübingen, Germany
e-mail: {moritz.stoll@, wilhelm.kley@}uni-tuebingen.de
[2] Universitäts-Sternwarte, Ludwig-Maximilians-Universität München, Scheinerstr. 1, D-81679 München, Germany
e-mail: picogna@usm.lmu.de

Received February 21, 2017/ Accepted later

ABSTRACT

In weakly ionized discs turbulence can be generated through the vertical shear instability (VSI). Embedded planets feel a stochastic component in the torques acting on them which can impact their migration. In this work we study the interplay between a growing planet embedded in a protoplanetary disc and the VSI. We performed a series of three-dimensional hydrodynamical simulations for inviscid locally isothermal discs that are VSI unstable and corresponding viscous discs having the same effective viscosity with embedded planets in the mass range from 5 to 100 Earth masses.
The inviscid discs become turbulent and generate angular momentum transport with an effective $\alpha = 5 \cdot 10^{-4}$. For all planet masses we find that the planets have only a weak impact on the disc turbulence. For the largest planet ($100 M_\oplus$) the turbulent activity becomes even enhanced inside of the planet. The depth and width of a gap created by the more massive planets (30, 100 $M_\oplus$) in turbulent discs equal exactly that in the viscous disc, leading to very similar torque strengths acting on the planet, with small stochastic fluctuations for the VSI disc. At the gap edges vortices are generated that are stronger and longer lived in the VSI disc. Low mass planets (with $M_p \leq 10 M_\oplus$) do not open gaps in the disc but create an over-density behind the planet that exerts a significant negative torque. This can boost the inward migration well above the Type I rate. Due to the finite turbulence level in realistic three-dimensional discs the gap depth will always be limited and migration will not stall in inviscid discs.

Key words. accretion discs, turbulence, planets

1. Introduction

The longstanding problem of identifying the mechanism responsible for transporting angular momentum in accretion discs and explain their observed lifetimes has been tackled since the early works of Shakura & Sunyaev (1973) and Lynden-Bell & Pringle (1974). The physical process that has been identified having the major contribution is the magnetorotational instability (MRI) (Balbus & Hawley 1991; Hawley & Balbus 1991). However, especially within the context of planet formation, the basic condition of an ionised media to trigger the MRI is generally not fulfilled (Gammie 1996).

Several purely hydrodynamical mechanisms have been proposed to drive the angular momentum, even in the non-ionised regions of the disc (also referred to as "dead zones"), that under special conditions can develop (see e.g. Nelson et al. 2013, and references therein). One of the more general applicable of those mechanisms is the vertical shear instability (VSI) which was first discovered in the context of differentially rotating stars (Goldreich & Schubert 1967; Fricke 1968) and then later applied also to accretion discs (Urpin & Brandenburg 1998). More recently, the VSI has been modelled and proven effective both in globally and locally isothermal discs (Arlt & Urpin 2004; Nelson et al. 2013), and in fully radiative discs (Stoll & Kley 2014).

Within the context of the planet formation process, these instabilities can strongly shape the dust dynamics, by increasing its concentration inside vortices (Barge & Sommeria 1995; Klahr & Bodenheimer 2006; Baruteau & Zhu 2016), and regulating their settling and growth (Dullemond & Dominik 2005). In particular, Stoll & Kley (2016) studied the effect of the VSI on the dust dynamics, finding a strong clustering of dust by the large-scale vertical motion induced by the instability and a reduced relative speed which can be highly beneficial for the planet formation process. Furthermore, a strong outward migration of submm size dust is observed in the upper layers of the disc that can replenish the outer disc regions of solid material.

A planet can strongly affect the disc structure in its vicinity by creating density waves departing from its location and depleting the co-orbital region. These asymmetries in the disc are then generating a torque acting onto the planet and force it to migrate within the disc (see e.g. Kley & Nelson 2012, and references therein). The direction and magnitude of this migration depends strongly on the local properties of the disc. The VSI generates strong vertical motions that can perturb the disc equilibrium, potentially affecting the resulting torque acting onto the planet.

In this work we focus on the signatures induced by a planet onto a protoplanetary disc where the VSI is operating in an inviscid disc and the resulting torque acting on it, and compare it to the classical viscous α model in order to study the main differences that this simpler prescription can or cannot reproduce. The paper is organised as follows. In Sec. 2 we describe the numerical method used to model the disc and planet and the parameter space studied. In Sec. 3 we outline the results of our analysis, and in Sec. 4 we discuss the major points and draw the conclusions.

2. Setup

We used the PLUTO code (Mignone et al. 2007) to model an isothermal accretion disc in spherical coordinates (r, θ, ϕ) and compared the interaction of an embedded planet with its parent

Table 1. Model parameter

Parameter	model
Radial range [5.2 au]	0.4 - 2.5
Vertical range [H]	±5
Phi range [rad]	0 - 2 π
Radial grid size	600
Theta grid size	128
Phi grid size	1024
Planet mass [$M_\oplus$]	5, 10, 30, 100

disc for a VSI model, which is inviscid and relies on the turbulence generated by the instability for the angular momentum transport, and an alpha disc model. The main parameters of the reference simulations are summarised in Tab. 1.

2.1. Gas component

The initial disc is axisymmetric and extends from 0.4 r_p to 2.5 r_p, where $r_p = 5.2$ au is the planet position. We state the initial conditions in cylindrical coordinates (R,Z,ϕ). The initial density profile created by force equilibrium is given by

$$\rho(R,Z) = \rho_0 \left(\frac{R}{R_p}\right)^p \exp\left[\frac{GM_s}{c_s^2}\left(\frac{1}{r}-\frac{1}{R}\right)\right], \quad (1)$$

where ρ_0 is the gas mid-plane density at $R = R_p = r_p$, $p = -1.5$ the density exponent, and c_s the isothermal sound speed. The disc is modelled with a locally isothermal equation of state, which keeps the initial temperature stratification fixed throughout the whole simulation. We assume a constant aspect ratio $H/r = 0.05$, which corresponds to a temperature profile

$$T(R) = T_0 \left(\frac{R}{R_p}\right)^q , \quad (2)$$

with $q = -1$ and $T_0 = 121$ K.

The gas moves with an azimuthal velocity given by the Keplerian speed around a 1 $M_\odot$ star, corrected by the pressure support (Nelson et al. 2013):

$$\Omega(R,Z) = \Omega_K \left[(p+q)\left(\frac{H}{R}\right)^2 + (1+q) - \frac{qR}{\sqrt{R^2+Z^2}}\right]^{\frac{1}{2}} . \quad (3)$$

At the inner and outer boundary we damp the density, radial and vertical velocity to the initial values at the timescale of half a local orbit (see e.g. de Val-Borro et al. 2006), to reduce numerical issues due to the interaction of the VSI with the boundary and to prevent reflection of the spiral wave onto the boundary. The damping is applied in the intervals [0.4,0.5]r_p and [2.3,2.5]r_p. For the kinematic viscosity in the alpha disc model we use $\nu = 2/3\alpha c_s H$, and adopt a constant α parameter of $\alpha = 5 \cdot 10^{-4}$, which is close to the value obtained from the VSI model (see Fig. 1). To bring the VSI model into equilibrium, we evolve it for 200 orbits before embedding the planet.

2.2. The planet

We embed a planet that orbits its parent star on a circular orbit with a radius $r_p = 1$ and a mass in the range [5, 10, 30, 100]$M_\oplus$. Gas accretion is not allowed, and the planet does not feel the disc, so its orbital parameters remain fixed during the whole simulation. The gravitational potential exerted by the planet onto the surrounding gas is implemented with a cubic expansion in the vicinity of the planet location (Klahr & Kley 2006):

$$\Phi_p = \begin{cases} -\frac{GM_p}{d}\left[\left(\frac{d}{d_{rsm}}\right)^4 - 2\left(\frac{d}{d_{rsm}}\right)^3 + 2\left(\frac{d}{d_{rsm}}\right)\right], & \text{for } d < d_{rsm} \\ -\frac{GM_p}{d}, & \text{for } d \geq d_{rsm}, \end{cases} \quad (4)$$

where d is the distance of a gas element from the planet location, and the smoothing length $d_{rsm} = 0.5\, r_{Hill}$ is adopted in order to avoid singularities. To prevent strong shock waves in the initial phase of the simulations, the planetary mass is increased slowly over the first 20 orbits of the simulation. We run the simulations for 200 orbital periods of the planet.

3. Results

3.1. The effective viscosity of the disc with embedded planets

For the VSI models the alpha-parameter is not set by the viscosity prescription. Instead, the VSI generates eddies that transport the angular momentum self-consistently. We can then calculate the efficiency of this process by evaluating an alpha-parameter through the Reynolds stress resulting from the turbulence.

We calculate the Reynolds stress in cylindrical coordinates (R, Z, ϕ):

$$R_{R,\phi} = \rho u_R \delta u_\phi , \quad (5)$$

where δu_ϕ is the local difference from the equilibrium azimuthal velocity, which we calculate by time averaging u_ϕ for each grid cell from orbit 60 to orbit 200 over 70 snap shots.

We then can calculate the dimensionless alpha-parameter as function of the radius

$$\alpha(r) = \frac{\langle R_{R,\phi}\rangle_{t,\theta,\phi}}{\langle P\rangle_{t,\theta,\phi}} , \quad (6)$$

where P is the pressure and $\langle\rangle_{t,\theta,\phi}$ denotes the average over time (140 orbits) and the whole vertical and azimuthal domain.

In Fig. 1 we compare the alpha-parameter for the different VSI-active discs with embedded planets of different mass. The inner damping region from 0.4 r_p to 0.5 r_p is very effective in suppressing the VSI, which is intended to reduce the interaction with the boundary. The wave killing zone is slightly less effective in suppressing the VSI for an increased grid resolution close to the inner boundary (for the 10 $M_\oplus$ model), while there is no difference in the outer disc. Interestingly, the VSI is more resilient to the wave killing zone for the 100 $M_\oplus$ case. There the VSI is stronger and can access a region much closer to the inner boundary. This behaviour is also highlighted in Fig. 2, where the vertical velocity in the midplane of the disc (induced by the VSI) reaches $0.5 c_{s0}$ for the more massive case.

In the top panels of Fig. 2 we see that small planetary masses are not able to influence the strength of the VSI, even close to their location. The strong deviation in the alpha profile seen in Fig. 1 for the large mass planets can be directly linked in the bottom panels of Fig. 2 with the formation of strong vortices at the gap edges carved by the planets. The vortex at the outer edge is strong enough to suppress the VSI in the region [1.2, 2.0]r_p. For the 30 $M_\oplus$ case, the variation of the surface density profile is enough to reduce the effectiveness of the VSI in close proximity to the planet.

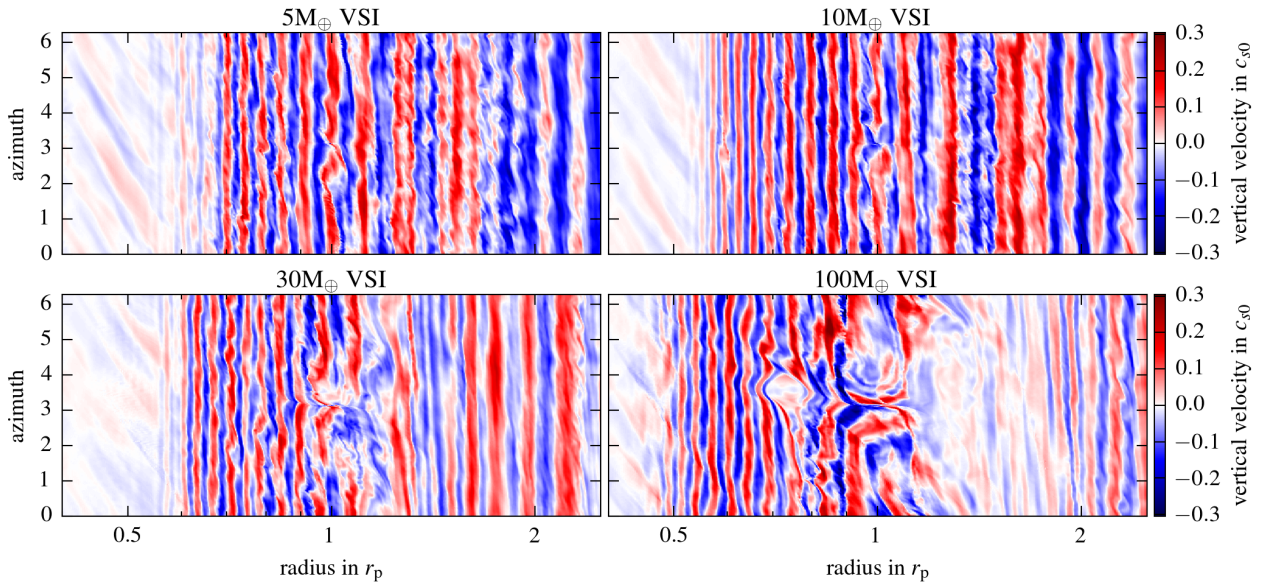

Fig. 2. Vertical velocity in the midplane of the VSI-disc after 198 orbits with embedded planets of different mass. Red colour denotes an upward motion and blue downwards. Larger planets clearly disrupt the usual VSI-modes close to the planet. In the last panel (100 $M_\oplus$ planet) vortices are visible at both sides of the planet. Also visible in the last panel is the more extended VSI activity near to the inner boundary than in the other panels.

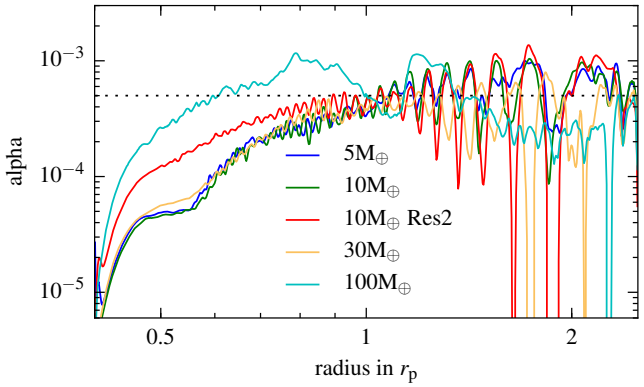

Fig. 1. Comparison of the alpha-parameter for the different VSI-active simulations with embedded planets of different mass. The planet is located at $r = r_p$. 'Res2' indicates a model with double resolution. The dotted line is at $\alpha = 5 \cdot 10^{-4}$.

Finally in the outer region, beginning at $2\,r_p$, the VSI can form unaffected by the planet and leads to an alpha-parameter close to 10^{-3}, which is approximately the value inferred from observations (see e.g. Andrews et al. 2009). Only for the largest planet the VSI is slightly suppressed due to the formation of a large vortex outside of the planetary orbit.

Altogether we can see that in this simulations α rises with radius, contrary to our previous results (Stoll & Kley 2014; Stoll & Kley 2016) where this trend was not observed, but there we also had a steeper radial density profile with $p = -2.5$.

3.2. Vortices and vorticity

Vortex creation by embedded planets is a phenomenon occurring in nearly inviscid discs (Koller et al. 2003; de Val-Borro et al. 2007), while they are usually suppressed by viscosity over time (de Val-Borro et al. 2006). It is thus unclear what happens in VSI simulations that are able to generate a viscosity on the order of $\alpha = 5 \cdot 10^{-4}$. In fact, in the simulations with VSI and $M_p = 100\,M_\oplus$ we see multiple vortices developing at the outer edge of the gap after the slow introduction of the planet (over 20 orbits). They merge to a single vortex over the next 100 orbits, which then remains stable, and even increases slightly in strength up to the end of the simulation. This vortex, at nearly the end of the simulation,[1] is shown in Fig. 3 on the right side of the lower panels. There we can see not only a vortex at the outer edge, but also a smaller vortex which has formed at the inner edge of the gap. Both vortices exists over the whole simulated timescale of 200 orbits. This is in contrast with the alpha disc on the left side of the lower panel, where we can still see two weak vortices that are dissipating in the long run due to the effect of viscosity.

Now we compare directly the inviscid VSI-active simulations with the results of a viscous disc using $\alpha = 5 \cdot 10^{-4}$. The upper panel of Fig. 3 shows the simulations with $M_p = 30\,M_\oplus$. As expected, the alpha viscosity disc does not show large scale vortices, but the VSI simulations again introduces a smaller vortex, which is also stable over the runtime of the simulation. The runs with smaller planets do not have a gap and thus do not show large scale vortices in this region, but instead smaller vortices are visible.

To further analyse the vortices we calculate a normalised vorticity:

$$\overline{\omega}_\theta = \left(\frac{r}{r_p}\right)^{3/2} (\nabla \times \boldsymbol{u})_\theta \,. \tag{7}$$

For undisturbed Kepler rotation this leads to $\overline{\omega}_\theta = \omega_{\theta K}$ independent of radius, where $\omega_{\theta K}$ is the vorticity at $r = r_p$.

The normalised vorticity in the disc's miplane is displayed in Fig. 4 for various models. The first row shows the vorticity of the two low mass planets averaged in time over 50 snapshots, beginning with orbit 100 and ending with orbit 200. We can see that

[1] At 200 orbits the vortex sits at the periodic boundary, thus we show one earlier time slice, where it is in the middle of the domain.

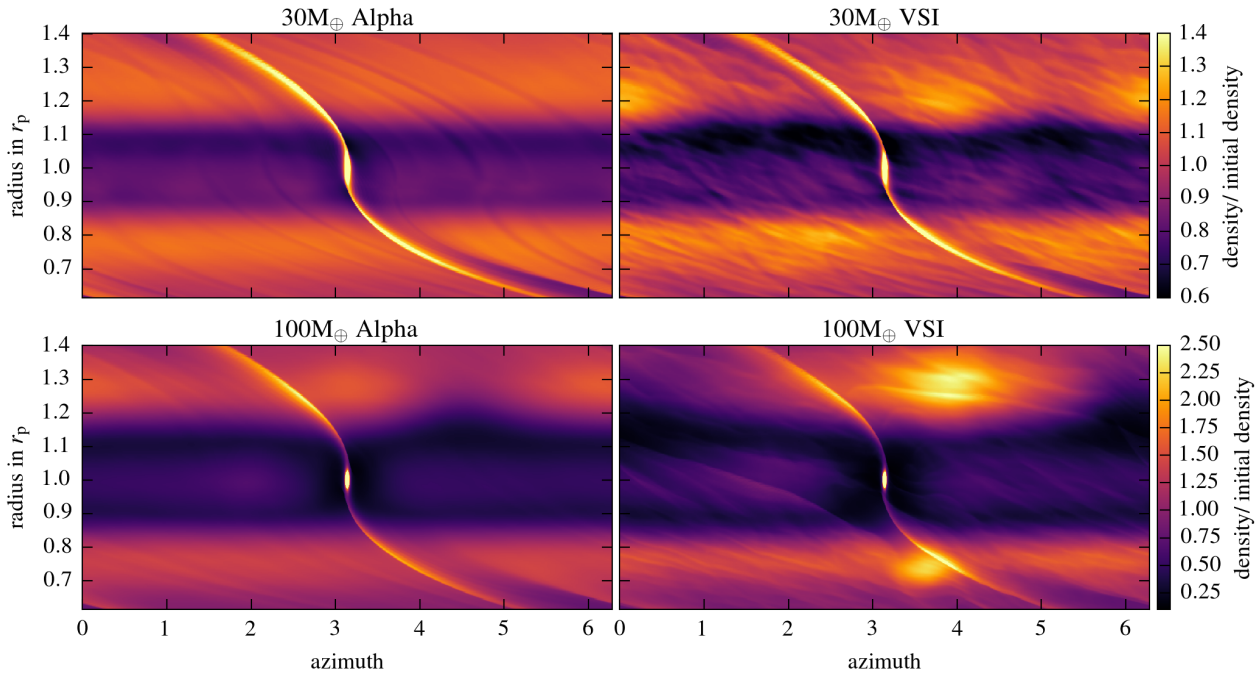

Fig. 3. Density in the midplane relative to the initial density after 198 orbits for the inviscid VSI-active simulations and viscous disc models using $\alpha = 5 \cdot 10^{-4}$. **Upper Panels**: after 198 orbits for $M_p = 30\,M_\oplus$. **Lower Panels**: same for $M_p = 100\,M_\oplus$.

the VSI does transport the vorticity created close to the planet along the horseshoe orbits, which leads to an increase in the surface density along the inner horseshoe orbit. This also creates a small vortex in close proximity behind the planet (for the $5\,M_\oplus$ model in top left panel), which affects the torques as we will see in Sec. 3.4.

The second to third row show the normalised vorticity for the different planets in the VSI discs after 200 orbits. The development of small vortices in the region with VSI was already seen and explained by Richard et al. (2016). The vortices in the $100\,M_\oplus$ model, which were already visible in Fig. 3, are clearly identifiable as an increase in the vorticity. The vortex at the inner edge forms after 100 orbits at $0.8\,r_p$ and starts to migrate inwards. The migration is initially slow, but it increases after leaving the gap edge. After further 100 orbits it migrates with approximately $0.001 r_p$ per orbit to $0.73\,r_p$ where it can be seen in the figure, which is on the same order of magnitude as found by (Richard et al. 2013). Vortex migration has already been studied by Paardekooper et al. (2010) and is due to the angular momentum transport by the excited density waves. The waves are asymmetric due to the density and vorticity gradient, leading to a net transport and migration. The vortex at the outer edge does not migrate notably, because the presence of the planet prevents inward migration.

The $30\,M_\oplus$ model has also increased vorticity at the edges of the gap. While no large vortices have formed yet, at the outer edge of the gap two vortices are forming (see also Fig. 3). This is in contrast to the alpha disc simulations, where for the $30\,M_\oplus$ case no vortices are seen and only weak signatures can be noticed for the $100\,M_\oplus$ case. The last row shows the vorticity for the alpha disc, where small vortices are present in the horseshoe region for the $30\,M_\oplus$ model, since the relatively small viscosity cannot dissipate them on a short timescale. The variation in vorticity in the outer region is due to VSI activity, which is not suppressed completely by the viscosity leaving mainly the modes with small wavenumber. Similar to the VSI disc, we see stronger VSI activity in the alpha disc in the $100\,M_\oplus$ model both in the inner and outer disc.

3.3. Surface density profile

An important observable that can be studied is the surface density profile which, modified by the presence of the planet and local instabilities, can show specific recognisable patterns. We present in Fig. 5 the disc surface density distribution, with respect to the initial model, for the different models and planetary masses, averaged over the azimuthal direction.

In the VSI-discs the planet is able to carve slightly deeper gaps with respect to the alpha disc models. Moreover, the profile is increased at the inner gap edge. These effects are caused by an increased vorticity at the gap edges, due to the interplay of the VSI with the Rossby wave instability (see Richard et al. 2016). Surprisingly even the smaller planets create a perturbation in the surface density profile close to the planet (especially in the VSI models). This is not a typical gap, but instead an increase in the surface density profile close the planet at the inner side of the disc and a decrease at the outer side. This comes from an increased vorticity in this region as we discussed in more detail in the Sec. 3.2. Finally, an overall slight decrease in the surface density in the outer region is visible for all VSI models, caused in part because they have been evolved for 200 orbits before adding the planet, and also due to higher alpha-parameter in the outer region (see Fig. 1). For the larger planets the surface density profiles show very good agreement between the VSI models and the corresponding viscous α-disc models. The gaps have the same widths and depths, confirming the estimate for the effective viscosity, $\alpha = 5 \cdot 10^{-4}$.

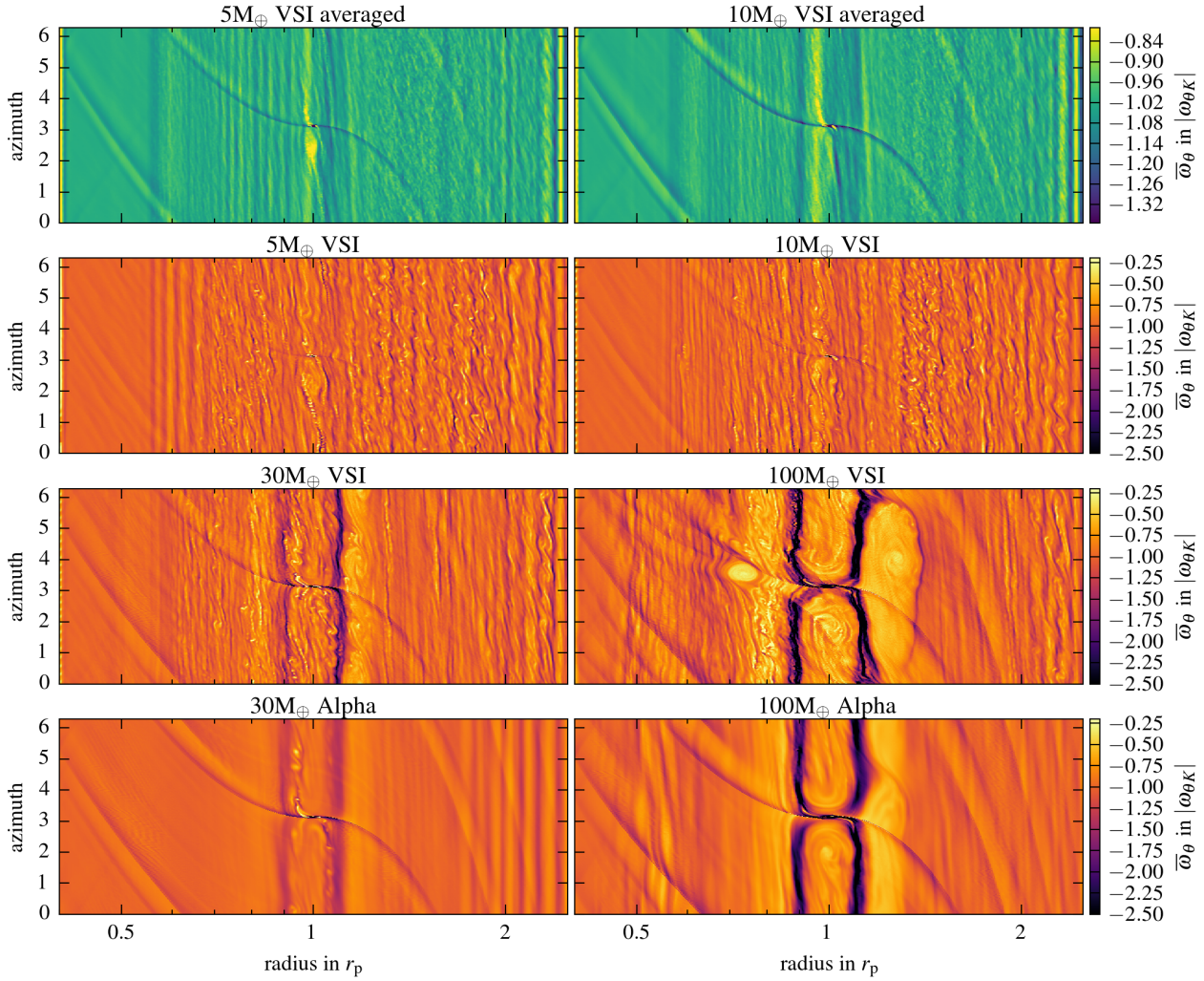

Fig. 4. First Row: Normalised vorticity in the midplane averaged over the last 100 orbits in the VSI disc. The increased vorticity close to the planet is clearly visible. **Second to Third Row**: Normalised vorticity in the midplane for the VSI disc after 198 orbits. **Last Row**: Normalised vorticity in the midplane for the viscous alpha disc after 198 orbits.

3.4. Torques acting on the planet

We calculate the torques using a smoothed force of the planet onto the disc:

$$\boldsymbol{F}_\mathrm{p} = \frac{GM_\mathrm{p}\Delta m}{d^3 + (\varepsilon R_H)^3}\boldsymbol{d}\,, \tag{8}$$

where d is the distance of a grid cell with mass Δm from the planet and $\varepsilon = 0.5$ the smoothing length. The smoothing reduces the potential inside the Hill radius, where we get too large contributions otherwise from the high gas density due to the missing accretion of the gas onto the planet. Moreover the density distribution close to the planet should be symmetrical with respect to the planet and thus it should not contribute to the total torque, but the finite resolution can make this numerically challenging.

We compare our results to the simulations of D'Angelo & Lubow (2010), thus we use the same normalization for the total torques

$$\Gamma_0 = \Sigma(r_\mathrm{p})\Omega^2(r_\mathrm{p})r_\mathrm{p}^4\left(\frac{M_\mathrm{p}}{M_s}\right)^2\left(\frac{r_\mathrm{p}}{H}\right)^2\,, \tag{9}$$

and for the torque distribution per unit disc mass as a function of radius

$$\left(\frac{d\Gamma}{dm}\right)_0 = \Omega^2(r_\mathrm{p})r_\mathrm{p}^2\left(\frac{M_\mathrm{p}}{M_s}\right)^2\left(\frac{r_\mathrm{p}}{H}\right)^4\,. \tag{10}$$

We display the torques over time in Fig. 6, where we express the total torque averaged over the last 50 orbits in the legend. We smoothed the torques over 4 orbits with a Gaussian window, to reduce the strong fluctuations. The source of the perturbations are different depending on the size of the planet. For the smaller planets they are introduced through the turbulence injected by the VSI. In the case of the massive planet the oscillations are introduced by a vortex at the outer edge of the planet.

We compare the torques to the simulations of D'Angelo & Lubow (2010), who obtained for locally isothermal 3D discs the following empirical function:

$$\Gamma = -(1.36 + 0.62\beta + 0.43\zeta)\Gamma_0\,, \tag{11}$$

where $\beta = -d\ln\Sigma/d\ln r$ and $\zeta = -d\ln T/d\ln r$, which correspond for our simulations to $\beta = 0.5$, $\zeta = 1$, and leads to an expected torque of $\Gamma = -2.15\Gamma_0$.

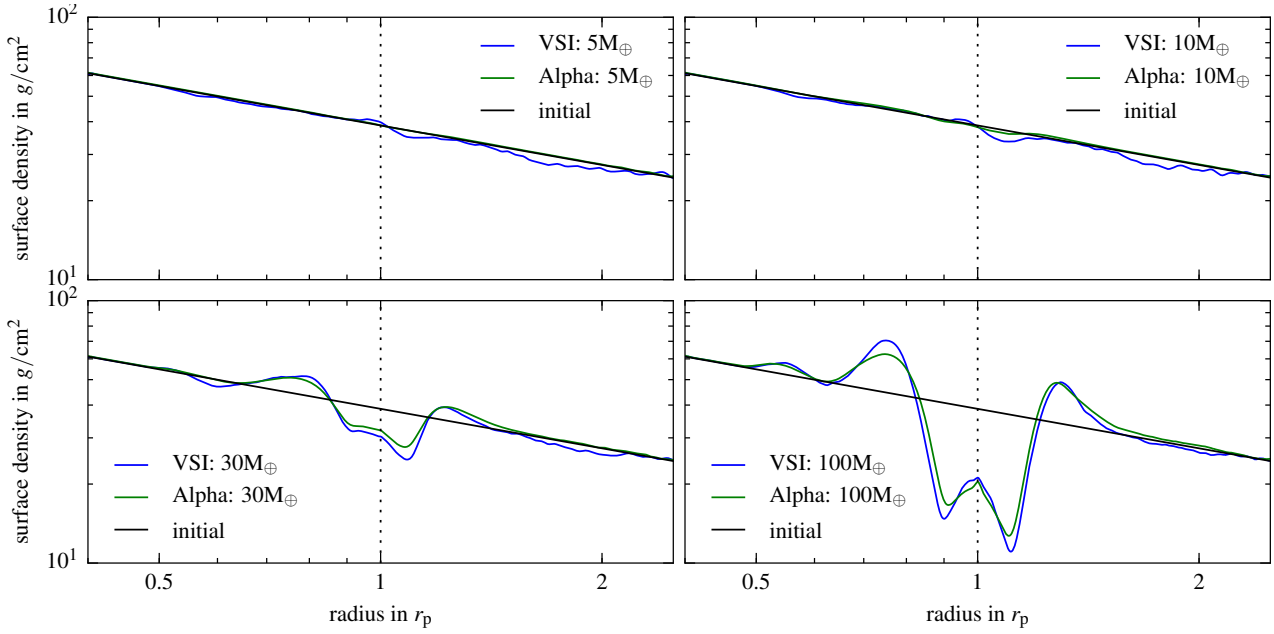

Fig. 5. Surface density for the different simulations after 200 orbits. The vertical dotted black lines indicate the position of the planet and the initial surface density profile is marked by the solid black line. For each planet mass the VSI models are compared to the α-disc cases.

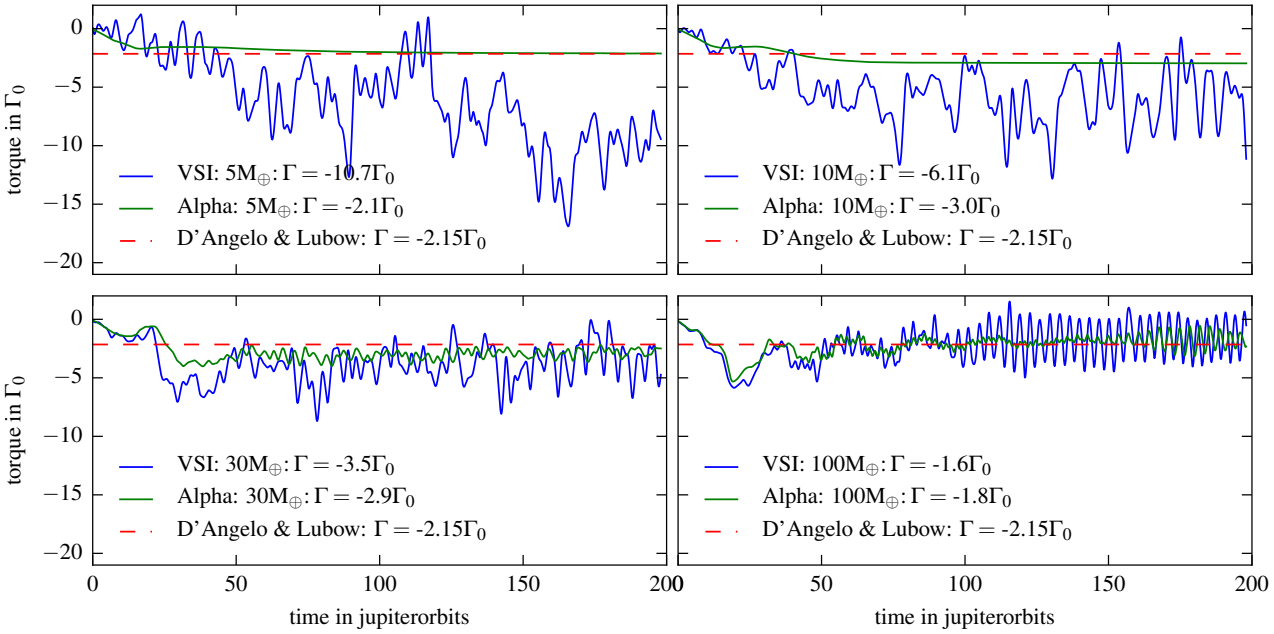

Fig. 6. Torque over time normalised by Γ_0. We smooth over 4 orbits with a Gaussian window and compare to the simulation of D'Angelo & Lubow (2010) (red dashed line). In the legend we give the total torque averaged over the last 50 orbits. Due to the turbulence in the VSI disc the torque strongly fluctuates. The oscillations in the last panel are due to the presence of a vortex.

Our discs with alpha-viscosity have a close agreement with the empirical function, with small differences caused by the different smoothing methods of the planetary potential adopted. Only the 100 $M_\oplus$ planet has a reduced torque due to gap formation.

In contrast, the simulations with VSI strongly disagree with the predictions. While it is not very surprising that the torques can be positive for a few orbits in context of turbulent discs, it is clearly visible that the average of torque is far from the predicted value. In case of the smallest planet with five earth masses the average of the torques is even five times larger than the torques in the alpha disc. This effect becomes smaller with increasing planet mass just as the VSI gets weaker due to the large planet disturbing the preferred VSI modes.

To shed light on this increase in torque we also show the torque distribution per unit disc mass as a function of radius in Fig. 7. Here we average again over the last 50 orbits and we compare to D'Angelo & Lubow (2008). In the lower panel of Fig. 7 we can again see a good agreement with their results, except for the heaviest planet. In the simulation with $M_p = 5\,M_\oplus$ the torque

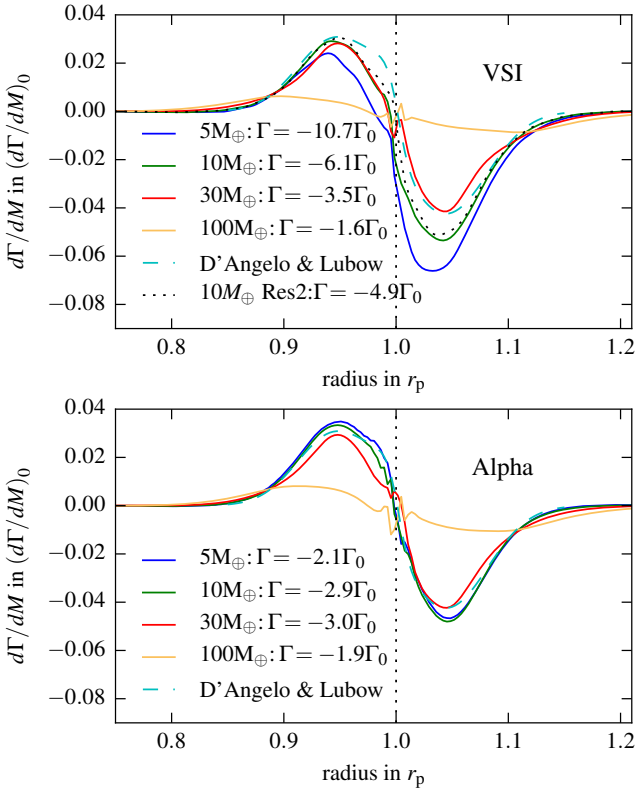

Fig. 7. Torques on the planets normalised by $(d\Gamma/dM)_0$, see eq. 10. **Upper Panel:** The planet is embedded into a disc with VSI. The inner torques are smaller then expected and the outer torques are stronger. **Lower Panel:** The planet is embedded into a disc with generic alpha viscosity. The torques are very similar to D'Angelo & Lubow (2010). In both simulations the torques for the heaviest planet are reduced due to the lower surface density in the gap.

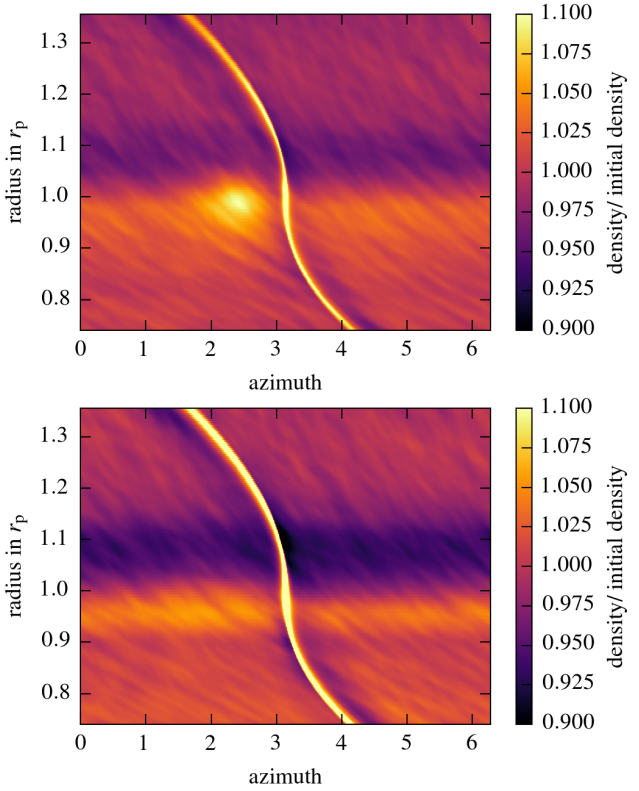

Fig. 8. Upper Panel: Density averaged over the last 100 orbits for the VSI simulation with $M_p = 5\,M_\oplus$ in units of initial density. **Lower Panel**: The density averaged over the last 100 orbits for the VSI simulation with $M_p = 10\,M_\oplus$ in units of initial density. In both cases an increase in density before the planet is visible, if only barely for the $10\,M_\oplus$ case. The bump in density does not move over time.

is five times stronger with active VSI compared to the simulation with alpha viscosity. This is due to a combination of reduced inner torque and stronger outer torque. This can not be explained with a variation in the radial surface density, because we could see in Fig. 5 that the density in the outer region is reduced and the density in the inner region is greater, leading to the opposite effect. Instead the surface density is dependent on the azimuthal direction. We see an increase in density at the inner side behind the planet and a decrease in density at the outer side in front of the planet. This can be seen in Fig. 8 where we average the density over 100 orbits. This is due to the increased vorticity behind the planet, from the interplay between the planet and the VSI as can be seen in the upper panels of Fig. 4.

3.5. A model with double resolution

To check the convergence with resolution, we repeat the simulation with $M_p = 10\,M_\oplus$ and VSI with doubled resolution in every direction. The resolution is then $1200 \times 256 \times 2048$ in (r, θ, φ) or (20,15,10) cells per r_H. The overall results show now no important difference to the results of the simulations with smaller resolution. A notable difference is in the alpha-profile, which we present in Fig. 1. We can see that in the inner region the alpha parameter is larger for the better resolved simulation. This indicates that the simulations are not properly resolved in the innermost region between 0.5-0.64 r_p. This also indicates that the rest of the domain is sufficiently resolved and not dependent on resolution, in contrast to the 2D simulations in Stoll & Kley (2014). This does not pose a problem for the calculations of the torques, which are only important close to the planet. This can be seen in Fig. 7, were the dotted black line represents the simulation with doubled resolution which can be compared to the green line. Both lines are as close together as one can expect from simulations with turbulence. No other notable differences have been observed.

4. Discussion and Conclusions

We performed a series of hydrodynamical simulations to study the interplay between a growing planet embedded in a protoplanetary disc and the VSI, which is a strong candidate for the main angular momentum transport mechanism in the region of active planet formation. The main results that can be drawn from our study are:

1. Vortices and VSI
   Larger planetary cores ($M_p > 10\,M_\oplus$) are able to open easily a gap in the disc, which lead to the generation of vortices at the gap edges. These vortices are observed both in VSI and α-disc models, however, due to the interaction between the vortices and the VSI, their lifetime is much longer in the VSI models. In our simulations we can see the presence of several weak spiral arms, for example in Fig. 3 (upper row), that can be associated with vortices generated by the Rossby-Wave Instability (RWI) near the edges of the gap created by

the planet. They are related to a maximum in the normalised vorticity profile, shown in Fig. 4. Furthermore the vorticity perturbations generated by the VSI, as suggested by Richard et al. (2016), are effectively increasing the lifetime of the RWI vortices, as one can see comparing the viscous and turbulent runs in the bottom panel of Fig. 4.

2. The VSI active region
The VSI active region is not affected sensibly by the embedded planets for planetary masses less than $30\,M_\oplus$. For higher masses the presence of vortices is able to suppress the VSI near their position. On the other hand the active region is extended inwards, at least for the most massive planet sudied (see Fig. 4). A possible explanation for this effect is the change in surface density profile due to the creation of a gap. This will in turn change the angular momentum profile and thus influence the VSI.

3. Planet migration
Concerning the migration of planets we find that the torques acting onto small planets for the α-disc models are in good agreement with the prediction of D'Angelo & Lubow (2010). This picture changes drastically for the inviscid models with the VSI operating. For small planets with masses smaller than about $10\,M_\oplus$ the time averaged torques are negative throughout. For the lowest planet mass we studied, $5\,M_\oplus$, the inward migration is about 5 times faster than for the α-disc model which is due to a density enhancement directly behind the planet. For increasing planet masses the migration rates approach those of the viscous disc. Due to this special disturbance in the density we do not see any prolonged phases of outward migration as seen for example for planets embedded in MHD-turbulent discs (Nelson 2005; Uribe et al. 2011). In general, because the density fluctuations in VSI turbulent discs are smaller than in MHD turbulence, the stochastic component in the migration process is lower in VSI discs. As three-dimensional inviscid simulations of disc will always generate turbulence through the VSI, embedded planets will experience substantial inward migration. This feature cannot be captured by modelling planet migration in two-dimensional inviscid discs that show typically a stalling of migration after a sufficiently wide gap has been formed (Li et al. 2009; Fung & Chiang 2017). In contrast, realistic three-dimensional discs will always show a finite turbulence level that will limit the gap depth. In fact, from our simulations we see that the width and depths of gaps opened by the planets are very similar in the VSI models and the corresponding α-disc models. In addition, small planets ($M_\mathrm{p} \leq 10\,M_\oplus$) that do not open significant gaps are able to modify the surface density profile close to their location which leads to the enhanced migration for the VSI turbulent discs.

4. Vortex migration and its implications
Vortex migration was first observed by Paardekooper et al. (2010) in isothermal discs, and then further studied by Faure et al. (2015) for radiative discs. Vortices are able to generate spiral arms by compressing the flow around them, and the migration occurs because of an asymmetry in the position of the sonic lines that generates the density waves. According to Richard et al. (2013) the migration speed is directly linked with the vortex aspect ratio (χ), it slows down upon increasing χ. In particular, Faure & Nelson (2016) studied the interaction of a planet with a vortex generated through RWI. Interestingly, they found that a massive vortex can drag with it the planet during the migration process, and it can also cross the planetary gap periodically crossing its location.
In our simulations for the $100\,M_\oplus$ planet, the inner vortex has a migration rate after an initial adjustment on the order of $0.001\,r_\mathrm{p}$/orbit, in accordance with (Richard et al. 2013), while the outer one is kept in its orbit by the steep surface density profile carved by the planet. The aspect ration of the inner vortex is around 3 which, according to Richard et al. (2013) should be destroyed after a few orbital periods due to elliptical instability (for $\chi < 4$). However, its lifetime is much more extended in our runs, meaning that the presence of the VSI is beneficial extending its life. On the other hand the outer vortex is much broader and with an higher aspect ratio. Both vortices have also a considerable vertical extent, and only in the outer corona they are effectively dissipated.

5. VSI as an angular momentum driving process
In agreement with previous simulations of VSI unstable discs Nelson et al. (2013), we find that an angular momentum transport driven by the VSI that corresponds to an $\alpha = 5{\cdot}10^{-4}$ which is not strongly affected by embedded planets. Hence, the VSI constitutes a viable candidate for the generation of turbulence in discs where the MRI may be inactive. Recently, we have shown (Stoll et al. 2017) that the turbulence generated by the VSI is anisotropic and can be described by a viscous ansatz for the stress tensor using two different coefficients for the radial and vertical angular momentum transport. It remains to be seen how an embedded planet behaves in such discs with anisotropic viscosities.

Thus, the VSI can on the one hand increase the strength of the vortices forming close to the gap edges for high planetary masses, and on the other hand boost the Type I migration for small planetary cores. This study can be further improved by relaxing the locally isothermal equation of state, and allowing the planet to accrete and migrate within the disc.

Acknowledgements. G. Picogna acknowledges the support through the German Research Foundation (DFG) grant KL 650/21 within the collaborative research program "The first 10 Million Years of the Solar System". M.H.R. Stoll acknowledges the support through the (DFG) grant KL 650/16. Some simulations were performed on the bwGRiD cluster in Tübingen, which is funded by the Ministry for Education and Research of Germany and the Ministry for Science, Research and Arts of the state Baden-Württemberg.

References

Andrews, S. M., Wilner, D. J., Hughes, A. M., Qi, C., & Dullemond, C. P. 2009, ApJ, 700, 1502
Arlt, R. & Urpin, V. 2004, A&A, 426, 755
Balbus, S. A. & Hawley, J. F. 1991, ApJ, 376, 214
Barge, P. & Sommeria, J. 1995, A&A, 295, L1
Baruteau, C. & Zhu, Z. 2016, MNRAS, 458, 3927
D'Angelo, G. & Lubow, S. H. 2008, ApJ, 685, 560
D'Angelo, G. & Lubow, S. H. 2010, ApJ, 724, 730
de Val-Borro, M., Artymowicz, P., D'Angelo, G., & Peplinski, A. 2007, A&A, 471, 1043
de Val-Borro, M., Edgar, R. G., Artymowicz, P., et al. 2006, MNRAS, 370, 529
Dullemond, C. P. & Dominik, C. 2005, A&A, 434, 971
Faure, J., Fromang, S., Latter, H., & Meheut, H. 2015, A&A, 573, A132
Faure, J. & Nelson, R. P. 2016, A&A, 586, A105
Fricke, K. 1968, ZAp, 68, 317
Fung, J. & Chiang, E. 2017, ArXiv e-prints [arXiv:1701.08161]
Gammie, C. F. 1996, ApJ, 457, 355
Goldreich, P. & Schubert, G. 1967, ApJ, 150, 571
Hawley, J. F. & Balbus, S. A. 1991, ApJ, 376, 223
Klahr, H. & Bodenheimer, P. 2006, ApJ, 639, 432
Klahr, H. & Kley, W. 2006, A&A, 445, 747
Kley, W. & Nelson, R. P. 2012, ARA&A, 50, 211
Koller, J., Li, H., & Lin, D. N. C. 2003, ApJ, 596, L91
Li, H., Lubow, S. H., Li, S., & Lin, D. N. C. 2009, ApJ, 690, L52
Lynden-Bell, D. & Pringle, J. E. 1974, MNRAS, 168, 603
Mignone, A., Bodo, G., Massaglia, S., et al. 2007, ApJS, 170, 228

Nelson, R. P. 2005, A&A, 443, 1067
Nelson, R. P., Gressel, O., & Umurhan, O. M. 2013, MNRAS, 435, 2610
Paardekooper, S.-J., Lesur, G., & Papaloizou, J. C. B. 2010, ApJ, 725, 146
Richard, S., Barge, P., & Le Dizès, S. 2013, A&A, 559, A30
Richard, S., Nelson, R. P., & Umurhan, O. M. 2016, MNRAS, 456, 3571
Shakura, N. I. & Sunyaev, R. A. 1973, A&A, 24, 337
Stoll, M. H. R. & Kley, W. 2014, A&A, 572, A77
Stoll, M. H. R. & Kley, W. 2016, A&A, 594, A57
Stoll, M. H. R., Picogna, G., & Kley, W. 2017, ArXiv e-prints [arXiv:1702.00334]
Uribe, A. L., Klahr, H., Flock, M., & Henning, T. 2011, ApJ, 736, 85
Urpin, V. & Brandenburg, A. 1998, MNRAS, 294, 399

4 Results

4.1 Summary

This dissertation studies the impact of the vertical shear instability (VSI) on the different phases of planet formation. In the first work "Vertical shear instability in accretion disk models with radiation transport", published in 2014, we focus on the VSI itself and applicability in the dead zone. We begin with analyzing the initial grow rates of the instability. The VSI quickly grows on the timescale of 30 local orbits from the initial small velocity perturbations to large modes threading through the whole vertical extend of the disk. The growth rates are in good agreement with earlier theoretical estimates (Urpin and Brandenburg, 1998, Urpin, 2003) and with similar simulations of Nelson et al. (2013).

We estimate the angular momentum transport, measured in α, to be on the level of a few times 10^{-4}. Since these simulations are only two dimensional axisymmetric simulations, which can me misleading, we also confirm this value in with a small 3D simulation of a quarter of the disk. We discover that the strength of the VSI seems to be dependent on the resolution, indicating missing numerical convergence. On the other hand we show that this issue can be resolved by adding a small kinematic viscosity, indicating that this is not a problem in physical disks. In fact, we could not see this problem in 3D simulations, indicating that this is a problem specific to inviscid 2D simulations.

Surprisingly, we find that the radial wavelength of the instability does locally not scale with the scale height of the disk, but instead with $\sim r^{2.5}$, a scaling that keeps the frequency of the vertical motion constant. Instead, we repeatedly see jumps in the wavelength, where it is halved, leading to expected scaling relative to the scale height on the global scale.

Based on these simulations we added radiative transport to the model, leading to self-consistent temperature profiles, since the heating and cooling of the disk is then correctly modeled, in contrast to the locally isothermal models before. This leads to an overall cooling of the disk, as the internal viscous heating due to the instability is too weak to match the radiative cooling of the disk surface and the instability dies out. Hence, we find that an external heat source in necessary to sustain the VSI. This is readily available through the central star. After we add the heating through the irradiation from star, we see again sustained VSI activity with an α-parameter of a few times 10^{-4}, similar to the locally isothermal models before.

In our next work "Particle dynamics in disks with turbulence generated by the vertical shear instability", published in 2016, we studied the impact of the VSI on dust particles embedded into the protoplanetary disk. We modeled the dust as particles with different sizes, from a radius of 0.1 mm up to km, that are influenced by the gas through the drag force in the Epstein regime. Since the dust fraction relative to the gas is small, we neglect the feedback of dust onto the gas. We also extended our simulations to three dimensions, allowing us to take into account perturbation in the azimuthal direction, which would for example allow the particles to be caught in vortices.

In order to reduce the computation time needed, we limited the azimuthal domain to an eighth of the full disk. We verified the validity of this approach by comparing a low resolution, locally isothermal model, with limited azimuthal extent, to a model with the full azimuthal extend. We did neither find a significant difference in the strength of the α-parameter nor in the azimuthal power spectrum.

We also improved our radiative model. In our earlier model in the first work we estimated the irradiation flux onto a flat disk model and irradiated this flux along the vertical direction. In this model we directly irradiate with the star along the radial direction. This ansatz allows for self-shadowing effects. With a density profile that is close to the Minimum Mass Solar Nebula (MMSN) but with a shallower decay, as determined from observations (Williams and Cieza, 2011), we obtain an VSI active region from 10 au to 60 au. Since this model is on the upper end in density, this results show again that it is very likely that parts of the dead zone are unstable to the VSI.

A very interesting result in this work is the formation of ringlike structures in the dust density due to the characteristic flow pattern of the VSI. This creates strong over-

densities in the dust density, where the dust density is increased by a factor of up to ten. This effect is strongest for particles with a stopping time on the timescale of one orbit and shorter, which translates to particles with a size between a few cm and several meters. This will most likely lead to enhanced rates of sticking collisions between these particles, especially since we observed relative velocities below the fragmentation limit of 50 m/s. It is also important for the onset of the streaming instability (see Sect. 1.2), which requires a dust to gas ratio of around one to ten. If this ratio is reached the streaming instability can increase the overdensities to even greater values, leading to the formation of planetesimals. This makes the VSI active region a suitable birthplace for planets.

The results for the dust distribution and migration are also interesting. A disk with active VSI has an unusual radial flow pattern, where the gas flows inwards at the midplane and outwards in the corona. This is opposite to the meridional flow observed in α-disk models (Kley and Lin, 1992). Hence, particles that are kicked towards the corona are no longer tightly coupled to the gas and can quickly migrate outwards. While this process is very rare, these particles will migrate outwards faster as expected from the turbulent diffusion alone. We could also see that the VSI is effective in preventing dust settling, far more than the α-parameter would imply.

We further analyze this radial flow pattern in our letter "Anisotropic hydrodynamic turbulence in accretion disks", published in 2017. We show that the inverted radial flow is a result of the anisotropic turbulence. This anisotropy is caused by the much larger vertical wavenumber compared to the radial wavenumber, that is necessary for VSI activity. The α-model can be savaged by splitting the isotropic α-parameter into two parameter thus allowing for different radial and vertical stresses. This ansatz then recovers the inverse radial flow pattern.

Finally, in our last publication for this dissertation, we studied the interaction between the VSI and planets of different masses by embedding the planets in VSI active disks. We compared these simulations to disks with the traditional viscous α-model. This allowed us to compare disks with turbulent viscosity, due to the VSI, to disks with kinematic viscosity, enabling us the check the validity of the α-model for the case of planet-disk interaction.

Since the impact of the planet's potential on the disk changes the angular momen-

tum structure, there is reason to suspect that the presence of a planet can impede the VSI activity and thus the level of turbulence generated by it. We could not detect this, even the most massive planet we included, with a mass of $100\,M_\oplus$, did not change the gap profile, compared to a viscous α-disk, in a significant way. The gap size is a good indicator for the α-parameter, since the gap size depends on how fast the angular momentum the gas gained or lost through the interaction with the planet can be transported away. Also the direct calculation of α did not show weakening close to the planet. In fact the presence of the $100\,M_\oplus$ planet seems to strengthen the VSI activity in the inner region, while the smaller planets do not impact the VSI at all.

Nevertheless the VSI has a large impact on the disk, by favoring the creation of vortices. This was already seen be Richard et al. (2016) in disks without planets. These vortices are what sets the VSI disks apart from their viscous counterparts. Most notably are the vortices in the $100\,M_\oplus$ model. There the gap edge creates the necessary condition for the Rossby wave instability in both models. While the condition is met in both models, the turbulent and the viscous disk, in case of the turbulent disk the vortices at the inner and outer edge are stronger and show no sign of decay during the runtime of the simulation over the 200 orbits. The vortex at the inner edge even starts to migrate inwards, away from the edge, without decaying.

But the models with smaller planets are also impacted by this tendency to sustain vortices. In these models very small vortices are created at the edge of the spiral arm, close to planet. These vortices then travel along the inner horse shoe orbit, until they are behind the planet, where they collect to form a larger vortex. Because these vortices also collect gas, they also impact the torque of the disk onto the planet and lead to a faster inward migration of the planet. In case of the $5\,M_\oplus$ model, the torque was five times stronger than in the viscous α-model. This clearly indicates that it is impossible to model type I migration with the viscous α-model in VSI active regions and poses a new problem for planet formation.

4.2 Outlook

We could show that the VSI can play a major role in the different stages of planet formation. Nevertheless there are several questions that need to be answered before the role of the VSI is clear. Further investigation is needed to discern the region where the VSI can be active. While we could show that it is in principle possible for the VSI to be present in some part of the dead zone, the level of turbulence and extend of this region have not been thoroughly explored. They depend for example on the initial density in the disk, which can only be constrained by better observations, and on the opacity of the gas. The opacity will not only depend on density and temperature but also on the dust fraction in the outer layers of the protoplanetary disk, which is influenced by the turbulence, in this case the VSI and possibly also the MRI, making a self-consistent solution difficult.

The temperature gradient in the disk will also depend on the MRI in the inner region of the disk. The MRI can not only provide additional heating of the disk, but also locally increase the disk scale height, due to heating the disk more, and thus create a self-shadowed region behind the MRI active region, with a steeper temperature gradient.

As already mentioned the dust clustering is an important effect. But in our current implementation only the gas has an impact on the dust and the backreaction of the dust on the gas is missing. While this is a good approximation for the initial dust to gas fraction found in accretion disks, the dust fraction can reach a critical level where the approximation is no longer valid, due to the dust clumping introduced by the VSI, and the streaming instability could become important. Hence, future simulations should include the backreaction, allowing to check if even greater clustering can be reached after the onset of the streaming instability.

The fast migration rate in the VSI model aggravates the problem of planets falling into the star, before the accretion disk disappears. But this can also be turned around as further indication that there is a region that can halt planet migration, for example the inner edge of the dead zone. Then the fast migration rate can even be seen as an advantage, as it forces the planet out of the region that enables planet formation and makes room for more planets, explaining the large number of crowded planetary systems discovered.

We can also look forward to more observations from the Atacama Large Millime-

ter/submillimeter Array (ALMA). ALMA observes in the millimeter and submillimeter wavelengths, thus allowing us to resolve the structure of the dust in protoplanetary disks. This already produced the beautiful image of HL Tau, where several rings are visible (shown in Fig. 1.2). To date it is unclear how these rings can be explained. While the VSI produces ringlike structures, they can not easily connect to rings of HL Tau, as they are most visible for larger dust grains than observed and also have different spacing between the rings. This could possibly be explained with fragmentation of the clustered particles. Only simulations including the dust collision and fragmentation will be able to tell us if the VSI is connected with these observations. This is an important next step, as only observations can be the final arbiter of any theory.

5 Acknowledgments

First I want to thank Willy Kley, who was an excellent supervisor. He was always available for questions and helpful discussions and could point me to interesting papers.

I also want to thank the Land Baden-Württemberg. They helped me directly, by funding part of my PhD via a stipendium from the Landesgraduiertenförderung, but also indirectly by funding the high performance cluster BWgrid, without which the largest of my simulations for this thesis would have been impossible.

Special thanks to my family, for the support and encouragement during my graduation. I also thank my friends for keeping me motivated.

Bibliography

ALMA Partnership, Brogan, C. L., Pérez, L. M., Hunter, T. R., Dent, W. R. F., et al. (2015). The 2014 ALMA Long Baseline Campaign: First Results from High Angular Resolution Observations toward the HL Tau Region. ApJ, 808:L3.

Arlt, R. and Urpin, V. (2004). Simulations of vertical shear instability in accretion discs. A&A, 426:755–765.

Armitage, P. J. (2011). Dynamics of Protoplanetary Disks. ARA&A, 49:195–236.

Balbus, S. A. and Hawley, J. F. (1991). A powerful local shear instability in weakly magnetized disks. I - Linear analysis. II - Nonlinear evolution. ApJ, 376:214–233.

Barker, A. J. and Latter, H. N. (2015). On the vertical-shear instability in astrophysical discs. MNRAS, 450:21–37.

Blum, J. (2010). Dust growth in protoplanetary disks — a comprehensive experimental/theoretical approach. *Research in Astronomy and Astrophysics*, 10(12):1199.

D'Angelo, G. and Lubow, S. H. (2010). Three-dimensional Disk-Planet Torques in a Locally Isothermal Disk. ApJ, 724:730–747.

de Val-Borro, M., Artymowicz, P., D'Angelo, G., and Peplinski, A. (2007). Vortex generation in protoplanetary disks with an embedded giant planet. A&A, 471:1043–1055.

Fricke, K. (1968). Instabilität stationärer Rotation in Sternen. ZAp, 68:317.

Gammie, C. F. (1996). Layered Accretion in T Tauri Disks. ApJ, 457:355.

Gammie, C. F. (2001). Nonlinear outcome of gravitational instability in cooling, gaseous disks. *The Astrophysical Journal*, 553(1):174.

Goldreich, P. and Schubert, G. (1967). Differential Rotation in Stars. ApJ, 150:571.

Han, E., Wang, S. X., Wright, J. T., Feng, Y. K., Zhao, M., Fakhouri, O., Brown, J. I., and Hancock, C. (2014). Exoplanet Orbit Database. II. Updates to Exoplanets.org. PASP, 126:827.

Kley, W. and Lin, D. N. C. (1992). Two-dimensional viscous accretion disk models. I - On meridional circulations in radiative regions. ApJ, 397:600–612.

Kokubo, E. and Ida, S. (1998). Oligarchic growth of protoplanets. *Icarus*, 131(1):171 – 178.

Kolb, S. M., Stute, M., Kley, W., and Mignone, A. (2013). Radiation hydrodynamics integrated in the PLUTO code. A&A, 559:A80.

Krot, A., Amelin, Y., Bland, P., Ciesla, F., Connelly, J., Davis, A., Huss, G., Hutcheon, I., Makide, K., Nagashima, K., Nyquist, L., Russell, S., Scott, E., Thrane, K., Yurimoto, H., and Yin, Q.-Z. (2009). Origin and chronology of chondritic components: A review. *Geochimica et Cosmochimica Acta*, 73(17):4963 – 4997. The Chronology of Meteorites and the Early Solar System.

Lesur, G. and Papaloizou, J. C. B. (2010). The subcritical baroclinic instability in local accretion disc models. A&A, 513:A60.

Li, H., Colgate, S. A., Wendroff, B., and Liska, R. (2001). Rossby Wave Instability of Thin Accretion Disks. III. Nonlinear Simulations. ApJ, 551:874–896.

Li, H., Finn, J. M., Lovelace, R. V. E., and Colgate, S. A. (2000). Rossby Wave Instability of Thin Accretion Disks. II. Detailed Linear Theory. ApJ, 533:1023–1034.

Lin, M.-K. and Youdin, A. N. (2015). Cooling Requirements for the Vertical Shear Instability in Protoplanetary Disks. ApJ, 811:17.

Lovelace, R. V. E., Li, H., Colgate, S. A., and Nelson, A. F. (1999). Rossby Wave Instability of Keplerian Accretion Disks. ApJ, 513:805–810.

Lyra, W. (2014). Convective Overstability in Accretion Disks: Three-dimensional Linear Analysis and Nonlinear Saturation. ApJ, 789:77.

Lyra, W. and Mac Low, M.-M. (2012). Rossby Wave Instability at Dead Zone Boundaries in Three-dimensional Resistive Magnetohydrodynamical Global Models of Protoplanetary Disks. ApJ, 756:62.

Masset, F. S. and Papaloizou, J. C. B. (2003). Runaway Migration and the Formation of Hot Jupiters. ApJ, 588:494–508.

Mignone, A., Bodo, G., Massaglia, S., Matsakos, T., Tesileanu, O., Zanni, C., and Ferrari, A. (2007). PLUTO: a Numerical Code for Computational Astrophysics. In *JENAM-2007, "Our Non-Stable Universe"*, pages 96–96.

Nelson, R. P., Gressel, O., and Umurhan, O. M. (2013). Linear and non-linear evolution of the vertical shear instability in accretion discs. MNRAS, 435:2610–2632.

Richard, S., Nelson, R. P., and Umurhan, O. M. (2016). Vortex formation in protoplanetary discs induced by the vertical shear instability. MNRAS, 456:3571–3584.

Shakura, N. I. and Sunyaev, R. A. (1973). Black holes in binary systems. Observational appearance. A&A, 24:337–355.

Stoll, M. H. R. and Kley, W. (2014). Vertical shear instability in accretion disc models with radiation transport. A&A, 572:A77.

Stoll, M. H. R. and Kley, W. (2016). Particle dynamics in discs with turbulence generated by the vertical shear instability. A&A, 594:A57.

Stoll, M. H. R., Kley, W., and Picogna, G. (2017). Anisotropic hydrodynamic turbulence in accretion disks. A&A, 599:L6.

Toomre, A. (1964). On the gravitational stability of a disk of stars. ApJ, 139:1217–1238.

Urpin, V. (2003). A comparison study of the vertical and magnetic shear instabilities in accretion discs. A&A, 404:397–403.

Urpin, V. and Brandenburg, A. (1998). Magnetic and vertical shear instabilities in accretion discs. MNRAS, 294:399.

Weidenschilling, S. J. and Cuzzi, J. N. (2006). *Accretion Dynamics and Timescales: Relation to Chondrites*, pages 473–485.

Williams, J. P. and Cieza, L. A. (2011). Protoplanetary Disks and Their Evolution. ARA&A, 49:67–117.

Windmark, F., Birnstiel, T., Güttler, C., Blum, J., Dullemond, C. P., and Henning, Th. (2012). Planetesimal formation by sweep-up: how the bouncing barrier can be beneficial to growth. A&A, 540:A73.

Youdin, A. and Johansen, A. (2007). Protoplanetary Disk Turbulence Driven by the Streaming Instability: Linear Evolution and Numerical Methods. ApJ, 662:613–626.